Summer 2024

Exploring Seismic Anisotropy in the Crust and Mantle of the Tibetan Plateau and Analyzing Seismic Velocity Variations in Yellowstone

Cong Shen
Missouri University of Science and Technology

EXPLORING SEISMIC ANISOTROPY IN THE CRUST AND MANTLE OF THE TIBETAN PLATEAU AND ANALYZING SEISMIC VELOCITY VARIATIONS IN YELLOWSTONE

by

CONG SHEN

A DISSERTATION

Presented to the Graduate Faculty of the

MISSOURI UNIVERSITY OF SCIENCE AND TECHNOLOGY

In Partial Fulfillment of the Requirements for the Degree

DOCTOR OF PHILOSOPHY

in

GEOLOGY AND GEOPHYSICS

2024

Approved by:

Kelly H. Liu, Advisor
Stephen S. Gao, Co-advisor
Taghi Sherizadeh
Marek Locmelis
Xingyao Yin

PUBLICATION DISSERTATION OPTION

This dissertation consists of the following two articles, formatted in the style used by the Missouri University of Science and Technology:

Paper I, found on pages 3-84, has been submitted to *Journal of Geophysical Research: Solid Earth*.

Paper II, found on pages 85-125, is intended for submission to *Journal of Geophysical Research: Solid Earth*.

ABSTRACT

Seismology is a scientific discipline that utilizes seismic waves to investigate the deep structures within the Earth's interior, which are otherwise inaccessible to direct observation by humans. These seismic waves can be categorized into two types: body waves and surface waves, each with distinct propagation modes and behaviors, carrying valuable information about their travel paths. The first paper concentrates on the analysis and inversion of body waves produced by large seismic events. It employs shear wave splitting and receiver function methods to explore the geodynamic structure of the south-central Tibetan Plateau, near the plate boundary. The investigation covers the depth range from the crust to the upper mantle, yielding a three-dimensional plate tearing model to elucidate the observed weak anisotropy in the southern region and the variable anisotropy in the northern region. The second paper utilizes surface waves, which include ambient noise from anthropogenic sources or micro-natural events, to study the crustal velocity structure below the Yellowstone caldera, which formed approximately 0.53 million years ago. Tomography results reveal the presence of low-velocity anomaly zones within and surrounding the caldera. Through a comparative analysis of Green's functions spanning 40 days and 13 years, we constructed seismic velocity perturbation diagrams over time. Notably, we observed pronounced annual periodicity in the velocity profiles of Norris Geyser Basin, Hot Spring Basin, and Jackson Lake in the vicinity of the caldera. These cyclic variations were found to be primarily driven by meteorological factors, as elucidated by corresponding meteorological data.

ACKNOWLEDGMENTS

I extend my heartfelt gratitude to my family for their unwavering support throughout my academic journey. Their unconditional financial and emotional assistance has been invaluable since my undergraduate days. I recognize that without their constant encouragement and aid, I would not have been able to successfully complete my studies. Their support has been the cornerstone of my academic success, and I am deeply grateful for their love and care.

I would like to extend my sincere appreciation to my advisor, Dr. Kelly Liu, and my co-advisor, Dr. Stephen Gao, for their unwavering support and meticulous guidance in both my academic and personal life. Their mentorship has been instrumental in shaping my research and academic pursuits.

I am also grateful to my committee members, Dr. Taghi Sherizadeh, Dr. Marek Locmelis, and Dr. Xinyao Yin, for their valuable input and advice throughout my research journey, especially during the three crucial exams. Their expertise and feedback have been instrumental in improving the quality of my work.

I am fortunate to have my colleagues and seniors, who enrich my extracurricular life and provide great assistance in my research endeavors. Their contributions have been instrumental in making my academic journey a memorable and fulfilling experience, and I am sincerely thankful for their presence in my life.

TABLE OF CONTENTS

Page

LIST OF ILLUSTRATIONS

PAPER I Page

PAPER II

NOMENCLATURE

Symbol	Description
H	Moho depth
κ	V_p/V_s ratio
V_p	P wave velocity
V_s	S wave velocity
δt	Splitting time
$\emptyset$	Fast polarization orientation
P_ms	P to S converted phase at Moho
t_0	Theoretical arrival time of P_ms phase
Δt	Moveout of the arrivals
A	High-quality shear wave splitting measurements
B	Moderate-quality shear wave splitting measurements
C	Poor-quality shear wave splitting measurements
N	Null shear wave splitting measurements
M_s	Surface wave magnitude
F_v	Variation factor
w	Weighting factor
SD	Standard Deviation
S_{Hmax}	Maximum horizontal compressive stress
C	Cross coherence
F	Fast Fourier transformation

X	Amplitude
φ	Phase
Δt	Delay time
A	Amplitude in frequency domain
D	Distance in meter

1. INTRODUCTION

In the multidisciplinary field of geophysics, the investigation of seismic anisotropy and ambient noise play a vital role in the Earth's lithospheric and asthenospheric dynamics. Seismic anisotropy, a phenomenon attributed to the preferential alignment of minerals within the Earth's crust and mantle, serves as a diagnostic tool in deciphering the mechanical behavior of tectonic plates and the underlying mantle flow patterns. This research particularly emphasized by observational studies in regions characterized by tectonic complexity such as the Tibetan Plateau, delineates the critical role of lower crust and asthenosphere as mechanically weak zones. These zones, as opposed to the more rigid upper crust and lithospheric mantle, are instrumental in accommodating strain and facilitating the dynamical processes that drive plate movements (Jolivet et al., 2018; McKenzie, 1978; Molnar et al., 1993; Silver, 1996).

Parallel to the study of deep Earth processes, research into shallow seismic velocity variations offers critical perspectives on the Earth's near-surface layers. Variations in seismic velocity at shallow depths, influenced by factors such as lithological composition, porosity, moisture content, and environmental conditions, are crucial for interpreting geophysical data and assessing seismic hazards (De Fazio et al., 1973; Roumelioti et al., 2020). Recent investigations highlight the significance of these variations in understanding subsurface geological structures and dynamics, notably within volcanic and hydrothermal regions like Yellowstone Park (Miller & Smith, 1999; Husen et al., 2004). Numerous methodologies, including resistivity tomography, seismic refraction, and surface wave analysis, have advanced the resolution and accuracy of

subsurface imaging, revealing complex velocity structures associated with geothermal processes and magmatic activities (Pasquet et al., 2016; Waite et al., 2006) in the Yellostone region.

Seismic anisotropy analysis, through techniques such as shear wave splitting and receiver function analysis, has elucidated the deformation patterns and flow dynamics within the lithosphere and asthenosphere, contributing to our understanding of tectonic processes and plate dynamics (Gao & Liu, 2009; Wu et al., 2015). Similarliy, investigations into shallow seismic velocity variations have enhanced our grasp on the lithological and environmental determinants of seismic wave propagation, which are essential for seismic hazard assessment and environmental geophysics.

Our two seismic research reveals the intricate interplay between deep mantle dynamics and surface geological phenomena, providing a nuanced understanding of the Earth's geodynamic processes. Future studies, leveraging advanced seismic imaging techniques and interdisciplinary methodologies, are poised to further unravel the complexities of Earth's internal and surface processes, offering new perspectives on the mechanisms driving tectonic movements, volcanic activities, and seismic hazards.

PAPER

I. TECTONIC IMPLICATIONS OF SEISMIC ANISOTROPY LAYERING BENEATH THE SOUTHERN TIBETAN PLATEAU REVEALED BY INTEGRATED SHEAR WAVE SPLITTING AND RECEIVER FUNCTION ANALYSES

ABSTRACT

To investigate continental dynamics underneath the south-central Tibetan Plateau, which composes the Himalayan, Lhasa, and Qiangtang blocks, we have conducted comprehensive examinations of seismic azimuthal anisotropy in the crust using receiver functions (RFs) and crustal and mantle anisotropy using teleseismic shear wave splitting (SWS) analysis. In the Qiangtang block, the observed predominantly E-W fast orientations from RF and SWS analyses with similar magnitude are interpreted as resulting from eastward crustal flow with minor contributions from the mantle. In the Lhasa block, the crustal anisotropy is approximately N-S oriented, which is parallel to the strike of rift basins and southward crustal flow. Anisotropy revealed by SWS demonstrates a rotation from E-W in the north to NE-SW in the south, which can be interpreted as reflecting mantle flow field induced by the northward movement of the subducting Indian plate. The addition of PKS and SKKS measurements and extension of epicentral distance range to 171.8 degrees for SWS analysis revealed dominantly strong E-W oriented anisotropy in most parts of the Himalayan block, where most previous studies reported pervasively null measurements. The absence of azimuthal anisotropy is observed in two regions in the Himalayan block which is attributable to mantle upwelling

through a previously identified slab window. A two-layered anisotropy structure with different fast orientations for the upper and lower layers can be constrained in the southern Qiangtang and the vicinity of the Main Boundary Thrust.

Keywords: Tibetan Plateau, seismic anisotropy, shear wave splitting, receiver functions

PLAIN LANGUAGE SUMMARY

In our study exploring the underground dynamics beneath the south-central Tibetan Plateau, an area encompassing the Himalayan, Lhasa, and Qiangtang blocks, we utilized advanced seismic techniques to uncover the structure and dynamics of the earth's crust and mantle. In the Qiangtang region, our findings suggest an eastward crustal movement with minimal mantle influence. In the Lhasa block, the observed crustal anisotropy aligns with rift basins, indicating a southward flow. In the same area, we also observed a transition in flow patterns from east-west in the north to northeast-southwest in the south, attributed to the northward movement of the Indian plate. Contrary to previous studies that often found no anisotropy in the Himalayan block, our research detected strong anisotropy with east-west orientations. In two areas of the Himalayan block, the absence of anisotropy likely results from molten rock rising through a gap in the Indian plate. Moreover, we discovered a two-layered structure of rock alignment near the Main Boundary Thrust and the Qiangtang block.

1. INTRODUCTION

Numerous observational and laboratory studies have demonstrated that the lower crust and asthenosphere, representing mechanically weak zones relative to the more rigid overlying upper crust and lithospheric mantle, respectively, play a critical role in accommodating strain and the dynamical processes of driving plate movements (Jolivet et al., 2018; McKenzie, 1978; Molnar et al., 1993; Silver, 1996). These weak zones allow for the horizontal movement of tectonic plates and isostatic adjustments leading to vertical movements of lithospheric blocks (Hollister & Crawford, 1986). Such movements are mostly responsible for generating structural or lithological fabrics in the crust and upper mantle, which can in turn be used to reveal the existence and characteristics of past and ongoing tectonic events such as the continental convergence occurring along the Himalayas over the past 55 million years (Agius & Lebedev, 2017; Conrad & Behn, 2010; Jin et al., 1996; McKenzie, 1978).

The Tibetan plateau, generally regarded as the consequence of a series of subductions and subsequent collisions of continental blocks, has been the focus of numerous studies aiming at understanding the complex tectonic processes involved in continental collision during the last several decades (e.g., Zhao et al., 1993). The relative plate motion between the northward-moving Indian plate and the westward-moving Eurasian plate in the hotspot reference frame (Gripp & Gordon, 2002) is fundamentally responsible for the extensive changes in the topography, structure, and sedimentary facies of the plateau since the Late Cretaceous (Yin & Harrison, 2000). Before the collision, the pre-existing Tethys was extruded under the action of the northward thrust of the Indian

plate, and its oceanic lithosphere descended underneath the Eurasian plate (Hsü et al., 1995). This and previous continental convergence have led to the amalgamation of the Himalayan, Lhasa, and Qiangtang blocks from south to north, bordered by the Indus-Yarlung, Bangong-Nujiang, and Jinshajiang sutures, respectively (Figure 1). In addition, the collision triggered numerous secondary structures (Molnar et al., 1973), including the N-S trending rifts (Nie et al., 2020), orogeny-parallel thrusts (Langille et al., 2010), and active detachments (Kapp et al., 2008). Exploring subsurface structure and dynamics in the crust and upper mantle is essential for understanding the formation mechanisms of the tectonic features observed on the plateau.

Seismic azimuthal anisotropy is widely utilized for probing crustal and upper mantle deformation in subduction and collision zones (e.g., Boness & Zoback, 2006; Gao & Liu, 2009; Wu et al., 2015). In the upper mantle, the lattice-preferred orientation of anisotropic minerals, predominantly olivine, formed in response to simple shear associated with mantle flow, generates flow-parallel seismic anisotropy under normal mantle conditions (Ismaïl & Mainprice, 1998). Anisotropy could also be induced by past tectonic processes, which were then frozen into the rigid lithosphere (Silver, 1996). In the lower crust, amphibole and mica are highly anisotropic minerals that can lead to non-negligible anisotropy compared to the upper mantle, with a resulting orientation consistent with the simple shear direction (Christensen, 1984; Ko & Jung, 2015). In contrast, anisotropy in the upper crust is mainly associated with the alignment of fluid-filled cracks (Crampin, 1981), with a resulting orientation parallel to the maximum compression direction.

Numerous studies on seismic anisotropy have been conducted in the south-central Tibetan plateau to investigate geodynamic processes associated with continental collision (e.g., Chen et al., 2010; Fu et al., 2008; Gilligan & Priestley, 2018; Hirn et al., 1995). Chen et al. (2010) analyzed 51 SKS and SKKS events recorded by 86 stations in the Hi-CLIMB array. They observed a strong E-W-oriented anisotropy in the southern Qiangtang block and the northern Lhasa block, and NE-SW oriented anisotropy in the southern Lhasa block (Figure 1). An abrupt northward increase in seismic anisotropy at ~33°N in the Qiangtang block was inferred to mark the subducted Indian slab front (Chen et al., 2010; Chen et al., 2015; Sandvol et al., 1997; Singh et al., 2006). The pattern of anisotropy exhibits a clockwise rotation from E-W in the north near the Bangong-Nujiang suture to N-S in the south near the Indus-Yarlung suture (Chen et al., 2010), challenging earlier interpretations of isotropic Indian lithosphere front (e.g., Sandvol et al., 1997; Singh et al., 2006). Such a rotational pattern is attributed to the presence of crustal channel flow (Basuyau et al., 2013; Gilligan & Priestley, 2018; Lease et al., 2012). In the Himalayan block, pervasive weak anisotropy measurements were observed by over 90% of the Hi-CLIMB and portable stations (e.g., Chen & Ozalaybey, 1998; Chen et al., 2010; Fu et al., 2008), with the formation mechanism still under debate. Distinct geodynamic models propose either a localized mantle upwelling (Fu et al., 2008) or an isotropic Indian lithosphere (e.g., Chen & Ozalaybey, 1998) as explanations.

Investigations of seismic velocity heterogeneity beneath the southern and central Tibetan plateau suggest that the Indian slab is torn into several segments, each characterized by different dipping angles and sizes (Chen et al., 2015; Duan et al., 2017), with three lithosphere breakage bands distinguished by low Pn and S-velocity zones

(Jiang et al., 2014; Li & Song, 2018). Increasing evidence suggests that crustal anisotropy on the Tibetan plateau could contribute significantly (up to 50%) to the observed anisotropy measurements using splitting of the PKS, SKKS, and SKS phases (Agius & Lebedev, 2017; Wu et al., 2015). While the structural frameworks within the crust and upper mantle of the central Tibetan plateau are well established, the deformation fields in the crust and upper mantle and their formation mechanisms remain poorly understood and controversial (e.g., Chen et al., 2010; Fu et al., 2008). These controversies are likely related to the inherent limitations of the approaches used, notably shear wave splitting (SWS) analyses, which provide high horizontal but lack vertical resolution (e.g., Long & Silver, 2009; Savage, 1999). This limitation impedes our understanding of deformation fields. Thus, additional investigations on anisotropy depth and layered structures are necessary to isolate crustal contribution and better constrain upper mantle anisotropy. In particular, confirming or rejecting the previously observed dominantly null measurements in the Himalayan block and proposing a viable mechanism for the observed anisotropy are essential for understanding mantle dynamics in the archetypical continental collision zone.

In this study, we have incorporated additional constraints on the deformation models by conducting a joint analysis of individual shear wave splitting parameters and receiver function-based crustal anisotropy measurements. Our goal is to explore the anisotropic structure present within the crust, lithospheric mantle, and asthenosphere, respectively. By increasing the coverage of back azimuth (BAZ) relative to previous

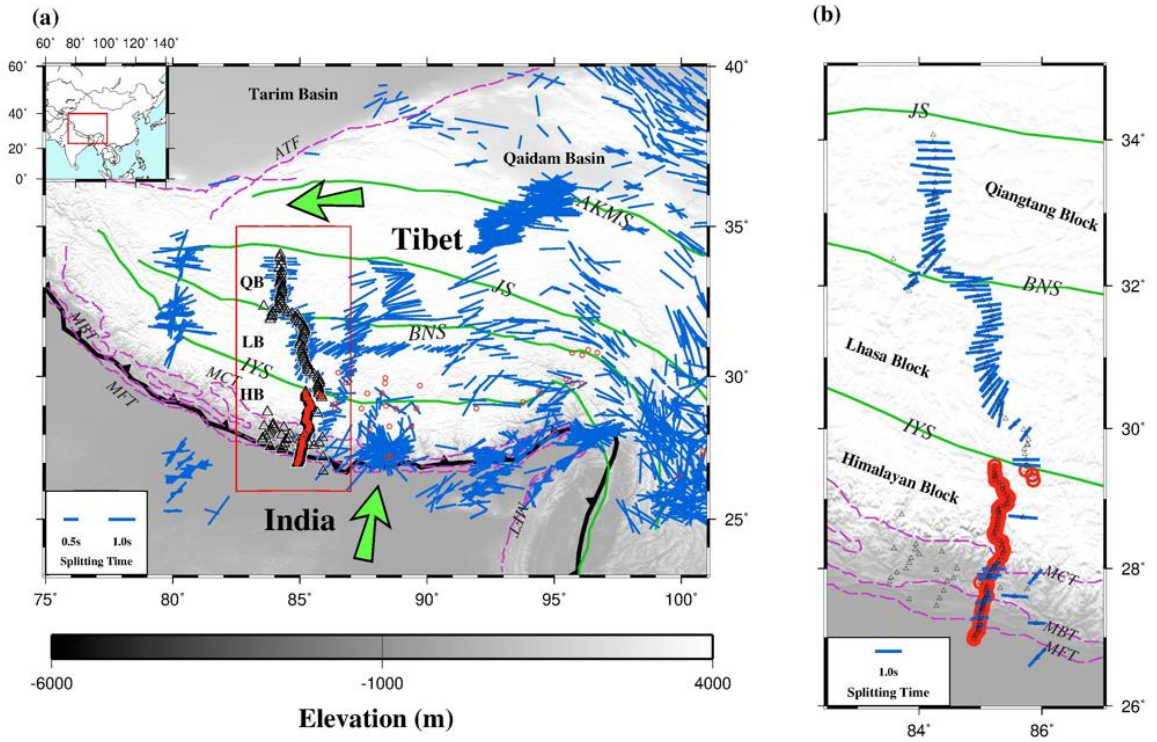

Figure 1. Tibetan topography map with previous SWS results. (a) A topography map showing the major geophysical and geological features in the studying area (red rectangle) and adjacent regions. The blue bars indicate the non-null SWS results while the red circles are where the null measurements are located from previous studies (Chen et al., 2010; Chen et al., 2015; Sandvol et al., 1997; Singh et al., 2006). The black triangles are the stations used in this study. The green arrows denote the absolute plate motion direction of the Eurasian plate and Indian plate calculated by the HS3-NUVEL-1A plate model (Gripp & Gordon, 2002). MFT: Main Frontal Thrust; MBT: Main Boundary Thrust; MCT: Main Central Thrust; IYS: Indu-Yarlung Suture; BNS: Bangong-Nujiang suture; JS: Jinshajiang Suture; ATF: Altyn Tagh Fault; HB: Himalaya Block; LB: Lhasa Block; QB: Qiangtang Block. (b) Enlargement of the study area outlined by the red rectangle. Note that only the shear wave splitting measurements recorded by the stations used in this study are shown.

SWS studies, through an expanded epicentral distance range and the inclusion of the PKS phase, the resulting anisotropy measurements demonstrate significant spatially varying anisotropy within both the crust and upper mantle, with deformations concentrated in the two mechanically weak layers, i.e., the middle/lower crust and asthenosphere. In the

Himalayan block, strong E-W oriented anisotropy is observed and is attributed mainly to sub-slab collision-zone parallel flow.

2. DATA AND METHOD

Data used to obtain the SWS measurements were recorded by 141 broadband seismic stations, among which 120 were part of the 2002-2005 Hi-CLIMB array and 21 were from other portable experiments. All the data were obtained from the Seismological Facility for the Advancement of Geoscience Data Management Center. When a seismic shear wave goes through an anisotropic media, it tends to split into two waves, leading to an arrival time difference between the fast and slow wave components. In this study, we utilize source-normalized P-to-s conversions from the Moho (receiver functions or RFs) and teleseismic SWS analyses to compute the optimal splitting parameters (fast polarization orientation ∅ and delay time δt).

2.1. MEASUREMENTS OF CRUSTAL ANISOTROPY USING RECEIVER FUNCTION ANALYSIS

The seismograms used for receiver function analysis were recorded by events with epicentral distances between 30.0° and 180° (Figure 2) and are band-pass filtered within the frequency range of 0.08 to 0.8 Hz. The RFs are then computed using a time-domain iterative deconvolution method (Ligorria & Ammon, 1999). Low quality RFs are rejected following the signal-to-noise ratio selection criteria (Liu & Gao, 2013) to ensure

data quality. A total of 21,901 radial RFs are selected from 1695 events (Figure 2) to investigate the crustal anisotropy.

We use the same procedure utilized in Kong et al. (2016) and Zheng et al. (2024) to quantify the bulk crustal anisotropy. After correcting the P-to-s conversion time ($P_m s$) differences due to epicentral and focal depth differences (Zheng et al., 2018), the receive functions are stacked using a grid search method (Nair et al., 2006; Zhu & Kanamori, 2000) to estimate the crustal thickness (H) and Vp/Vs (κ), which are subsequently used as a constraint for picking the $P_m s$ phase. Examples of crustal anisotropy measurements for stations H1020 and H1540 can be found in Figures S1 and S2.

Under the assumption of a single layer of anisotropy with a horizontal axis of symmetry, the moveout of the converted phases from the Moho ($P_m s$) satisfies the sinusoidal function in terms of the BAZ (Kong et al., 2016; Rumpker et al., 2014). Since the $P_m s$ phase arrival time repeats every 180°, we adjust stations with BAZs over 180° by subtracting 180°, grouping them into the 0-180° range to determine the anisotropy parameters for these stations. All the RFs are grouped into consecutive 10° azimuthal bins based on their BAZ. Anisotropy parameters are derived from the grouped RFs through curve fitting of the $P_m s$ arrival times corresponding to the maximum amplitudes using a nonlinear least-squares algorithm as well as through grid search to identify optimal parameters for maximum stacking amplitude (Wu et al., 2015).

Considering the wide range of Moho depths in the study area (Nábelek et al., 2009), we employ a search range of 0.0-2.0 s for δt with an increment of 0.1 s, and a ∅ range of -90° to 90° with a 1° increment. The arithmetic means of δt and the angular mean of ∅ are selected if the delay time difference from the two methods (i.e., curve-

fitting and grid-searching) is less than 0.15 s, and the difference between two fast polarization orientations is less than 20°. For larger discrepancies in delay times and fast orientations between results from the two methods, the curve-fitting results are preferred for their stability compared to the grid-searching results. To ensure the robustness of the results, we manually verified the results to reject those with poor BAZ coverage and ambiguous $P_m s$ arrival times. This step also involved adjusting the time window to exclude arrivals that are inconsistent with the calculated arrival time based on the crustal thickness derived from H-κ stacking.

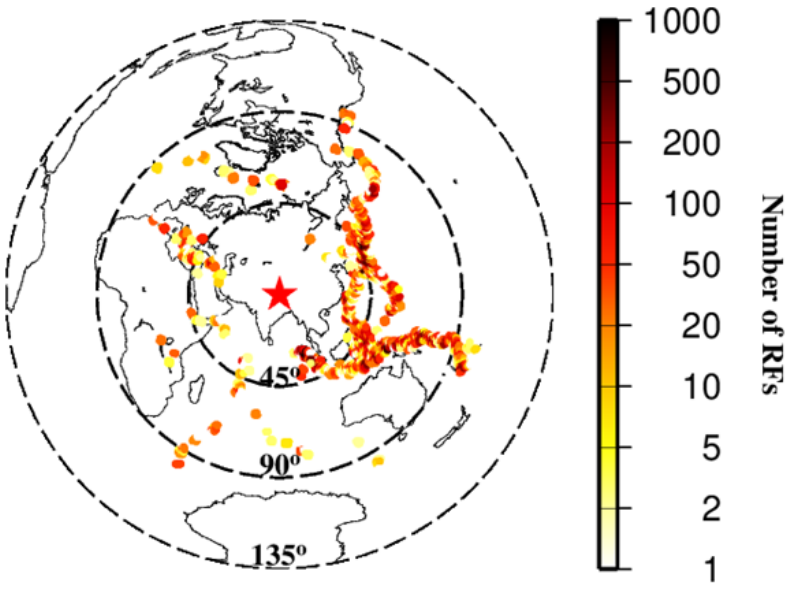

Figure 2. Azimuthal equidistant projection map showing the number of P-to-s receiver functions in the circles with a radius used for the crustal anisotropy analysis. The red star marks the center of the Hi-CLIMB seismic arrays.

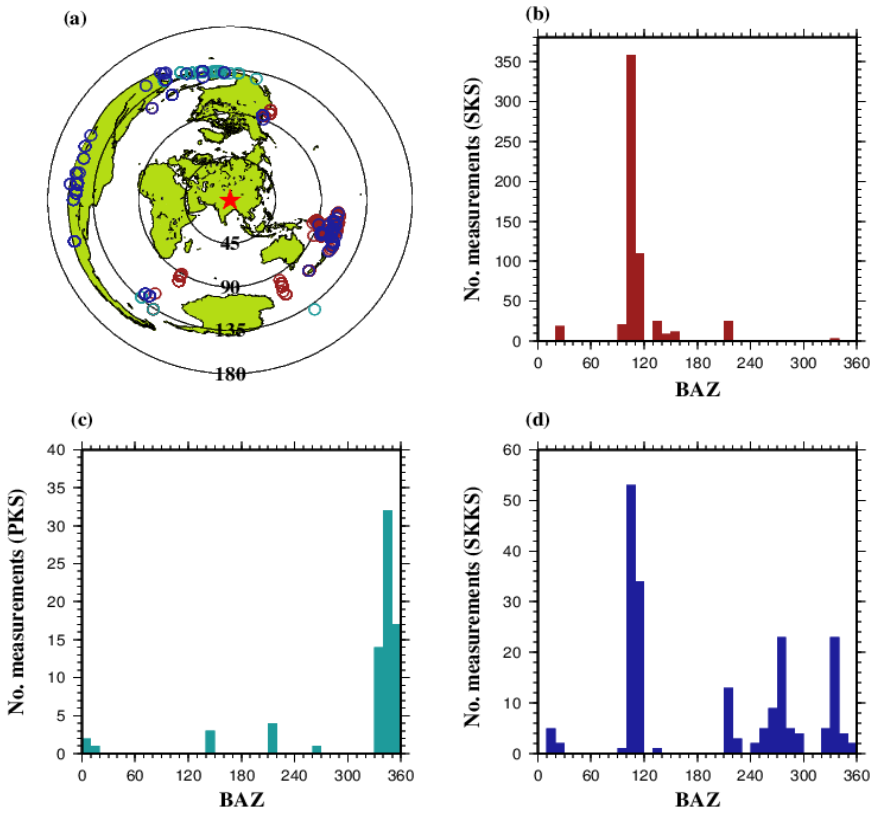

Figure 3. (a) Azimuthal equidistant map showing the distribution of the earthquakes used in this study. The events of the SKS, PKS, and SKKS are shown in red, azure, and blue, respectively. The red star marks the center of the study area. (b) Histogram showing the number and the back-azimuth distribution of the SKS phases. (c) Same as (b) but for PKS. (d) Same as (b) and (c), but for SKKS.

2.2. MEASUREMENTS OF SEISMIC ANISOTROPY USING SHEAR WAVE SPLITTING

The computation of the optimal splitting parameters from PKS, SKS, and SKKS (collectively known as XKS) is based on the transverse energy minimization method (Silver & Chan, 1991). The selected events for the SWS analysis have magnitudes (Mw) greater than 5.5 and epicentral distances between 84° and 180°. These events were band-pass filtered within the frequency range of 0.04 to 0.5 Hz. Events with a signal-to-noise ratio (SNR) less than 4.0 were discarded (Liu & Gao, 2013), resulting in 1348 qualifying

events (Figure 3). Individual shear wave splitting parameters are manually checked and ranked following the procedure described in Liu and Gao (2013). A total of 851 high-quality individual splitting parameters are obtained for further analyses (Figure 4). Note that at some stations, while SKS and SKKS result in null measurements (Figures S3a and S3b), the inclusion of the PKS phase which is mostly from the north (Figure 3c), leads to well-defined measurements (Figure S3c).

2.3. ESIMATION OF ANISOTROPY DEPTH

The XKS splitting parameters have excellent horizontal resolution due to the near-vertical incidence angle, however, the vertical resolution is relatively poor (Silver, 2006). To assess the anisotropy depth accounting for the XKS splitting measurements, the variation factor (F_v) is calculated with the optimal depth corresponding to the minimum variation factor (Liu & Gao, 2011). The study area is divided into three sub-blocks based on the characteristics of the observed splitting parameters (Figure 4a). For each sub-block, the individual splitting measurements are grouped into a series of circular bins with a radius of 0.2°, and a spacing distance of 0.2°. We calculate the standard deviation (SD) for each circle and then average them to obtain the SD value for a candidate anisotropy depth ranging from 0 km to 250 km, with a step increment of 50 km (Figures S4, S5, and S6).

2.4. CHARACTERIZATION OF MULTILAYER ANISOTROPY

The individual SWS measurements are systematically analyzed to distinguish between simple and complex anisotropy at each station. A 90^o periodicity observed in

terms of fast orientation and splitting time against the BAZs serves as a robust indicator of multi-layered anisotropic structures near the observation location (Silver & Savage,1994; Gao & Liu, 2009; Rumpker & Silver, 1998), while a 180o periodicity implies dipping anisotropic structure (Frederiksen & Bostock, 2000). Conversely, single-layer anisotropy or multilayer with identical or orthogonal fast orientations presents invariant splitting parameters with azimuth. Additionally, the anisotropy may be influenced by the piercing point if events recorded by the same station sample areas with different anisotropic features (Jia et al., 2021). To enhance the azimuthal coverage, we combine measurements from nearby stations displaying similar azimuthal variation patterns. For instance, as detailed in the next section, measurements from stations H1490, H1500, H1510, H1520, H1530, and H1540 are combined for characterizing complex anisotropy. Note that for simplicity, the combined data set is named H1500. For stations with sufficient azimuthal coverage, a grid search algorithm is employed to calculate the splitting parameters from individual layers under a two-layer model (Silver & Savage, 1994; Gao & Liu, 2009).

3. RESULTS

3.1. RESULTS OF XKS SPLITTING MEASUREMENTS

A total of 43 stations have yielded reliable measurements for the interpretation of crustal anisotropy (Figure 5). The delay time for the study area ranges from 0.15 s to 1.18 s, with an average of 0.70 ± 0.28 s, which requires an anisotropy of 2-9% assuming a crustal thickness of 65 km and a Vs of 4.5 km/s. The average delay time for the crust in

our region is larger than that obtained in the studies conducted in northern and southeastern Tibet (Wu et al., 2019; Zheng et al., 2018), reflecting the significant role that the crust plays in seismic anisotropy in these areas. NE-SW fast orientations dominate the northern and southern Himalayan block while some NW-SE fast orientations are sporadically observed at stations in the central and northeast parts of the block. Nearly N-S oriented crustal anisotropy is observed in the Lhasa block. The northern Qiangtang block is characterized by mostly NW-SE oriented crustal anisotropy, while the southern Qiangtang block has NE-SW oriented anisotropy.

3.2. RESULTS OF CRUSTAL ANISOTROPY

A total of 851 high-quality individual SWS measurements, including 583 SKS, 194 SKKS, and 74 PKS, are obtained (Figure 4). To investigate spatially variable anisotropy origin, we divided the study area into three sub-blocks bounded by the sutures (Figure 4a). Unlike the previous studies (e.g., Chen et al., 2010; Fu et al., 2008; Huang et al., 2000) which report dominant null or weak splitting measurements, we find significant seismic anisotropy south of the Indus-Yarlung suture (area C in Figure 4a), with an average delay time of 1.05 ± 0.03 s. The fast orientations are E-W or NE-SW in the west of Area C, which is parallel to the mountain belt, rotate to SW-NE in the east near the Main Boundary Thrust, and return to E-W in the central part of this area. To the north of the Indus-Yarlung suture within the Lhasa block, the fast orientations show successive changes from NE-SW to W-E from the south to north, except for several measurements near 84.2°E, which are consistent with previous SWS studies (e.g., Chen et al., 2010). The largest delay time for a single measurement reaches 2.35 s near the Indus-Yarlung

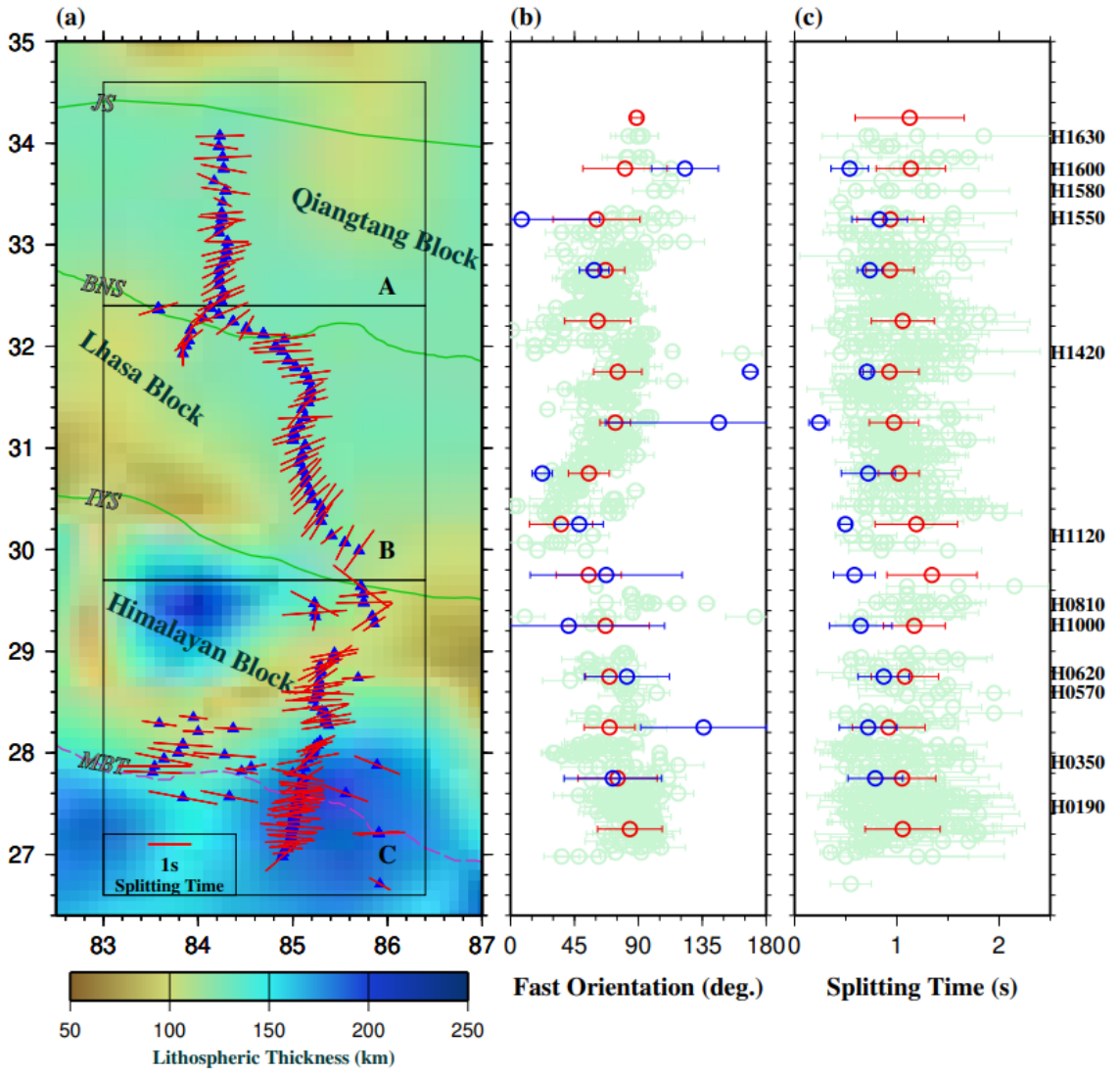

Figure 4. (a) Resulting well-defined XKS splitting parameters plotted at the ray-piercing points at 200 km depth. The red bars denote the station-averaged splitting results centered at the stations (blue triangles). (b) The distribution of fast orientations plotted against the latitude. The red bars with circles indicate the average of SWS within the 0.5° range while the blue ones are the average of crustal anisotropy. The light green bars represent the individual SWS results. (c) Same as (b) but for the splitting time.

suture. The averaged fast orientation and delay time are 60.05 ± 23.41° and 0.99 ± 0.04 s, respectively, in the Lhasa block. The fast orientations in the Qiangtang block are around

E-W, with an average of 82.29 ± 17.26° for fast orientation and 0.98 ± 0.04 s for delay time.

A total of 851 high-quality individual SWS measurements, including 583 SKS, 194 SKKS, and 74 PKS, are obtained (Figure 4). To investigate spatially variable anisotropy origin, we divided the study area into three sub-blocks bounded by the sutures (Figure 4a). Unlike the previous studies (e.g., Chen et al., 2010; Fu et al., 2008; Huang et al., 2000) which report dominant null or weak splitting measurements, we find significant seismic anisotropy south of the Indus-Yarlung suture (area C in Figure 4a), with an average delay time of 1.05 ± 0.03 s. The fast orientations are E-W or NE-SW in the west of Area C, which is parallel to the mountain belt, rotate to SW-NE in the east near the Main Boundary Thrust, and return to E-W in the central part of this area. To the north of the Indus-Yarlung suture within the Lhasa block, the fast orientations show successive changes from NE-SW to W-E from the south to north, except for several measurements near 84.2°E, which are consistent with previous SWS studies (e.g., Chen et al., 2010). The largest delay time for a single measurement reaches 2.35 s near the Indus-Yarlung suture. The averaged fast orientation and delay time are 60.05 ± 23.41° and 0.99 ± 0.04 s, respectively, in the Lhasa block. The fast orientations in the Qiangtang block are around E-W, with an average of 82.29 ± 17.26° for fast orientation and 0.98 ± 0.04 s for delay time.

Systematic investigation of the individual measurements indicates that most stations exhibit uniform splitting parameter distributions concerning the BAZ in the modulo-90o domain, indicating a single anisotropic layer with a horizontal axis of symmetry is sufficient to describe the major anisotropy characteristics. However, the two

areas near the Himalayan thrust system and the Bangong-Nujiang suture exhibit a periodicity of 90° in both fast orientations and delay times (Figure 6).

3.3. MULTILAYER ANISOTROPY IN THE HIMALAYAN AND QIANGTANG BLOCKS

Optimal splitting parameters for two anisotropic layers are determined through a grid-search approach, involving all possible parameter pairs within specified ranges (Silver & Savage, 1994; Gao & Liu, 2009). To mitigate non-uniqueness, we incorporate additional constraints by fixing the splitting parameters for the upper layer using the results obtained from the crustal anisotropy. For Station H0230, the values obtained for the lower layer (77.0°, 0.65 s) and the upper layer (-69.0°, 0.60 s), without any constraints using the results from crust anisotropy in the Himalayan block (station H0230, Figures S7a, S7c), are consistent with those derived under the assumption that the anisotropy of upper layer originates from the crust (Figure 6a). However, significant differences in the resulting two-layer parameters are found for Station H1500. Without constraining the upper layer, the splitting parameters are (40.0°, 1.10 s) for the lower layer and (-70.0°, 0.60 s) for the upper layer (Figures S7b and S7d), while by fixing the fast orientations of the upper layer to the parameters obtained from the crust, the resulting values become (-1.0°, 0.60 s) for the lower layer and (69.1°, 1.10 s) for the upper layer (Figures S7e and S7g). This discrepancy is most likely related to the well-known non-uniqueness of the grid-searching process (Savage & Silver, 1994). To reduce the non-uniqueness, by considering the extremely strong crustal anisotropy with a delay time of 1.04 s in the area, we place a constraint of a larger delay time for the upper layer compared to that of the lower layer. The resulting splitting parameters are (25.0°, 0.65 s)

for the lower layer and (81.0°, 0.70 s) for the upper layer (Figure S7f and S7h), which are similar to the results when the upper layer is assumed to be the crust (Figures 6b and 6d). Across all models tested, the fast polarization orientation of the upper layer predominantly aligns with the east-west direction, while that of the lower layer aligns with the north-south direction.

3.4. OPTIMAL DEPTH OF THE OBSERVED ANISOTROPY

The optimal anisotropy depth in the Qiangtang block ranges from a few km to 50 km (Figure S4), suggesting that crustal and upper-most mantle anisotropy is responsible for the observed splitting measurements in the block. Conversely, in the Lhasa block, the minimum SD is located at a depth of approximately 150 km (Figure S5), slightly deeper than the lithospheric thickness of approximately 130 km (Pasyanos et al., 2014), implying that the primary source of anisotropy is probably located at the lithosphere-asthenosphere transitional zone. The anisotropy depth estimated for the Himalayan block is approximately 200 km (Figure S6), indicating that the anisotropy is present in the upper asthenosphere, given that the thickness of the lithosphere in this block ranges from 150 km to 190 km (Pasyanos et al., 2014).

4. DISCUSSIONS

4.1. SIGNIFICANT CRUSTAL FLOW IN THE QIANGTANG BLOCK

In the Qiangtang block, the dominant fast orientation of crustal anisotropy is E-W (Figure 5), which is consistent with the proposed direction of mid-to-lower crustal channel flow (Agius & Lebedev, 2017; Klemperer, 2006; Li et al., 2022; Tao et al.,

2022). An independent piece of evidence of strong crustal anisotropy comes from the resulting 0-50 km for the optimal depth estimation using XKS splitting measurements (Figure S4). Results from two-layer fitting for the combined data set in the southern part of the Qiangtang block (Figure 6b) also suggest that the crust is strongly anisotropic with a nearly E-W fast orientation. The splitting times range from 0.35-1.04 s, suggesting an anisotropy magnitude from 4-9 % for a 50 km thick middle and lower crust. This is in agreement with previous crustal anisotropy studies in the Tibetan Plateau. For instance, Wu et al. (2015) report the delay time of the mid-to-lower crust beneath the western Tibet plateau ranges from 0.45 s to 1.30 s, requiring an anisotropy of 5-15%.

Agius and Lebedev (2017) measured crustal anisotropy at multi-station experiments in the central Tibetan plateau and revealed E-W fast orientations and splitting times ranging from 0.25-0.80 s. They explain the observations as the alignment of the mica crystals driven by horizontal flow. Zhang et al. (2023) measured anisotropy at some of the stations that we used in this study and obtained similar E-W-orientated crustal anisotropy with a delay time of around 1.0 s near the Bangong-Nujiang suture. Our measurements using integrated receiver function analysis and XKS splitting provide additional evidence for eastward crustal flow in the Qiangtang block (Figure 7).

4.2. POTENTIAL MID-LOWER CRUSTAL FLOW IN THE LHASA BLOCK

Our crustal anisotropy measurements reveal that the fast orientations in the Lhasa block are sub-parallel to N-S trending rifts (Figure 5), which are commonly found in the Lhasa block and are generally considered to be the result of N-S compression (Yin & Harrison, 2000). Numerous previous studies have demonstrated that extensional fractures

in the top several kilometers of the upper crust formed in compression domains can produce anisotropy with a fast orientation that is parallel to the direction of the compressional stress (Crampin, 1981). In areas with a normal crustal thickness, the splitting times are normally smaller than 0.1 s (e.g., Shi et al., 2013), while in areas with thickened crust such as the eastern Tibetan Plateau, it could amount to 0.2 s (e.g., Hu et al., 2019), this is significantly smaller than the splitting times that we observed in the Lhasa block, which range from 0.30-0.97 s (Figure 5). Therefore, other mechanisms besides stress-induced anisotropy must have contributed to the observed crustal anisotropy.

Previous studies using ambient noise (e.g., Guo et al., 2009) and body wave tomography (e.g., Hung et al., 2010) have identified a pronounced low-velocity zone in the lower crust beneath the Lhasa block, indicating a mechanically weak middle to lower crust (Pang et al., 2018; Jiang et al., 2014; Hung et al., 2010). One possible mechanism is southward mid-to-lower crustal flow that has been proposed by some studies based on isotopic observations and seismic velocity profile (Figure 7; Klemperer, 2006). Assuming that the extensional fractures in the upper crust contribute to 0.2 s of the observed crustal anisotropy, the mid-to-lower crustal flow accounts for about 0.5 s of the crustal splitting time. This is significantly smaller than that inferred for the mid-to-lower crustal flow underneath the Qiangtang block and may suggest a weaker channel flow in the former area. This may explain the diverse perspectives among studies concerning the necessity of the existence and direction of the channel flow in the Lhasa block among previous studies (Beaumont et al., 2004; Kapp et al., 2005).

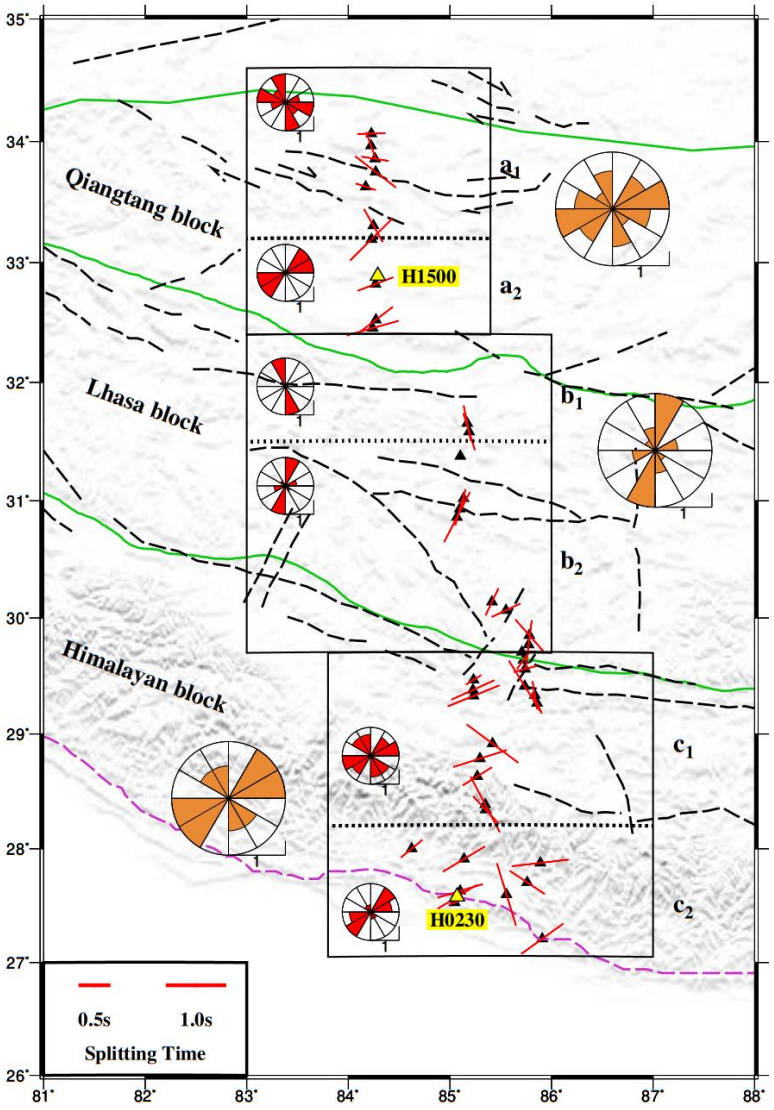

Figure 5. Resulting splitting parameters for the whole crust. The crustal anisotropy measurements from individual stations are shown as red bars. The rose diagrams in the blocks are the results of the sub-block separated by dashed lines, and the ones outside the block are the results of the blocks marked as solid rectangles. The two red triangles mark the location of station H0230 and H1500.

4.3. MANTLE FLOW FIELDS BENEATH THE LHASA BLOCK

The fast orientations observed from XKS splitting in the Lhasa block show a systematic and gradual variation, from NE-SW in the southern portion of the block to E-

W in the northern block. The splitting times from XKS splitting analysis are about twice of those from crustal anisotropy analysis at most of the stations in the area, suggesting a strong mantle contribution. Depth estimations of anisotropy within the Lhasa block indicate that its primary source is the lithosphere-asthenosphere transition zone. The fast orientations observed in the southern part of the Lhasa block are sub-parallel to the direction of the plate motion of the Indian plate (Figure 1). Numerous studies have shown that a subducting slab can induce a corner flow which in turn leads to fast orientations that are parallel to the direction of subduction (e.g., Fu et al., 2008). Therefore, the NE-SW fast orientations in the southern Lhasa block could be attributed to corner flow associated with the subduction of the Indian slab (Figure 7). The existence of NE-SW-oriented anisotropy in the southern Lhasa block can provide independent evidence for the presence of a mantle wedge, which is one of the debated issues on Tibetan mantle tomography (Hung et al., 2010; Zhang et al., 2016).

Progressing northward, the transition to an E-W anisotropy orientation could be interpreted as a result of the blockage of dispatched mantle flow associated with the advancing Indian slab by the thick lithosphere in the middle and northern parts of the Lhasa block (Figures 4a and 7). This model suggests that the direction of the movement of the asthenospheric material is in general agreement with that of the surface material. The flow fields proposed here to explain our XKS splitting results are similar to what is proposed by some other studies. For instance, a shift from N-S to E-W in the fast polarization orientation over brief spans has been identified in the eastern Tibetan Plateau (Lei et al., 2019), which is explained as the consequence of material extrusion flow and orthogonal mantle convection within the broad mantle wedge model.

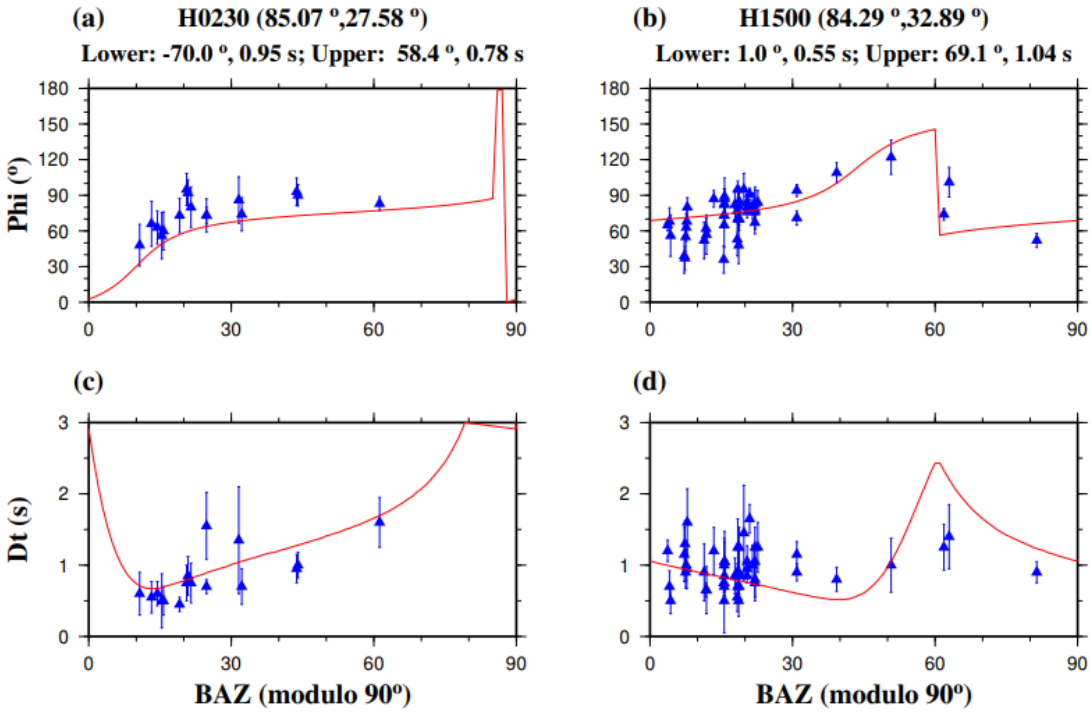

Figure 6. XKS splitting measurements exhibiting a 90° BAZ periodicity. (a) Fast orientations of the station H0230 plotted against BAZ in modulo 90°. (c) Variation of splitting time of the station H0230 plotted against BAZ in modulo 90°. (b), (d) are the same as (a), (c), respectively, but for the station H1500 and its adjacent stations. The green lines rule out the possibility that the fast orientations and the BAZ of the ray are parallel or perpendicular to each other. The red lines demonstrate the theoretical XKS distributions based on the splitting parameters of the upper and lower layers shown above.

4.4. OROGEN-PARALLEL MANTLE FLOW IN THE SUB-SLAB REGION BENEATH THE HIMALAYAN BLOCK

In the Himalayan block, where most previous studies suggest a lack of observable azimuthal anisotropy (e.g., Chen et al., 2010; Fu et al., 2008), the fast orientations from XKS splitting are mostly E-W which are sub-parallel to the strike of the orogenic belt (Figure 4a). In addition, a nearly E-W lower layer anisotropy is revealed at Station H0230 (Figure 6a). Furthermore, the observed crustal anisotropy has spatially variable fast orientations and significantly smaller splitting times, and the estimated depth of

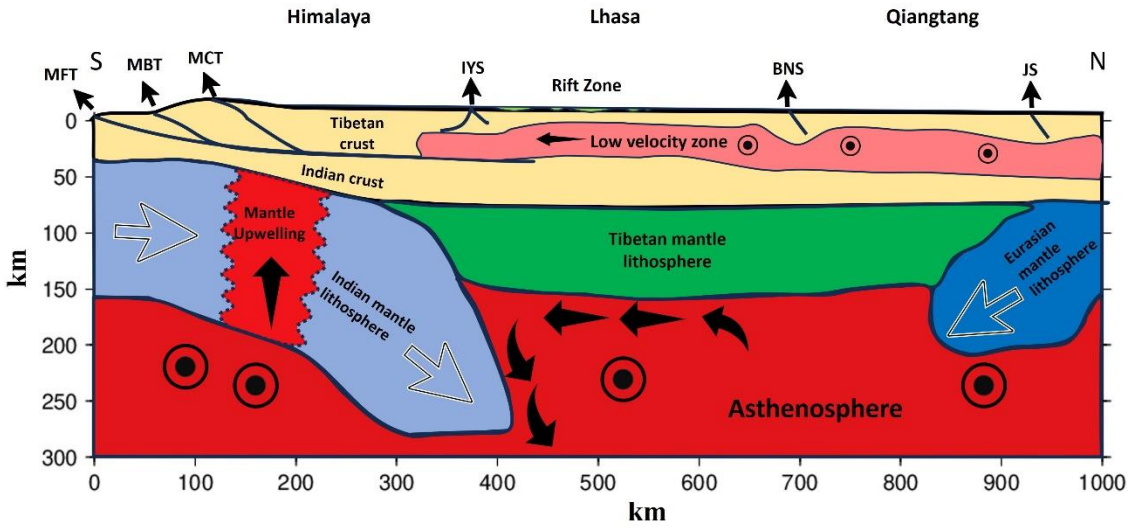

Figure 7. Model illustrating the structure and driving mechanisms behind the observed anisotropy in the southern Tibetan Plateau (Modified from Wang et al., 2016). The E-W fast polarization orientations at the southern end of the study area result from asthenosphere flow. Slab breakage facilitates the upwelling of asthenospheric material. The mantle anisotropy in the Lhasa block, delineated by the Indus-Yarlung suture and the Bangong-Nujiang suture is induced by corner convective flow and the eastward movement of the mantle, while crust anisotropy is controlled by rifts and southward crustal flow. The dominant E-W anisotropy in the Qiangtang block characters the eastward mid to lower crust flow.

anisotropy in this area is about 200 km, which is comparable to or deeper than the estimated lithospheric thickness (Figure 4a; Pasyanos et al., 2014). These observations suggest that the observed anisotropy is mostly from the upper asthenosphere. A viable mechanism for trench parallel anisotropy in typical subduction zones is sub-slab trench parallel flow, most likely driven by slab rollback (Russo & Silver, 1994). However, slab rollback is only reported for the eastern portion of the Indo-Burma subduction system (Lee et al., 2016). Therefore, we propose that one of the possible explanations for the observed E-W fast orientation from XKS splitting in the Himalayan block is the westward continuation of slab rollback-induced flow along the Burma subduction zone

(Liu et al., 2019). The westward absolute plate motion of the Eurasian plate in the hotspot reference frame (Gripp & Gordon, 2002) may also contribute to the E-W anisotropy (Singh et al., 2016), although the slow rate of motion (23 mm/yr) might be too small to produce significant azimuthal anisotropy (Kendall et al., 2022).

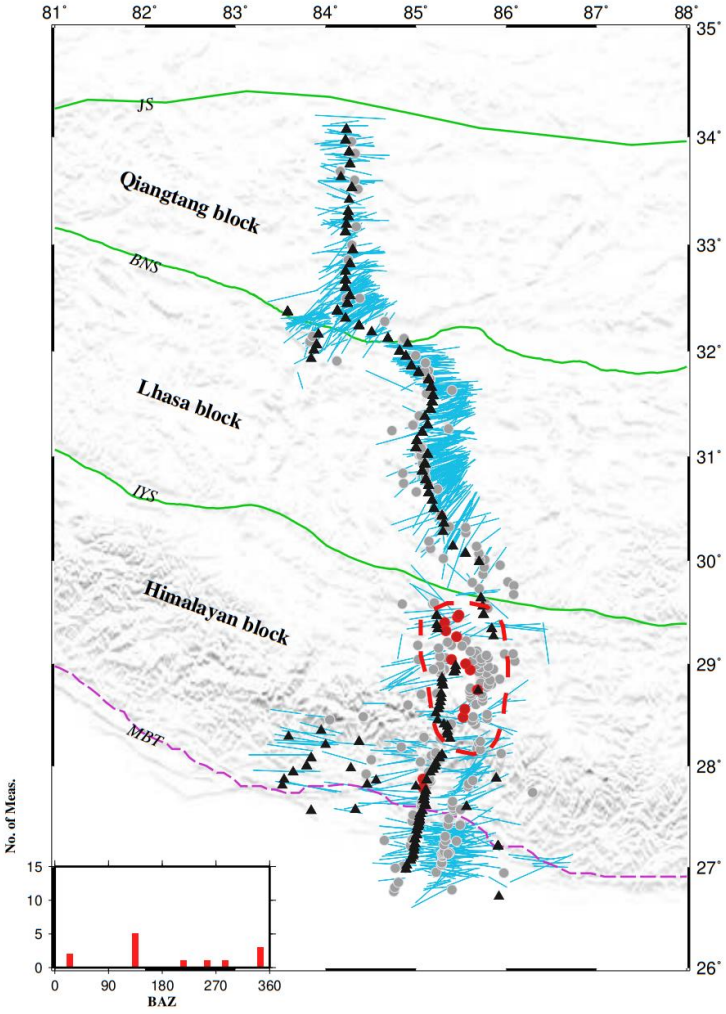

Figure 8. Distribution of induvial XKS splitting parameters (blue bars) and true null measurements (red circles) as well as pseudo or unknown null measurements (gray circles) for the study area. Black triangles are seismic stations. Dashe red lines outline an area with a significant clustering of true null measurements. The histogram in the lower left corner displays the number of true null measurements.

4.5. POSSIBLE MANTLE UPWELLING THROUGH A SLAB WINDOW

Null measurements are characterized by a lack of XKS energy on the transverse component and can be caused by two situations (Silver & Chan, 1991). The first is that the mantle and crust from the core-mantle boundary to the surface sampled by the XKS ray path are seismically isotropic ("true null"), and the second is pseudo null, which occurs when the fast orientation is parallel or orthogonal to the BAZ. For the first situation, null measurements present for events with different BAZs, and for the second situation, null measurements are only from events with similar or orthogonal BAZs. In this study, we apply a three-step procedure to determine true null measurements. First, the coordinates of the ray piercing points of all the null measurements at the estimated anisotropy depth for a given area are calculated. Second, the area is divided into consecutive non-overlapping rectangle bins with a dimension of 0.2° by 0.2° at both the E-W and N-S directions, and the circular average of the BAZs of all the null measurements for each bin is calculated. Third, the BAZs of the individual null measurements in the bin are compared with the average BAZ in the bin to determine if they are true nulls. Specifically, if a null measurement with a difference between the BAZ and the averaged BAZ is greater than 15.0° in the modulo-90° domain, it is considered a true null (red circles in Figure 8). Admittedly, the resulting spatial distribution of the true null measurements would vary when different bin sizes and threshold values are used. However, testing using different parameters suggests that the area with a concentration of true nulls would not change.

Using the above procedure, an area with concentrated true null measurements in the northern part of the Himalayan block has been identified (Figure 8). For most of the

null measurements in this area, the events are from the southeast (lower-left inset in Figure 8). This area is also characterized by an absence of well-defined splitting measurements, which independently confirms the lack of observable azimuthal anisotropy. In this area, seismic tomography studies (Li & Song, 2018; Nie et al., 2020) imaged a discontinuity in the subducted Indian slab and interpreted it as a slab tear. In addition, geochemical investigations (e.g., Chen et al., 2021) reported anomalously high Sr/Y ratios in adakitic Miocene rocks in the area, and proposed a deep mantle origin, probably from upwelling through a slab tear. On the basis of these observations, we hypothesize that the pervasive true nulls in this area result from mantle upwelling through the slab tear (Figure 7).

5. CONCLUSIONS

Joint analyses of shear wave splitting and receiver function measurements in the south-central Tibetan plateau reveal systematic variations in crust and mantle seismic anisotropy. The expanded back azimuth coverage, archived through an extended epicentral distance range over previous studies and the inclusion of PKS and SKKS phases in addition to SKS, contribute to a substantial enhancement in the quality and quantity of splitting measurements, especially south of the Indus-Yarlung suture where null measurements were reported by previous studies. Using crustal anisotropy results and optimal anisotropy depth estimates, this comprehensive approach allows better identification and characterization of complex anisotropy patterns. Standard deviation analysis of fast orientations suggests that the source of anisotropy is primarily situated

within the mid to lower crust in the Qiangtang block and extends into the upper asthenosphere in both the Himalayan and Lhasa blocks induced by slab subduction and slab rollback along the Burma subduction zone. The clustering of true null measurements near the Bangong-Nujiang suture suggests a significant upwelling of asthenospheric material, likely driven by slab tearing.

ACKNOWLEDGMENTS

We thank the Seismological Facility for the Advancement of Geoscience (SAGE) Data Management Center for providing access to the seismic data used in this study. The service for downloading seismic data is funded through the Nation Science Foundation's Seismological Facility for the SAGE Award under Cooperative Agreement EAR-1724509. The study was partially supported by the U.S. National Science Foundation under awards 1830644 and 2149587 to K.L. and 1919789 to S.G.

DATA AVAILABILITY

All the data used in the study are publicly available from the Seismological Facility for the Advancement of Geoscience Data Management Center, using the BREQ_FAST data requesting procedure (https://ds.iris.edu/ds/nodes/dmc/forms/breqfast-request/). Note that email-based BREQ_FAST request will be replaced by FetchData (https://github.com/EarthScope/fetch-scripts) and ROVER (https://earthscope.github.io/rover). The seismic data includes the networks XF (10.7914/SN/XF_2002; Nabelek, 2002), and YL (10.7914/SN/YL_2001; Sheehan, 2001),

Y2 (10.7914/SN/Y2_2007; Roecker & Levin, 2007). The specific data requesting parameters including the cut-off magnitude and epicentral distance range can be found in Section 3. To demonstrate the quality of the measurements, during the review process of this paper, the manually verified XKS results can be found at https://web.mst.edu/csgg2/06_Tibet_SWS_V6/ and the crustal anisotropy results from receiver functions can be reviewed at https://web.mst.edu/csgg2/07_Tibet_Pms/. Figures were made with Generic Mapping Tools version 4.5.7 and 6.2.0 (Wessel et al., 2019).

APPENDIX

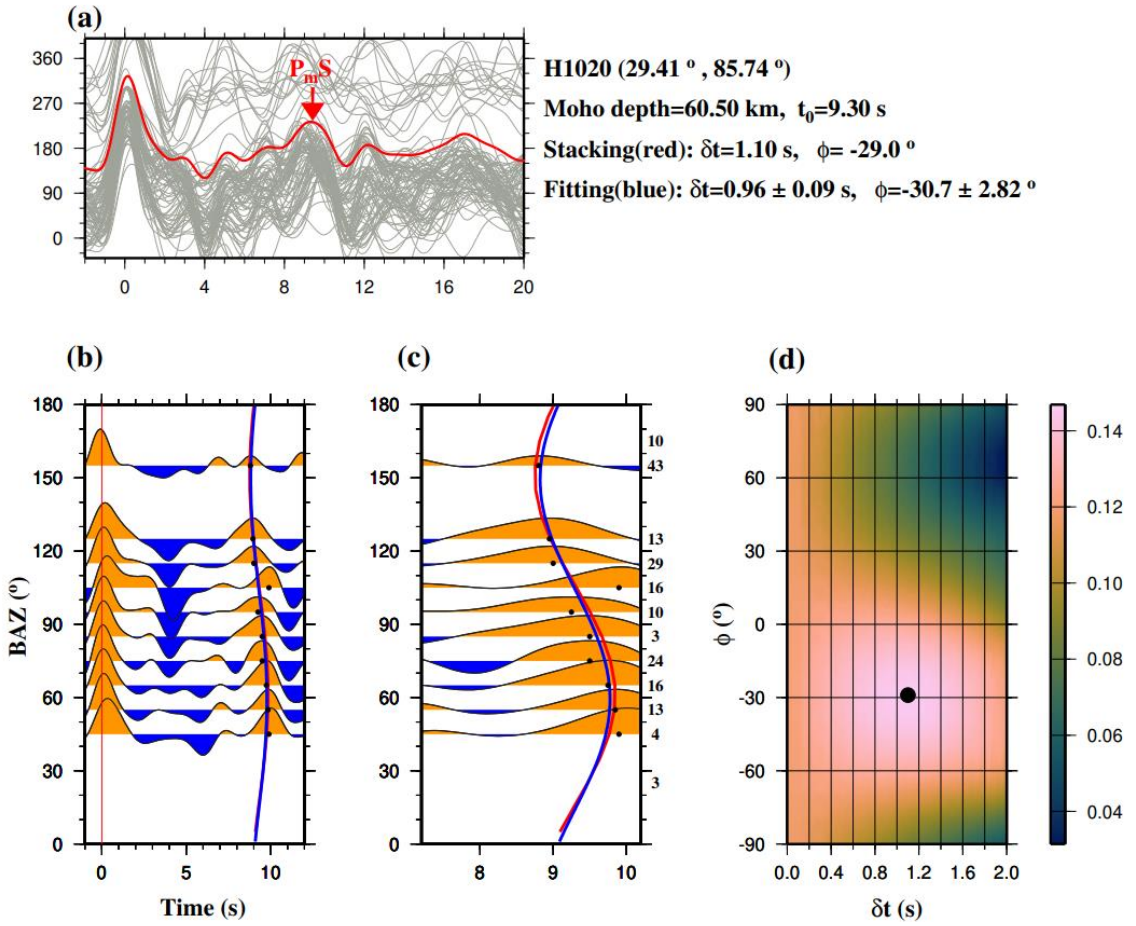

Figure S1. Crustal anisotropy measurement using receiver functions obtained at Station H1020. (a) Receiver functions plotted against the incoming back azimuth shown in gray traces. The red trace is achieved by stacking all the receiver functions. (b) Azimuthal band-averaged receiver functions with a step of 10°. The black dots show the peak in the time segment containing the P-to-S conversion at the Moho (PmS). Predicted PmS arrivals computed by using the optimal pair of anisotropy parameters (the fast orientation, ϕ and the splitting time, δt) based on the non-linear least square procedure are shown in the red curve, while the resultant arrivals obtained by grid searching candidate values and stacking (Rumpker et al., 2014) are denoted by the blue curve. (c) Same as (b) but for the time window of 7 s to 10 s.(d) Stacking amplitudes as a function of candidate pairs of ϕ and δt. The black dot marks the optimal pair of anisotropy parameters that results in the maximum stacking amplitude.

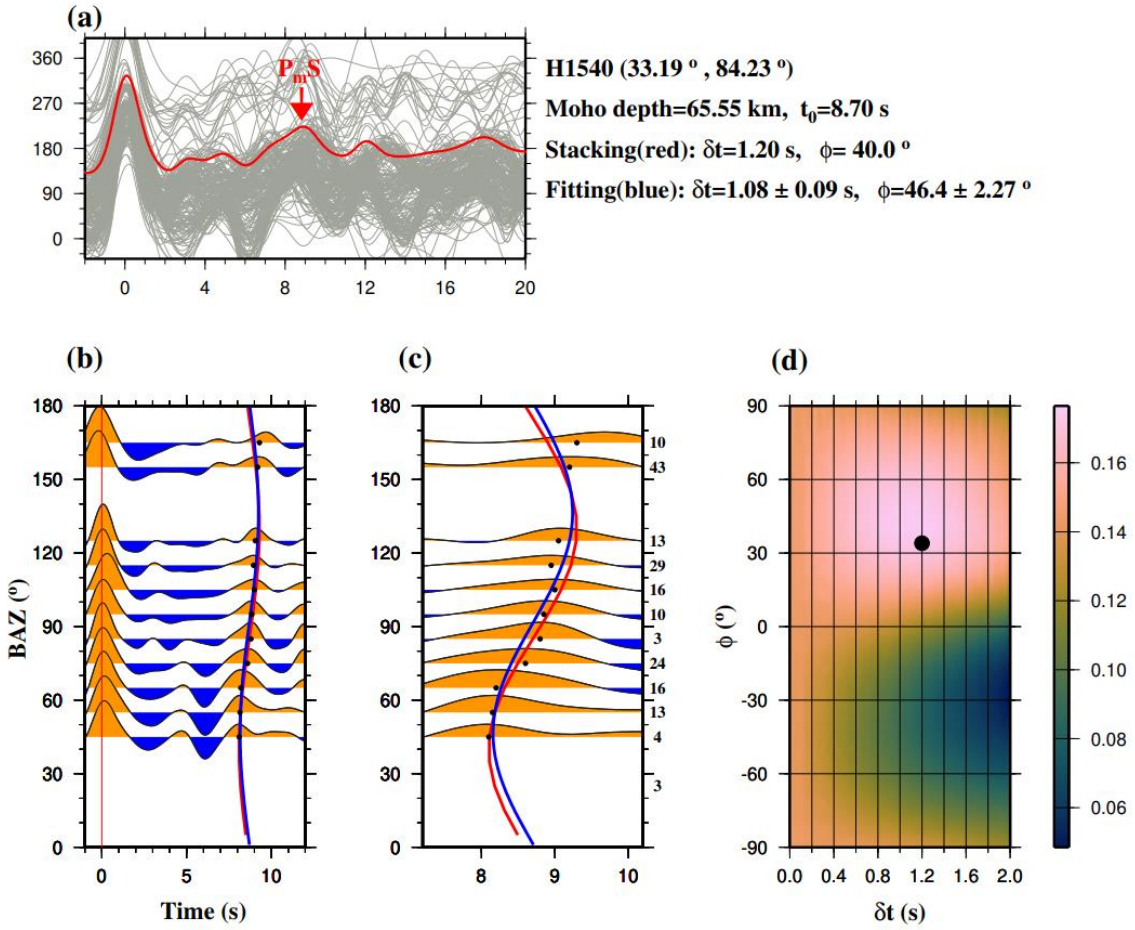

Figure S2. Same as Figure S1 but for the station H1540.

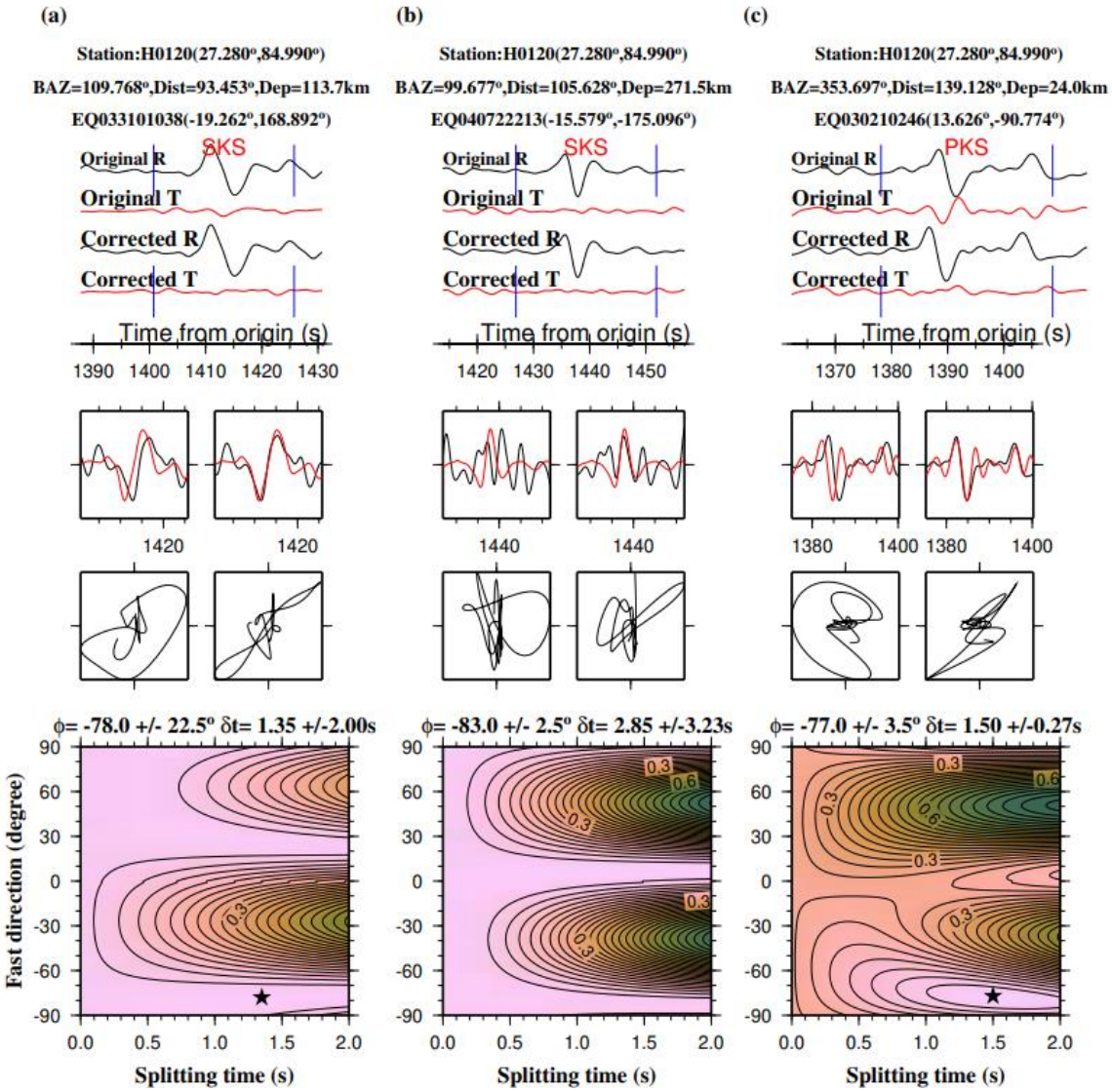

Figure S3. Examples of null (a and b) and good shear wave splitting (SWS) measurements (c) from station H0120. Plots from top to bottom denote the original and corrected radial and transverse waveforms, seismograms of fast and slow components before (left) and after (right) correction, particle motion patterns before (left) and after (right) advancing the slow component by the optimal value of the splitting time, and the error functions shown in a form of energy contour map. The black star at the bottom corresponds to the minimum energy and thus represents the optimal pairs of splitting parameters.

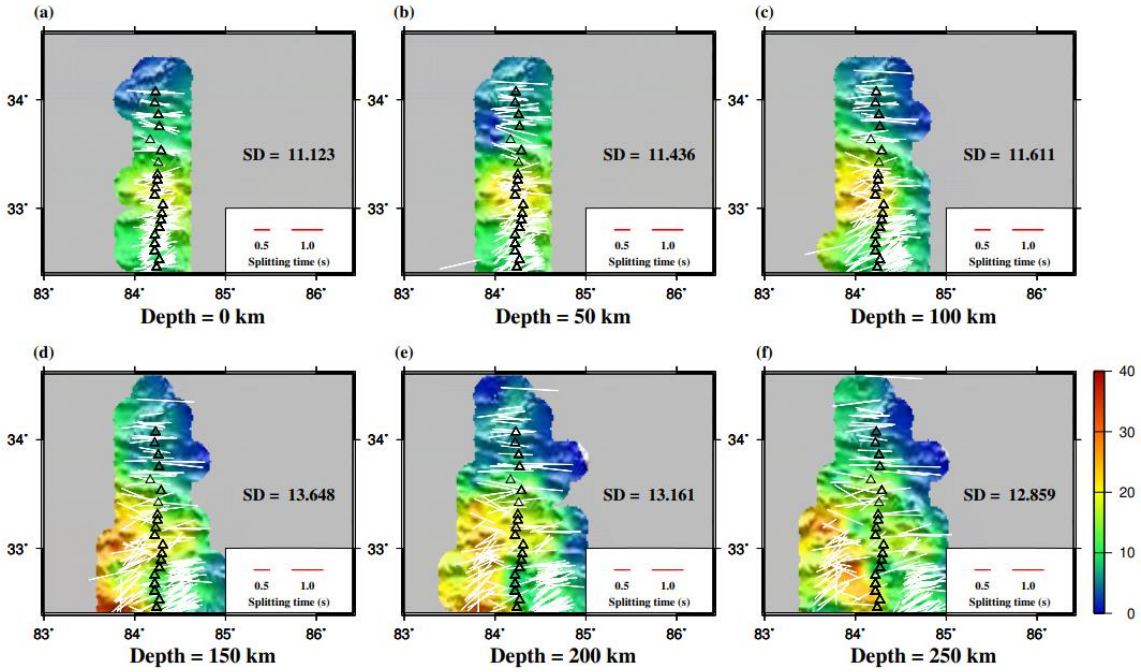

Figure S4. Standard deviation (SD) of averaged fast orientations for subblock A (Figure 4) with respect to the depth with an interval of 50 km. The individual measurements used in the computation are plotted as white bars. The depth with the minimum SD indicates the potential anisotropy origin.

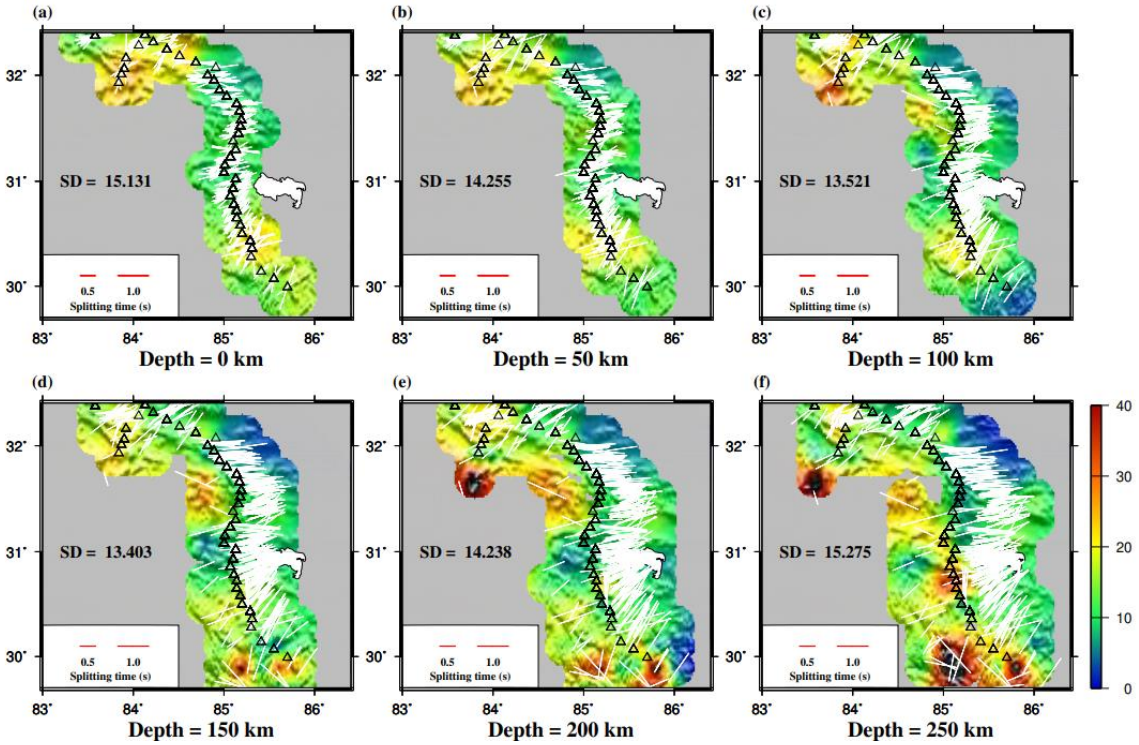

Figure S5. Same as Figure S4 but for subblock B (Figure 4).

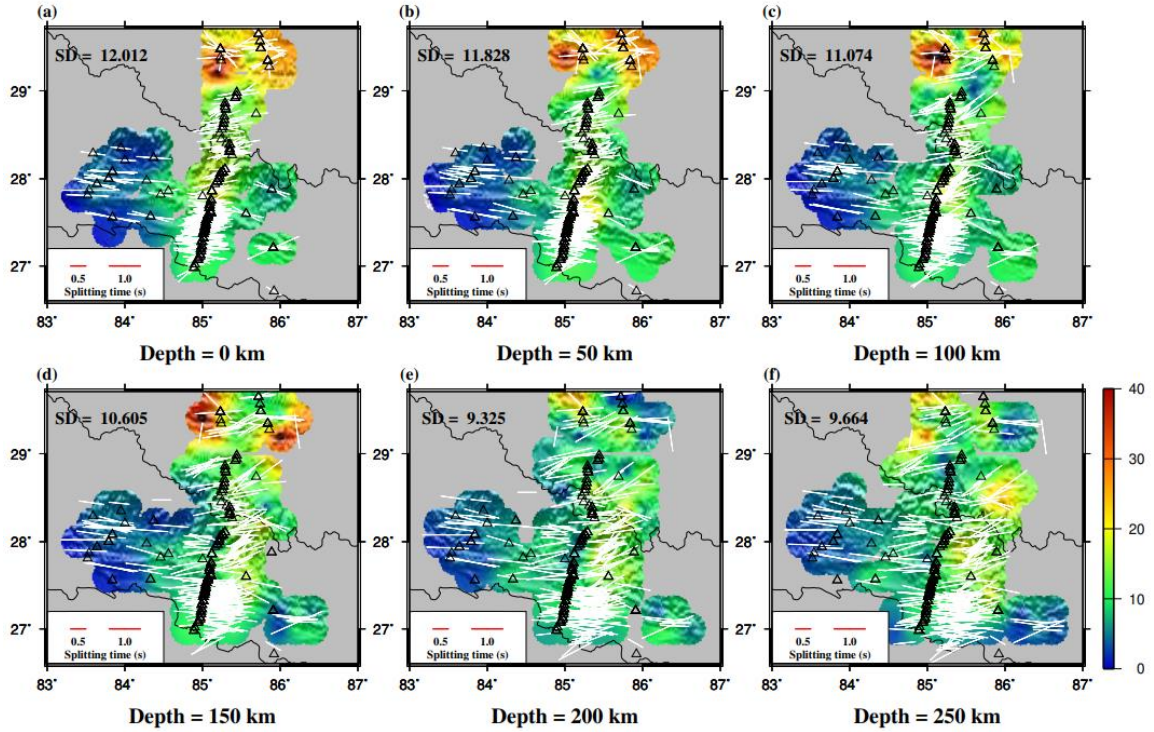

Figure S6. Same as figure S4 but for subblock C (Figure 4).

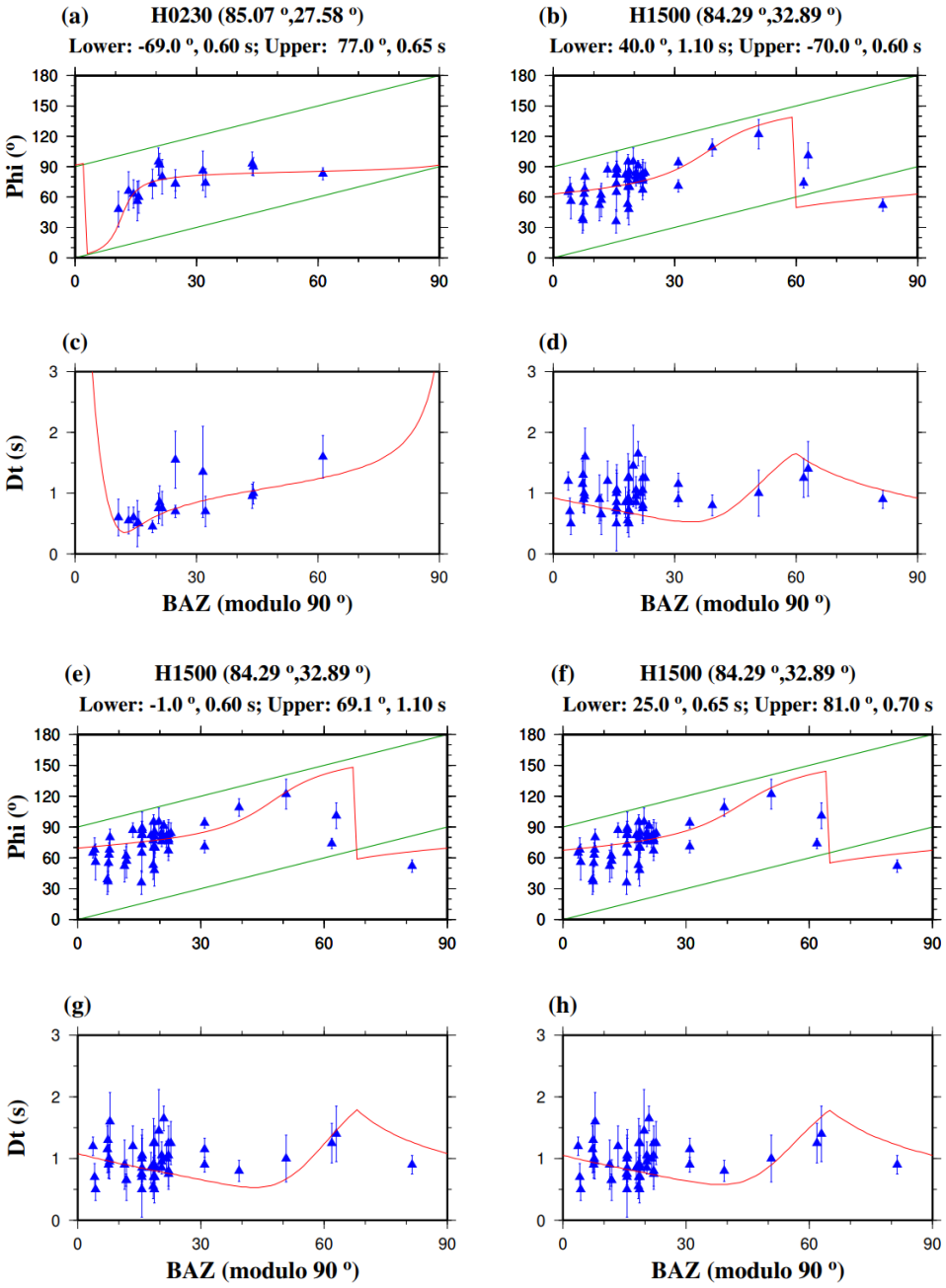

Figure S7. Individual splitting parameters (blue triangles) and predicted values calculated using the optimal pairs of splitting parameters. (a) and (c) give the optimal splitting pairs for Station H0230, which are obtained by freely searching all candidate pairs of splitting parameters. (b, d) Same as (a, c) but for Station H1500. (e, g) Same as (b, d) but with the fast orientation of the upper layer being fixed. (f, h) Same as (b, d) but setting the splitting time of the upper layer greater than that of the lower layer.

Table S1. Well-defined Individual Splitting Parameters.

Station	Phase	Event	St-lat.	St-lon.	Phi	STD of Phi	DT	STD of DT	BAZ	Ev-Lat.	Ev-Lon.	Ev-Dep.	R.
BUNGxx_YL	SKKS	EQ013321432	27.9	85.9	-62	18.0	1.1	0.5	358.6	15.6	-93.1	84.9	A
BUNGxx_YL	SKKS	EQ020162309	27.9	85.9	-74	9.5	1.2	0.3	358.6	15.5	-93.1	80.2	A
H0010x_XF	SKS	EQ022900423	27.0	84.9	36	12.5	0.5	0.1	105.1	-19.8	-178.4	627.6	A
H0010x_XF	SKS	EQ032331212	27.0	84.9	62	8.5	1.2	0.5	133.8	-45.1	167.1	28.0	B
H0010x_XF	SKS	EQ040692256	27.0	84.9	48	15.5	1.4	0.7	117.0	-32.3	-178.4	18.4	B
H0020x_XF	SKS	EQ022900423	27.0	84.9	74	11.5	0.4	0.1	105.1	-19.8	-178.4	627.6	A
H0020x_XF	SKS	EQ022951139	27.0	84.9	-88	13.0	0.6	0.3	105.8	-20.6	-178.4	549.0	B
H0040x_XF	PKS	EQ030210246	27.1	84.9	-74	17.0	0.8	0.4	353.6	13.6	-90.8	24.0	A
H0040x_XF	PKS	EQ040351159	27.1	84.9	-82	5.5	1.3	0.3	339.8	8.4	-82.9	29.2	B
H0040x_XF	SKS	EQ032331212	27.1	84.9	86	7.5	0.7	0.1	133.8	-45.1	167.1	28.0	B
H0040x_XF	SKS	EQ032960758	27.1	84.9	-88	16.0	0.7	0.3	109.4	-23.7	179.8	503.8	A
H0050x_XF	SKS	EQ031171603	27.1	85.0	-84	10.0	1.0	0.4	110.9	-20.9	169.8	77.4	B
H0050x_XF	SKS	EQ032331212	27.1	85.0	71	10.0	0.8	0.3	133.8	-45.1	167.1	28.0	B
H0060x_XF	SKS	EQ032331212	27.1	85.0	77	16.5	0.7	0.2	133.8	-45.1	167.1	28.0	B
H0070x_XF	SKKS	EQ023521412	27.1	85.0	-86	9.0	1.1	0.2	217.8	-57.1	-25.0	10.0	B
H0070x_XF	SKKS	EQ032731408	27.1	85.0	69	16.5	0.9	0.6	114.9	-30.4	-177.4	10.0	B
H0070x_XF	SKS	EQ031171603	27.1	85.0	-80	2.5	1.7	0.4	110.9	-20.9	169.8	77.4	B
H0070x_XF	SKS	EQ032331212	27.1	85.0	80	12.0	0.6	0.2	133.8	-45.1	167.1	28.0	B
H0070x_XF	SKS	EQ033060532	27.1	85.0	61	9.5	1.0	0.5	134.1	-45.2	166.5	10.0	B
H0070x_XF	SKS	EQ033612238	27.1	85.0	-77	3.0	1.5	0.4	111.5	-21.7	169.8	10.0	B
H0080x_XF	SKS	EQ032650445	27.2	85.0	-86	5.5	1.2	0.2	330.6	19.8	-70.7	10.0	A
H0080x_XF	SKS	EQ032731408	27.2	85.0	-84	19.0	0.9	0.5	114.9	-30.4	-177.4	10.0	B
H0090x_XF	SKKS	EQ032731408	27.2	85.0	71	17.5	0.7	0.5	114.9	-30.4	-177.4	10.0	A
H0090x_XF	SKKS	EQ033090058	27.2	85.0	-89	3.5	1.8	0.2	329.9	5.0	-77.8	33.0	B
H0090x_XF	SKS	EQ032331212	27.2	85.0	-75	9.0	0.9	0.2	133.8	-45.1	167.1	28.0	B
H0100x_XF	PKS	EQ030210246	27.2	85.0	-84	2.5	1.8	0.4	353.7	13.6	-90.8	24.0	B
H0100x_XF	SKKS	EQ032731408	27.2	85.0	84	13.5	0.8	0.3	114.9	-30.4	-177.4	10.0	A
H0100x_XF	SKKS	EQ033090058	27.2	85.0	82	11.0	1.4	0.5	329.9	5.0	-77.8	33.0	B

Table S1. Well-defined Individual Splitting Parameters. (cont.)

H0100x_XF	SKS	EQ032331212	27.2	85.0	-77	6.0	0.9	0.2	133.8	-45.1	167.1	28.0	A
H0100x_XF	SKS	EQ032731408	27.2	85.0	-80	19.5	1.1	0.6	114.9	-30.4	-177.4	10.0	B
H0120x_XF	PKS	EQ030210246	27.3	85.0	-77	3.5	1.5	0.3	353.7	13.6	-90.8	24.0	A
H0120x_XF	SKKS	EQ032650445	27.3	85.0	-87	4.5	1.7	0.3	330.7	19.8	-70.7	10.0	A
H0120x_XF	SKKS	EQ032731408	27.3	85.0	87	11.5	1.3	0.3	114.9	-30.4	-177.4	10.0	A
H0120x_XF	SKKS	EQ033090058	27.3	85.0	-80	10.0	1.6	0.4	330.0	5.0	-77.8	33.0	B
H0120x_XF	SKKS	EQ033602126	27.3	85.0	-82	10.5	1.7	0.6	112.3	-22.3	169.3	10.0	B
H0120x_XF	SKS	EQ030040515	27.3	85.0	-84	1.5	1.7	0.2	105.4	-20.6	-177.7	378.0	B
H0120x_XF	SKS	EQ032080204	27.3	85.0	-84	3.0	1.4	0.3	105.5	-21.1	-176.6	212.9	B
H0120x_XF	SKS	EQ032331212	27.3	85.0	-85	9.0	1.1	0.2	133.8	-45.1	167.1	28.0	A
H0120x_XF	SKS	EQ032731408	27.3	85.0	-83	3.5	1.6	0.2	114.9	-30.4	-177.4	10.0	B
H0120x_XF	SKS	EQ032960758	27.3	85.0	-82	3.0	1.7	0.4	109.4	-23.7	179.8	503.8	B
H0120x_XF	SKS	EQ033060532	27.3	85.0	85	7.0	1.4	0.2	134.1	-45.2	166.5	10.0	B
H0120x_XF	SKS	EQ033592309	27.3	85.0	87	8.5	1.2	0.3	112.2	-22.3	169.5	10.0	B
H0130x_XF	PKS	EQ032160437	27.3	85.0	76	16.5	0.7	0.3	211.5	-60.5	-43.4	10.0	A
H0130x_XF	SKS	EQ022771905	27.3	85.0	88	19.5	0.6	0.3	106.3	-21.0	-179.0	621.1	A
H0130x_XF	SKS	EQ022900423	27.3	85.0	89	8.0	0.6	0.2	105.0	-19.8	-178.4	627.6	A
H0130x_XF	SKS	EQ022951139	27.3	85.0	-88	14.5	0.6	0.3	105.8	-20.6	-178.4	549.0	B
H0130x_XF	SKS	EQ030160053	27.3	85.0	88	7.5	1.2	0.3	24.3	44.3	-129.0	10.0	B
H0130x_XF	SKS	EQ030952203	27.3	85.0	-89	11.0	0.6	0.2	107.5	-16.2	167.9	177.5	A
H0130x_XF	SKS	EQ031292026	27.3	85.0	84	4.5	0.7	0.1	212.2	-48.2	32.3	10.0	B
H0130x_XF	SKS	EQ032331212	27.3	85.0	88	5.0	1.1	0.1	133.8	-45.1	167.1	28.0	B
H0130x_XF	SKS	EQ033060532	27.3	85.0	90	10.5	1.2	0.3	134.1	-45.2	166.5	10.0	B
H0150x_XF	SKKS	EQ033090058	27.4	85.0	80	18.0	1.0	0.5	330.0	5.0	-77.8	33.0	B
H0150x_XF	SKKS	EQ033611600	27.4	85.0	-82	8.0	1.5	0.6	111.8	-22.0	169.8	10.0	B
H0150x_XF	SKS	EQ022771905	27.4	85.0	-88	5.5	1.4	0.4	106.3	-21.0	-179.0	621.1	B
H0150x_XF	SKS	EQ022900423	27.4	85.0	-83	2.5	1.4	0.3	105.0	-19.8	-178.4	627.6	B
H0150x_XF	SKS	EQ022951139	27.4	85.0	-85	7.5	1.4	0.5	105.7	-20.6	-178.4	549.0	B
H0150x_XF	SKS	EQ033060532	27.4	85.0	-81	14.0	0.9	0.2	134.0	-45.2	166.5	10.0	B

Table S1. Well-defined Individual Splitting Parameters. (cont.)

H0150x_XF	SKS	EQ033610455	27.4	85.0	-79	5.5	1.3	0.4	112.1	-22.1	169.4	10.0	B
H0160x_XF	SKKS	EQ032650445	27.4	85.0	72	6.0	1.4	0.4	330.7	19.8	-70.7	10.0	B
H0160x_XF	SKKS	EQ032731408	27.4	85.0	89	12.5	1.0	0.4	114.8	-30.4	-177.4	10.0	A
H0160x_XF	SKS	EQ022771905	27.4	85.0	78	17.0	0.7	0.2	106.3	-21.0	-179.0	621.1	B
H0160x_XF	SKS	EQ022900423	27.4	85.0	83	12.0	0.7	0.2	105.0	-19.8	-178.4	627.6	A
H0160x_XF	SKS	EQ032331212	27.4	85.0	84	7.5	1.0	0.1	133.8	-45.1	167.1	28.0	B
H0160x_XF	SKS	EQ032960758	27.4	85.0	-89	8.0	0.8	0.2	109.3	-23.7	179.8	503.8	B
H0160x_XF	SKS	EQ033060532	27.4	85.0	76	16.5	1.0	0.5	134.0	-45.2	166.5	10.0	B
H0160x_XF	SKS	EQ033170249	27.4	85.0	80	5.5	1.8	0.4	149.7	-54.2	143.8	10.0	B
H0160x_XF	SKS	EQ040561652	27.4	85.0	71	19.5	0.6	0.3	104.5	-20.7	-175.0	55.8	B
H0170x_XF	SKKS	EQ032731408	27.4	85.0	-89	4.0	1.3	0.2	114.8	-30.4	-177.4	10.0	A
H0170x_XF	SKS	EQ022771905	27.4	85.0	77	9.5	0.6	0.2	106.3	-21.0	-179.0	621.1	A
H0170x_XF	SKS	EQ022900423	27.4	85.0	78	6.5	0.6	0.1	105.0	-19.8	-178.4	627.6	A
H0170x_XF	SKS	EQ022951139	27.4	85.0	74	13.0	0.5	0.1	105.7	-20.6	-178.4	549.0	B
H0170x_XF	SKS	EQ032650445	27.4	85.0	85	8.5	1.1	0.3	330.8	19.8	-70.7	10.0	B
H0170x_XF	SKS	EQ032731408	27.4	85.0	72	7.5	0.8	0.1	114.8	-30.4	-177.4	10.0	A
H0170x_XF	SKS	EQ032960758	27.4	85.0	89	13.5	0.7	0.3	109.3	-23.7	179.8	503.8	A
H0170x_XF	SKS	EQ033060532	27.4	85.0	82	12.5	0.9	0.3	134.0	-45.2	166.5	10.0	A
H0170x_XF	SKS	EQ040510558	27.4	85.0	61	13.0	0.6	0.2	104.2	-11.6	166.5	84.0	A
H0180x_XF	SKKS	EQ032650445	27.5	85.0	80	12.5	1.3	0.5	330.8	19.8	-70.7	10.0	B
H0180x_XF	SKKS	EQ032731408	27.5	85.0	84	14.0	1.2	0.4	114.8	-30.4	-177.4	10.0	A
H0180x_XF	SKS	EQ022951139	27.5	85.0	87	19.0	1.0	0.5	105.7	-20.6	-178.4	549.0	B
H0180x_XF	SKS	EQ032731408	27.5	85.0	76	8.5	1.2	0.2	114.8	-30.4	-177.4	10.0	B
H0180x_XF	SKS	EQ040520234	27.5	85.0	-80	11.0	1.0	0.3	216.0	-58.4	-15.0	10.0	B
H0190x_XF	SKKS	EQ032501319	27.5	85.0	67	18.0	1.0	0.8	111.3	-22.5	172.1	33.0	B
H0190x_XF	SKKS	EQ032731408	27.5	85.0	78	14.0	1.3	0.4	114.8	-30.4	-177.4	10.0	A
H0190x_XF	SKKS	EQ040671108	27.5	85.0	84	14.0	1.4	0.8	117.0	-32.4	-178.2	7.0	B
H0190x_XF	SKS	EQ031292026	27.5	85.0	-87	15.5	1.2	0.5	212.2	-48.2	32.3	10.0	B
H0190x_XF	SKS	EQ033060532	27.5	85.0	77	10.5	1.4	0.3	134.0	-45.2	166.5	10.0	A

Table S1. Well-defined Individual Splitting Parameters. (cont.)

H0190x_XF	SKS	EQ033170249	27.5	85.0	85	5.0	1.2	0.2	149.7	-54.2	143.8	10.0	B
H0190x_XF	SKS	EQ033610455	27.5	85.0	81	15.5	0.9	0.3	112.1	-22.1	169.4	10.0	B
H0190x_XF	SKS	EQ040700348	27.5	85.0	67	14.5	1.1	0.4	116.9	-32.3	-178.1	10.0	B
H0200x_XF	SKS	EQ032160437	27.5	85.0	84	16.5	1.3	0.5	211.5	-60.5	-43.4	10.0	B
H0200x_XF	SKS	EQ032231340	27.5	85.0	83	2.0	1.8	0.2	150.5	-56.9	147.6	10.0	B
H0200x_XF	SKS	EQ033592309	27.5	85.0	69	11.5	1.0	0.2	112.2	-22.3	169.5	10.0	B
H0210x_XF	SKKS	EQ032731408	27.5	85.1	75	15.0	1.4	0.5	114.8	-30.4	-177.4	10.0	A
H0210x_XF	SKKS	EQ033060532	27.5	85.1	86	19.0	1.0	0.7	134.0	-45.2	166.5	10.0	B
H0210x_XF	SKS	EQ030651024	27.5	85.1	69	15.0	0.7	0.3	107.6	-23.6	-175.8	10.0	B
H0210x_XF	SKS	EQ031171603	27.5	85.1	-83	4.5	1.2	0.4	110.9	-20.9	169.8	77.4	B
H0210x_XF	SKS	EQ031292026	27.5	85.1	84	7.5	0.9	0.1	212.2	-48.2	32.3	10.0	A
H0210x_XF	SKS	EQ032160437	27.5	85.1	80	7.0	1.6	0.2	211.6	-60.5	-43.4	10.0	B
H0210x_XF	SKS	EQ032231340	27.5	85.1	86	7.5	1.4	0.3	150.5	-56.9	147.6	10.0	B
H0210x_XF	SKS	EQ032731408	27.5	85.1	87	3.5	1.2	0.2	114.8	-30.4	-177.4	10.0	B
H0210x_XF	SKS	EQ032960758	27.5	85.1	-87	3.0	1.1	0.2	109.3	-23.7	179.8	503.8	B
H0210x_XF	SKS	EQ033060532	27.5	85.1	87	13.0	1.3	0.4	134.0	-45.2	166.5	10.0	A
H0210x_XF	SKS	EQ033170249	27.5	85.1	82	6.5	1.4	0.3	149.7	-54.2	143.8	10.0	B
H0210x_XF	SKS	EQ033592042	27.5	85.1	65	13.5	1.1	0.3	112.2	-22.3	169.5	10.0	B
H0210x_XF	SKS	EQ033611600	27.5	85.1	-88	3.0	1.4	0.2	111.8	-22.0	169.8	10.0	B
H0210x_XF	SKS	EQ033612238	27.5	85.1	-86	5.5	1.5	0.4	111.5	-21.7	169.8	10.0	B
H0220x_XF	SKKS	EQ032650445	27.6	85.1	79	19.5	1.1	0.5	330.9	19.8	-70.7	10.0	A
H0220x_XF	SKS	EQ031292026	27.6	85.1	85	15.5	0.8	0.3	212.2	-48.2	32.3	10.0	A
H0220x_XF	SKS	EQ032160437	27.6	85.1	83	10.0	1.5	0.4	211.6	-60.5	-43.4	10.0	B
H0230x_XF	SKKS	EQ032731408	27.6	85.1	73	14.0	1.6	0.5	114.8	-30.4	-177.4	10.0	A
H0230x_XF	SKS	EQ022801900	27.6	85.1	73	14.5	0.5	0.1	109.1	-18.7	169.3	245.5	B
H0230x_XF	SKS	EQ022951139	27.6	85.1	60	16.0	0.5	0.2	105.7	-20.6	-178.4	549.0	B
H0230x_XF	SKS	EQ030040515	27.6	85.1	56	19.5	0.5	0.4	105.4	-20.6	-177.7	378.0	B
H0230x_XF	SKS	EQ030730255	27.6	85.1	83	6.0	1.6	0.4	151.2	-62.1	161.7	10.0	B
H0230x_XF	SKS	EQ030922131	27.6	85.1	-85	13.5	0.8	0.3	110.6	-25.1	179.9	498.0	B

Table S1. Well-defined Individual Splitting Parameters. (cont.)

H0230x_XF	SKS	EQ031171603	27.6	85.1	-88	11.0	0.9	0.3	110.9	-20.9	169.8	77.4	B
H0230x_XF	SKS	EQ031292026	27.6	85.1	74	14.0	0.7	0.3	212.2	-48.2	32.3	10.0	A
H0230x_XF	SKS	EQ032160437	27.6	85.1	86	19.5	1.4	0.8	211.6	-60.5	-43.4	10.0	B
H0230x_XF	SKS	EQ032331212	27.6	85.1	-87	11.5	1.0	0.2	133.8	-45.1	167.1	28.0	B
H0230x_XF	SKS	EQ032731408	27.6	85.1	73	7.0	0.7	0.1	114.8	-30.4	-177.4	10.0	B
H0230x_XF	SKS	EQ032880219	27.6	85.1	66	19.0	0.6	0.2	103.2	-17.8	-178.7	582.6	B
H0230x_XF	SKS	EQ033060532	27.6	85.1	90	9.0	1.0	0.2	134.0	-45.2	166.5	10.0	B
H0230x_XF	SKS	EQ033612238	27.6	85.1	80	17.0	0.8	0.3	111.5	-21.7	169.8	10.0	B
H0230x_XF	SKS	EQ040110807	27.6	85.1	48	17.5	0.6	0.3	100.7	-16.2	-176.2	366.1	B
H0230x_XF	SKS	EQ040561652	27.6	85.1	63	14.0	0.6	0.2	104.4	-20.7	-175.0	55.8	B
H0240x_XF	SKKS	EQ033090058	27.6	85.1	82	4.5	0.9	0.1	330.4	5.0	-77.8	33.0	B
H0240x_XF	SKS	EQ030160053	27.6	85.1	-79	3.0	1.2	0.3	24.3	44.3	-129.0	10.0	B
H0240x_XF	SKS	EQ030271756	27.6	85.1	81	19.5	0.7	0.3	212.4	-46.0	35.1	10.0	B
H0240x_XF	SKS	EQ031292026	27.6	85.1	73	12.0	0.9	0.2	212.2	-48.2	32.3	10.0	A
H0240x_XF	SKS	EQ033170249	27.6	85.1	-88	7.5	1.0	0.2	149.7	-54.2	143.8	10.0	B
H0250x_XF	SKKS	EQ032650445	27.6	85.1	-88	11.5	0.9	0.3	330.9	19.8	-70.7	10.0	B
H0250x_XF	SKS	EQ030730255	27.6	85.1	89	8.5	1.4	0.3	151.2	-62.1	161.7	10.0	B
H0250x_XF	SKS	EQ032331212	27.6	85.1	81	13.0	0.9	0.2	133.8	-45.1	167.1	28.0	B
H0260x_XF	SKKS	EQ032650445	27.7	85.1	-89	13.0	0.8	0.2	330.9	19.8	-70.7	10.0	A
H0260x_XF	SKKS	EQ032731408	27.7	85.1	76	18.5	1.4	0.6	114.8	-30.4	-177.4	10.0	A
H0260x_XF	SKKS	EQ033090058	27.7	85.1	-77	11.5	0.6	0.1	330.4	5.0	-77.8	33.0	A
H0260x_XF	SKS	EQ030730255	27.7	85.1	-84	4.0	1.4	0.1	151.2	-62.1	161.7	10.0	B
H0260x_XF	SKS	EQ032231340	27.7	85.1	87	16.0	1.0	0.4	150.5	-56.9	147.6	10.0	B
H0260x_XF	SKS	EQ033060532	27.7	85.1	-78	17.5	0.9	0.3	134.0	-45.2	166.5	10.0	A
H0260x_XF	SKS	EQ033170249	27.7	85.1	-77	13.0	0.8	0.2	149.7	-54.2	143.8	10.0	B
H0270x_XF	SKKS	EQ032650445	27.7	85.1	88	14.0	0.9	0.3	330.9	19.8	-70.7	10.0	A
H0270x_XF	SKS	EQ030730255	27.7	85.1	-77	4.0	1.4	0.1	151.2	-62.1	161.7	10.0	B
H0270x_XF	SKS	EQ032331212	27.7	85.1	-84	13.0	1.0	0.2	133.7	-45.1	167.1	28.0	A
H0270x_XF	SKS	EQ033060532	27.7	85.1	86	17.0	0.9	0.5	134.0	-45.2	166.5	10.0	A

Table S1. Well-defined Individual Splitting Parameters. (cont.)

H0280x_XF	SKKS	EQ032731408	27.7	85.1	57	19.5	1.2	0.7	114.7	-30.4	-177.4	10.0	B
H0290x_XF	SKKS	EQ032650445	27.8	85.1	-89	8.5	0.9	0.2	331.0	19.8	-70.7	10.0	B
H0290x_XF	SKKS	EQ033090058	27.8	85.1	-69	12.5	0.7	0.2	330.5	5.0	-77.8	33.0	B
H0290x_XF	SKKS	EQ040351159	27.8	85.1	-78	5.0	0.9	0.1	340.3	8.4	-82.9	29.2	B
H0290x_XF	SKS	EQ033612238	27.8	85.1	-82	8.0	1.4	0.5	111.5	-21.7	169.8	10.0	B
H0310x_XF	SKS	EQ030160053	27.8	85.0	-78	3.0	1.0	0.2	24.2	44.3	-129.0	10.0	B
H0330x_XF	SKKS	EQ032080204	27.9	85.1	62	10.0	0.9	0.2	105.4	-21.1	-176.6	212.9	B
H0330x_XF	SKS	EQ032261823	27.9	85.1	53	17.5	0.5	0.3	104.8	-19.9	-178.0	563.3	B
H0330x_XF	SKS	EQ032731408	27.9	85.1	88	12.5	0.8	0.2	114.7	-30.4	-177.4	10.0	A
H0330x_XF	SKS	EQ033060532	27.9	85.1	82	9.5	1.3	0.3	134.0	-45.2	166.5	10.0	A
H0330x_XF	SKS	EQ033592042	27.9	85.1	71	6.5	1.2	0.1	112.2	-22.3	169.5	10.0	A
H0330x_XF	SKS	EQ040561652	27.9	85.1	76	15.5	0.6	0.2	104.4	-20.7	-175.0	55.8	B
H0360x_XF	SKS	EQ033170249	27.9	85.2	80	3.0	1.5	0.2	149.7	-54.2	143.8	10.0	B
H0370x_XF	SKKS	EQ032731408	28.0	85.2	66	16.5	1.2	0.6	114.7	-30.4	-177.4	10.0	B
H0370x_XF	SKS	EQ022900423	28.0	85.2	36	8.5	1.0	0.2	104.9	-19.8	-178.4	627.6	B
H0370x_XF	SKS	EQ030952203	28.0	85.2	36	6.0	1.0	0.2	107.6	-16.2	167.9	177.5	B
H0370x_XF	SKS	EQ031171603	28.0	85.2	53	14.0	0.6	0.2	110.9	-20.9	169.8	77.4	B
H0370x_XF	SKS	EQ040110929	28.0	85.2	44	14.0	1.2	0.4	105.5	-20.1	-179.2	673.1	B
H0380x_XF	SKS	EQ022900423	28.0	85.2	55	11.0	0.6	0.1	104.9	-19.8	-178.4	627.6	A
H0380x_XF	SKS	EQ030040515	28.0	85.2	41	13.5	0.6	0.2	105.3	-20.6	-177.7	378.0	A
H0380x_XF	SKS	EQ031171603	28.0	85.2	71	13.5	0.5	0.2	110.9	-20.9	169.8	77.4	A
H0380x_XF	SKS	EQ032080204	28.0	85.2	30	8.5	0.8	0.3	105.4	-21.1	-176.6	212.9	B
H0380x_XF	SKS	EQ032261823	28.0	85.2	46	18.0	0.6	0.2	104.8	-19.9	-178.0	563.3	B
H0380x_XF	SKS	EQ032731408	28.0	85.2	58	16.0	0.7	0.2	114.7	-30.4	-177.4	10.0	A
H0380x_XF	SKS	EQ032960758	28.0	85.2	57	19.0	0.5	0.3	109.3	-23.7	179.8	503.8	B
H0380x_XF	SKS	EQ040110929	28.0	85.2	42	9.5	1.0	0.3	105.5	-20.1	-179.2	673.1	B
H0380x_XF	SKS	EQ040251143	28.0	85.2	31	8.5	1.0	0.3	100.4	-16.8	-174.2	129.8	B
H0380x_XF	SKS	EQ040561652	28.0	85.2	50	14.5	0.6	0.2	104.4	-20.7	-175.0	55.8	B
H0390x_XF	SKS	EQ033060532	28.0	85.2	76	17.5	0.9	0.3	134.0	-45.2	166.5	10.0	B

Table S1. Well-defined Individual Splitting Parameters. (cont.)

H0390x_XF	SKS	EQ040561652	28.0	85.2	53	17.5	0.5	0.3	104.4	-20.7	-175.0	55.8	B
H0400x_XF	SKKS	EQ032731408	28.1	85.2	76	11.5	1.2	0.3	114.7	-30.4	-177.4	10.0	A
H0400x_XF	SKKS	EQ033090058	28.1	85.2	78	16.0	1.0	0.5	330.8	5.0	-77.8	33.0	B
H0400x_XF	SKS	EQ032731408	28.1	85.2	81	9.5	0.7	0.2	114.7	-30.4	-177.4	10.0	A
H0400x_XF	SKS	EQ033101038	28.1	85.2	60	13.5	0.7	0.2	109.8	-19.3	168.9	113.7	A
H0410x_XF	SKKS	EQ032731408	28.1	85.3	63	8.5	1.2	0.2	114.7	-30.4	-177.4	10.0	B
H0410x_XF	SKS	EQ023620320	28.1	85.3	48	12.0	0.9	0.2	103.5	-18.2	-178.5	626.6	B
H0410x_XF	SKS	EQ030040515	28.1	85.3	59	13.0	0.6	0.2	105.3	-20.6	-177.7	378.0	A
H0410x_XF	SKS	EQ030952203	28.1	85.3	79	7.5	0.7	0.2	107.6	-16.2	167.9	177.5	A
H0410x_XF	SKS	EQ031171603	28.1	85.3	72	16.5	0.6	0.3	110.9	-20.9	169.8	77.4	B
H0410x_XF	SKS	EQ032731408	28.1	85.3	67	7.0	0.7	0.1	114.7	-30.4	-177.4	10.0	A
H0410x_XF	SKS	EQ040110929	28.1	85.3	63	18.0	0.6	0.3	105.5	-20.1	-179.2	673.1	B
H0410x_XF	SKS	EQ040561652	28.1	85.3	57	17.0	0.7	0.3	104.4	-20.7	-175.0	55.8	B
H0420x_XF	PKS	EQ040351159	28.1	85.3	88	5.0	1.0	0.2	340.8	8.4	-82.9	29.2	B
H0420x_XF	SKS	EQ030040515	28.1	85.3	54	16.0	0.7	0.3	105.3	-20.6	-177.7	378.0	B
H0420x_XF	SKS	EQ031171603	28.1	85.3	63	18.5	0.6	0.3	110.9	-20.9	169.8	77.4	B
H0480x_XF	SKS	EQ041160219	28.3	85.4	82	11.5	1.3	0.4	111.8	-21.8	169.6	10.0	B
H0490x_XF	PKS	EQ033590711	28.3	85.4	-84	15.5	0.8	0.3	340.9	8.4	-82.8	33.0	B
H0490x_XF	PKS	EQ040620347	28.3	85.4	-78	16.5	1.0	0.4	348.0	11.6	-86.8	28.0	A
H0490x_XF	SKS	EQ032231340	28.3	85.4	-88	9.0	1.2	0.3	150.5	-56.9	147.6	10.0	B
H0490x_XF	SKS	EQ032650445	28.3	85.4	89	13.0	1.1	0.3	331.4	19.8	-70.7	10.0	B
H0490x_XF	SKS	EQ040700348	28.3	85.4	58	18.5	1.0	0.4	116.8	-32.3	-178.1	10.0	B
H0490x_XF	SKS	EQ041160219	28.3	85.4	72	5.0	1.5	0.2	111.8	-21.8	169.6	10.0	B
H0500x_XF	PKS	EQ040620347	28.3	85.4	-83	16.0	1.1	0.5	348.0	11.6	-86.8	28.0	A
H0500x_XF	SKS	EQ032231340	28.3	85.4	83	8.0	1.3	0.3	150.5	-56.9	147.6	10.0	B
H0500x_XF	SKS	EQ041280126	28.3	85.4	58	11.5	1.2	0.3	111.7	-22.0	170.3	14.0	B
H0510x_XF	SKKS	EQ033090058	28.4	85.4	82	3.5	2.0	0.3	331.2	5.0	-77.8	33.0	B
H0510x_XF	SKKS	EQ033300742	28.4	85.4	76	5.0	1.2	0.2	322.2	-1.9	-75.7	183.5	B
H0510x_XF	SKS	EQ032880219	28.4	85.4	59	15.5	0.5	0.2	103.2	-17.8	-178.7	582.6	B

Table S1. Well-defined Individual Splitting Parameters. (cont.)

H0510x_XF	SKS	EQ033612238	28.4	85.4	58	15.5	0.9	0.2	111.6	-21.7	169.8	10.0	A
H0520x_XF	PKS	EQ041200057	28.4	85.3	-72	18.5	0.7	0.3	346.6	10.8	-86.0	10.0	B
H0530x_XF	SKS	EQ032231340	28.5	85.2	84	5.0	1.6	0.3	150.4	-56.9	147.6	10.0	B
H0550x_XF	SKKS	EQ032731408	28.5	85.2	89	8.5	1.3	0.3	114.5	-30.4	-177.4	10.0	B
H0560x_XF	SKS	EQ033170249	28.6	85.3	80	18.0	1.1	0.5	149.7	-54.2	143.8	10.0	B
H0570x_XF	SKKS	EQ033090058	28.6	85.3	81	1.5	2.0	0.2	331.2	5.0	-77.8	33.0	B
H0570x_XF	SKS	EQ041612252	28.6	85.3	-77	9.0	1.4	0.2	149.5	-51.6	139.6	10.0	B
H0580x_XF	SKKS	EQ033090058	28.6	85.3	77	3.5	1.5	0.3	331.3	5.0	-77.8	33.0	B
H0580x_XF	SKS	EQ032231340	28.6	85.3	82	14.0	1.0	0.4	150.4	-56.9	147.6	10.0	B
H0580x_XF	SKS	EQ033631148	28.6	85.3	78	11.5	1.0	0.3	112.3	-22.5	169.6	27.1	B
H0590x_XF	SKS	EQ033170249	28.7	85.3	85	19.5	0.9	0.3	149.7	-54.2	143.8	10.0	B
H0590x_XF	SKS	EQ033631148	28.7	85.3	81	5.5	1.5	0.2	112.3	-22.5	169.6	27.1	B
H0600x_XF	SKS	EQ040741630	28.7	85.3	42	19.5	0.9	0.4	99.8	-17.3	-172.3	12.0	B
H0600x_XF	SKS	EQ041071658	28.7	85.3	69	19.0	1.1	0.4	108.2	-24.5	-175.9	10.0	B
H0620x_XF	SKKS	EQ032081141	28.8	85.3	56	11.0	0.8	0.2	281.2	-20.1	-65.2	345.3	B
H0620x_XF	SKKS	EQ040820422	28.8	85.3	51	13.5	0.8	0.3	275.0	-22.9	-64.4	16.0	B
H0620x_XF	SKS	EQ040561652	28.8	85.3	57	18.5	0.6	0.3	104.1	-20.7	-175.0	55.8	B
H0630x_XF	SKKS	EQ031241315	28.8	85.3	63	18.0	1.1	0.6	114.8	-30.5	-178.2	62.4	B
H0630x_XF	SKKS	EQ032081141	28.8	85.3	66	7.0	1.2	0.2	281.2	-20.1	-65.2	345.3	B
H0630x_XF	SKKS	EQ040350518	28.8	85.3	72	4.0	1.1	0.2	268.1	-26.1	-63.5	558.4	A
H0630x_XF	SKS	EQ040692207	28.8	85.3	54	9.0	1.2	0.3	116.7	-32.6	-178.0	10.0	B
H0641x_XF	PKS	EQ043250807	28.9	85.3	85	10.0	0.9	0.3	343.6	9.6	-84.2	16.0	B
H0641x_XF	SKKS	EQ040350518	28.9	85.3	62	10.0	0.8	0.2	268.1	-26.1	-63.5	558.4	B
H0660x_XF	SKKS	EQ032731408	28.9	85.4	54	6.5	1.6	0.3	114.5	-30.4	-177.4	10.0	B
H0660x_XF	SKKS	EQ040350518	28.9	85.4	54	8.0	0.6	0.1	268.3	-26.1	-63.5	558.4	B
H0660x_XF	SKS	EQ031242008	28.9	85.4	55	19.0	1.1	0.5	114.9	-30.6	-178.3	45.6	B
H0670x_XF	SKKS	EQ033090058	28.9	85.4	81	8.0	1.5	0.5	331.7	5.0	-77.8	33.0	B
H0670x_XF	SKS	EQ031292026	28.9	85.4	76	11.0	0.7	0.1	212.4	-48.2	32.3	10.0	A
H0680x_XF	SKKS	EQ032650445	29.0	85.4	81	6.0	1.2	0.3	331.8	19.8	-70.7	10.0	A

Table S1. Well-defined Individual Splitting Parameters. (cont.)

H0680x_XF	SKKS	EQ033090058	29.0	85.4	79	5.5	1.1	0.2	331.7	5.0	-77.8	33.0	B
H0720x_XF	SKS	EQ032080204	29.1	85.4	-82	1.5	1.5	0.4	105.1	-21.1	-176.6	212.9	B
H0780x_XF	SKKS	EQ042411341	29.3	85.2	10	14.0	0.7	0.2	247.9	-35.2	-70.5	5.0	B
H0790x_XF	PKS	EQ043250807	29.4	85.2	86	3.0	1.5	0.3	343.6	9.6	-84.2	16.0	B
H0810x_XF	PKS	EQ043200906	29.5	85.2	-45	11.0	1.3	0.4	331.2	4.7	-77.5	15.0	B
H0810x_XF	SKKS	EQ041810701	29.5	85.2	-42	5.5	1.6	0.2	348.3	10.7	-87.0	9.0	B
H0810x_XF	SKKS	EQ043282104	29.5	85.2	-84	3.5	1.3	0.3	109.8	-24.3	179.0	532.3	B
H0810x_XF	SKKS	EQ050281546	29.5	85.2	-63	6.5	1.0	0.1	332.9	-1.1	-81.2	10.0	A
H0810x_XF	SKKS	EQ051410511	29.5	85.2	-79	12.5	1.1	0.3	330.8	-3.3	-81.0	39.5	A
H1000x_XF	SKKS	EQ043170636	29.3	85.9	57	17.0	0.6	0.2	267.9	-26.7	-63.3	568.7	A
H1010x_XF	PKS	EQ042511153	29.3	85.8	60	9.0	1.1	0.3	264.8	-28.6	-65.8	22.3	B
H1010x_XF	SKKS	EQ041970427	29.3	85.8	-8	20.5	1.1	0.6	102.9	-17.6	-178.6	560.0	A
H1010x_XF	SKKS	EQ043170636	29.3	85.8	69	18.0	1.2	0.5	268.0	-26.7	-63.3	568.7	B
H1010x_XF	SKKS	EQ051531056	29.3	85.8	62	15.5	1.2	0.5	275.5	-24.2	-67.0	196.2	B
H1030x_XF	PKS	EQ050590105	29.5	85.8	67	10.5	0.8	0.2	13.0	18.8	-104.6	10.0	B
H1030x_XF	SKS	EQ043520713	29.5	85.8	-84	2.0	1.7	0.2	107.1	-21.9	-179.3	593.3	B
H1030x_XF	SKS	EQ043591339	29.5	85.8	87	6.5	1.3	0.3	105.4	-20.4	-178.7	614.5	B
H1030x_XF	SKS	EQ050781734	29.5	85.8	-83	8.0	1.3	0.5	107.2	-21.9	-179.5	598.7	B
H1030x_XF	SKS	EQ051401240	29.5	85.8	-84	2.5	1.5	0.2	110.3	-24.5	178.8	565.3	B
H1040x_XF	PKS	EQ043200906	29.6	85.7	85	6.0	1.1	0.3	332.0	4.7	-77.5	15.0	A
H1040x_XF	PKS	EQ043250807	29.6	85.7	84	2.0	1.1	0.2	344.5	9.6	-84.2	16.0	A
H1040x_XF	SKKS	EQ050031759	29.6	85.7	82	6.5	1.3	0.2	140.4	-50.7	161.9	10.0	B
H1050x_XF	PKS	EQ043200906	29.6	85.7	-48	3.0	2.2	0.3	332.0	4.7	-77.5	15.0	B
H1050x_XF	PKS	EQ043250807	29.6	85.7	-36	4.5	1.1	0.2	344.5	9.6	-84.2	16.0	B
H1050x_XF	SKKS	EQ051380910	29.6	85.7	60	4.0	1.6	0.3	219.7	-56.4	-26.9	102.2	B
H1100x_XF	SKKS	EQ043170636	30.0	85.7	19	5.0	1.5	0.3	269.2	-26.7	-63.3	568.7	B
H1100x_XF	SKS	EQ043071002	30.0	85.7	53	15.0	0.9	0.3	21.9	49.3	-128.8	10.0	A
H1110x_XF	SKKS	EQ042411341	30.1	85.6	10	16.0	0.9	0.4	249.6	-35.2	-70.5	5.0	B
H1110x_XF	SKKS	EQ043282104	30.1	85.6	35	4.5	1.2	0.3	109.8	-24.3	179.0	532.3	B

Table S1. Well-defined Individual Splitting Parameters. (cont.)

H1110x_XF	SKS	EQ043222109	30.1	85.6	29	16.5	0.7	0.3	104.9	-20.1	-178.7	622.6	B
H1110x_XF	SKS	EQ051401240	30.1	85.6	32	7.5	0.9	0.3	110.1	-24.5	178.8	565.3	B
H1120x_XF	SKKS	EQ042511153	30.1	85.4	45	16.0	0.7	0.3	266.4	-28.6	-65.8	22.3	B
H1120x_XF	SKKS	EQ043170636	30.1	85.4	58	11.5	0.6	0.2	269.4	-26.7	-63.3	568.7	B
H1140x_XF	SKKS	EQ042411341	30.3	85.3	30	16.5	0.7	0.3	250.2	-35.2	-70.5	5.0	B
H1140x_XF	SKKS	EQ042471904	30.3	85.3	33	10.0	1.3	0.4	97.9	-15.3	-173.3	10.0	B
H1150x_XF	PKS	EQ043250807	30.4	85.3	-6	2.0	1.8	0.3	344.1	9.6	-84.2	16.0	B
H1150x_XF	SKKS	EQ042400043	30.4	85.3	70	11.0	1.3	0.5	272.0	-27.4	-70.8	30.0	B
H1150x_XF	SKS	EQ042472318	30.4	85.3	27	13.5	1.0	0.3	97.7	-15.0	-173.5	10.0	B
H1150x_XF	SKS	EQ042872030	30.4	85.3	75	3.0	2.0	0.2	102.6	-17.6	-178.9	566.3	B
H1150x_XF	SKS	EQ043071002	30.4	85.3	51	12.5	1.3	0.4	21.6	49.3	-128.8	10.0	B
H1150x_XF	SKS	EQ043261107	30.4	85.3	24	4.0	1.4	0.3	98.7	-15.4	-174.9	256.1	B
H1160x_XF	PKS	EQ041810701	30.4	85.3	2	4.5	1.2	0.3	348.6	10.7	-87.0	9.0	A
H1160x_XF	PKS	EQ043250807	30.4	85.3	-1	2.0	1.2	0.2	344.1	9.6	-84.2	16.0	A
H1160x_XF	PKS	EQ043252201	30.4	85.3	5	17.0	0.9	0.4	353.5	13.4	-90.1	40.6	A
H1160x_XF	SKKS	EQ042400043	30.4	85.3	71	5.0	1.6	0.3	272.2	-27.4	-70.8	30.0	B
H1160x_XF	SKKS	EQ042411341	30.4	85.3	38	19.5	0.7	0.3	250.5	-35.2	-70.5	5.0	B
H1160x_XF	SKKS	EQ043170636	30.4	85.3	28	15.0	0.7	0.3	269.9	-26.7	-63.3	568.7	A
H1160x_XF	SKS	EQ041970427	30.4	85.3	30	3.5	1.8	0.3	102.4	-17.6	-178.6	560.0	B
H1160x_XF	SKS	EQ042010801	30.4	85.3	75	11.5	0.7	0.2	20.4	49.6	-127.0	23.7	A
H1160x_XF	SKS	EQ042831544	30.4	85.3	36	19.5	1.2	0.7	97.7	-15.2	-173.3	10.0	A
H1160x_XF	SKS	EQ042872030	30.4	85.3	75	4.0	1.7	0.3	102.5	-17.6	-178.9	566.3	A
H1160x_XF	SKS	EQ043071002	30.4	85.3	69	13.5	1.0	0.3	21.6	49.3	-128.8	10.0	A
H1160x_XF	SKS	EQ043222109	30.4	85.3	29	5.5	1.5	0.4	104.7	-20.1	-178.7	622.6	B
H1160x_XF	SKS	EQ043282104	30.4	85.3	30	3.0	1.5	0.3	109.6	-24.3	179.0	532.3	B
H1160x_XF	SKS	EQ050391448	30.4	85.3	28	3.0	1.6	0.3	106.2	-14.3	167.3	206.3	B
H1160x_XF	SKS	EQ050580454	30.4	85.3	42	10.0	1.0	0.2	102.5	-17.7	-178.6	555.9	B
H1160x_XF	SKS	EQ050781502	30.4	85.3	29	4.5	1.3	0.3	103.1	-20.4	-174.3	18.0	B
H1160x_XF	SKS	EQ050781734	30.4	85.3	28	2.0	1.8	0.3	106.7	-21.9	-179.5	598.7	B

Table S1. Well-defined Individual Splitting Parameters. (cont.)

H1160x_XF	SKS	EQ051011708	30.4	85.3	31	1.5	1.8	0.2	111.2	-22.0	170.6	68.0	B
H1170x_XF	SKKS	EQ041970427	30.5	85.2	30	16.5	1.2	0.7	102.4	-17.6	-178.6	560.0	A
H1170x_XF	SKKS	EQ042010801	30.5	85.2	74	8.5	0.7	0.2	20.4	49.6	-127.0	23.7	B
H1170x_XF	SKS	EQ041970427	30.5	85.2	39	8.0	1.5	0.4	102.4	-17.6	-178.6	560.0	B
H1170x_XF	SKS	EQ043071002	30.5	85.2	72	16.0	0.7	0.3	21.6	49.3	-128.8	10.0	A
H1170x_XF	SKS	EQ043282104	30.5	85.2	37	1.5	1.4	0.1	109.5	-24.3	179.0	532.3	B
H1180x_XF	SKS	EQ041970427	30.6	85.2	46	12.5	1.2	0.4	102.4	-17.6	-178.6	560.0	B
H1180x_XF	SKS	EQ042010801	30.6	85.2	88	6.0	1.2	0.2	20.3	49.6	-127.0	23.7	B
H1180x_XF	SKS	EQ042482024	30.6	85.2	32	8.0	1.4	0.3	97.3	-14.8	-173.2	10.0	A
H1180x_XF	SKS	EQ043222109	30.6	85.2	48	10.5	0.8	0.2	104.6	-20.1	-178.7	622.6	B
H1180x_XF	SKS	EQ043520713	30.6	85.2	44	4.5	1.1	0.2	106.6	-21.9	-179.3	593.3	A
H1180x_XF	SKS	EQ043542013	30.6	85.2	50	14.5	0.8	0.2	102.9	-18.1	-178.9	563.8	B
H1180x_XF	SKS	EQ043550739	30.6	85.2	35	7.5	0.9	0.2	98.9	-15.9	-174.6	227.8	B
H1180x_XF	SKS	EQ043591339	30.6	85.2	43	7.0	1.1	0.2	104.9	-20.4	-178.7	614.5	B
H1190x_XF	SKKS	EQ043282104	30.7	85.1	39	2.5	1.4	0.2	109.5	-24.3	179.0	532.3	A
H1190x_XF	SKS	EQ043222109	30.7	85.1	48	12.0	0.7	0.2	104.6	-20.1	-178.7	622.6	B
H1190x_XF	SKS	EQ043261107	30.7	85.1	34	10.0	0.9	0.2	98.6	-15.4	-174.9	256.1	A
H1190x_XF	SKS	EQ043282104	30.7	85.1	43	2.0	1.0	0.1	109.5	-24.3	179.0	532.3	A
H1190x_XF	SKS	EQ043520713	30.7	85.1	49	5.0	0.9	0.1	106.5	-21.9	-179.3	593.3	B
H1190x_XF	SKS	EQ043591339	30.7	85.1	47	14.0	1.1	0.5	104.8	-20.4	-178.7	614.5	B
H1190x_XF	SKS	EQ050182120	30.7	85.1	41	14.5	1.0	0.4	108.2	-22.9	179.0	588.9	B
H1190x_XF	SKS	EQ050391448	30.7	85.1	33	3.5	1.2	0.2	106.2	-14.3	167.3	206.3	B
H1190x_XF	SKS	EQ051401240	30.7	85.1	45	5.0	1.1	0.2	109.7	-24.5	178.8	565.3	B
H1190x_XF	SKS	EQ052372309	30.7	85.1	43	4.0	1.1	0.2	108.4	-23.7	-180.0	530.7	B
H1200x_XF	SKS	EQ041740904	30.7	85.1	31	2.0	1.4	0.2	103.8	-10.9	166.3	152.8	B
H1200x_XF	SKS	EQ042472318	30.7	85.1	31	9.5	1.3	0.4	97.5	-15.0	-173.5	10.0	B
H1200x_XF	SKS	EQ043222109	30.7	85.1	44	6.0	1.0	0.2	104.6	-20.1	-178.7	622.6	B
H1200x_XF	SKS	EQ043261107	30.7	85.1	39	9.0	0.9	0.2	98.5	-15.4	-174.9	256.1	A
H1200x_XF	SKS	EQ043282104	30.7	85.1	45	6.0	1.2	0.2	109.4	-24.3	179.0	532.3	B

Table S1. Well-defined Individual Splitting Parameters. (cont.)

H1200x_XF	SKS	EQ043520713	30.7	85.1	48	6.0	1.1	0.2	106.5	-21.9	-179.3	593.3	B
H1200x_XF	SKS	EQ043550739	30.7	85.1	29	13.0	0.9	0.3	98.8	-15.9	-174.6	227.8	B
H1200x_XF	SKS	EQ050182120	30.7	85.1	44	5.5	1.0	0.2	108.1	-22.9	179.0	588.9	B
H1200x_XF	SKS	EQ050781734	30.7	85.1	43	5.0	1.1	0.2	106.6	-21.9	-179.5	598.7	A
H1200x_XF	SKS	EQ051401240	30.7	85.1	48	5.5	1.1	0.2	109.7	-24.5	178.8	565.3	B
H1210x_XF	SKKS	EQ042020340	30.8	85.1	48	9.5	0.9	0.2	110.3	-20.3	169.4	37.0	B
H1210x_XF	SKKS	EQ042411341	30.8	85.1	48	10.0	0.8	0.2	251.4	-35.2	-70.5	5.0	B
H1210x_XF	SKKS	EQ043542013	30.8	85.1	29	5.5	1.3	0.3	102.8	-18.1	-178.9	563.8	B
H1210x_XF	SKS	EQ041970427	30.8	85.1	46	13.5	0.7	0.2	102.3	-17.6	-178.6	560.0	A
H1210x_XF	SKS	EQ042521100	30.8	85.1	45	15.0	0.9	0.3	97.6	-15.2	-173.4	12.7	B
H1210x_XF	SKS	EQ043222109	30.8	85.1	54	7.5	0.8	0.1	104.5	-20.1	-178.7	622.6	B
H1210x_XF	SKS	EQ043231227	30.8	85.1	55	16.0	0.8	0.3	105.6	-21.1	-179.1	625.4	B
H1210x_XF	SKS	EQ043261107	30.8	85.1	42	10.0	0.7	0.2	98.5	-15.4	-174.9	256.1	A
H1210x_XF	SKS	EQ043450053	30.8	85.1	46	7.5	1.1	0.3	109.3	-18.9	169.0	137.5	B
H1210x_XF	SKS	EQ043542013	30.8	85.1	46	13.0	0.9	0.3	102.8	-18.1	-178.9	563.8	B
H1210x_XF	SKS	EQ050182120	30.8	85.1	53	10.0	0.8	0.2	108.1	-22.9	179.0	588.9	B
H1210x_XF	SKS	EQ050391448	30.8	85.1	40	3.0	1.1	0.1	106.1	-14.3	167.3	206.3	B
H1210x_XF	SKS	EQ050580454	30.8	85.1	53	10.0	0.8	0.2	102.3	-17.7	-178.6	555.9	B
H1210x_XF	SKS	EQ051341002	30.8	85.1	58	11.5	0.8	0.2	106.0	-22.7	-176.7	119.2	A
H1210x_XF	SKS	EQ051401240	30.8	85.1	55	4.5	0.8	0.1	109.7	-24.5	178.8	565.3	A
H1210x_XF	SKS	EQ051660250	30.8	85.1	75	9.0	1.0	0.2	23.5	41.3	-126.0	16.0	A
H1210x_XF	SKS	EQ052372309	30.8	85.1	58	5.0	0.8	0.1	108.4	-23.7	-180.0	530.7	B
H1220x_XF	PKS	EQ051321115	30.9	85.1	71	10.0	1.1	0.4	144.2	-57.4	-139.2	10.0	B
H1220x_XF	SKKS	EQ043170636	30.9	85.1	67	17.5	0.8	0.4	270.5	-26.7	-63.3	568.7	B
H1220x_XF	SKKS	EQ043282104	30.9	85.1	47	3.5	1.2	0.2	109.4	-24.3	179.0	532.3	A
H1220x_XF	SKS	EQ041740904	30.9	85.1	46	10.0	0.9	0.2	103.8	-10.9	166.3	152.8	B
H1220x_XF	SKS	EQ041970427	30.9	85.1	64	13.5	0.8	0.2	102.2	-17.6	-178.6	560.0	A
H1220x_XF	SKS	EQ042872030	30.9	85.1	66	7.0	1.2	0.2	102.3	-17.6	-178.9	566.3	B
H1220x_XF	SKS	EQ043101731	30.9	85.1	63	10.5	1.0	0.2	109.0	-18.6	169.0	186.7	B

Table S1. Well-defined Individual Splitting Parameters. (cont.)

H1220x_XF	SKS	EQ043222109	30.9	85.1	68	7.5	0.9	0.2	104.5	-20.1	-178.7	622.6	B
H1220x_XF	SKS	EQ043282104	30.9	85.1	68	5.0	0.9	0.1	109.4	-24.3	179.0	532.3	A
H1220x_XF	SKS	EQ051401240	30.9	85.1	72	5.0	1.0	0.1	109.7	-24.5	178.8	565.3	A
H1220x_XF	SKS	EQ051660250	30.9	85.1	74	11.5	1.3	0.3	23.5	41.3	-126.0	16.0	B
H1230x_XF	PKS	EQ051321115	30.9	85.1	84	11.0	1.3	0.3	144.2	-57.4	-139.2	10.0	B
H1230x_XF	SKKS	EQ042020340	30.9	85.1	50	7.5	1.4	0.3	110.3	-20.3	169.4	37.0	B
H1230x_XF	SKKS	EQ043282104	30.9	85.1	55	3.5	1.5	0.2	109.4	-24.3	179.0	532.3	A
H1230x_XF	SKKS	EQ043520713	30.9	85.1	62	12.5	0.8	0.2	106.4	-21.9	-179.3	593.3	B
H1230x_XF	SKKS	EQ050781734	30.9	85.1	51	7.5	1.0	0.2	106.5	-21.9	-179.5	598.7	A
H1230x_XF	SKKS	EQ051922306	30.9	85.1	62	17.0	1.1	0.4	109.9	-27.0	-176.3	10.0	B
H1230x_XF	SKS	EQ041970427	30.9	85.1	67	6.0	1.0	0.2	102.2	-17.6	-178.6	560.0	A
H1230x_XF	SKS	EQ042872030	30.9	85.1	67	5.0	1.5	0.2	102.3	-17.6	-178.9	566.3	B
H1230x_XF	SKS	EQ043071002	30.9	85.1	89	12.0	1.1	0.3	21.5	49.3	-128.8	10.0	B
H1230x_XF	SKS	EQ043101731	30.9	85.1	60	3.5	1.3	0.1	109.0	-18.6	169.0	186.7	B
H1230x_XF	SKS	EQ043180024	30.9	85.1	53	5.5	0.8	0.1	104.1	-10.3	164.7	10.0	B
H1230x_XF	SKS	EQ043261107	30.9	85.1	67	4.5	1.1	0.2	98.5	-15.4	-174.9	256.1	A
H1230x_XF	SKS	EQ043282104	30.9	85.1	68	3.5	1.1	0.1	109.4	-24.3	179.0	532.3	A
H1230x_XF	SKS	EQ043450053	30.9	85.1	72	3.5	1.1	0.1	109.2	-18.9	169.0	137.5	B
H1230x_XF	SKS	EQ043520713	30.9	85.1	72	4.0	1.1	0.1	106.4	-21.9	-179.3	593.3	B
H1230x_XF	SKS	EQ043542013	30.9	85.1	68	6.5	1.1	0.2	102.8	-18.1	-178.9	563.8	B
H1230x_XF	SKS	EQ043550739	30.9	85.1	67	4.5	1.0	0.1	98.8	-15.9	-174.6	227.8	B
H1230x_XF	SKS	EQ043591339	30.9	85.1	66	8.0	0.9	0.2	104.7	-20.4	-178.7	614.5	B
H1230x_XF	SKS	EQ050160825	30.9	85.1	77	5.5	1.2	0.2	108.5	-25.5	-176.3	16.0	A
H1230x_XF	SKS	EQ050182120	30.9	85.1	74	10.5	1.2	0.4	108.1	-22.9	179.0	588.9	B
H1230x_XF	SKS	EQ050391448	30.9	85.1	62	2.5	1.1	0.1	106.1	-14.3	167.3	206.3	B
H1230x_XF	SKS	EQ050580454	30.9	85.1	70	3.0	1.0	0.1	102.3	-17.7	-178.6	555.9	B
H1230x_XF	SKS	EQ050750341	30.9	85.1	73	6.5	1.1	0.2	109.0	-24.4	179.9	507.1	B
H1230x_XF	SKS	EQ050781734	30.9	85.1	68	2.5	1.2	0.1	106.5	-21.9	-179.5	598.7	A
H1230x_XF	SKS	EQ051011708	30.9	85.1	61	6.0	1.1	0.2	111.1	-22.0	170.6	68.0	B

Table S1. Well-defined Individual Splitting Parameters. (cont.)

H1230x_XF	SKS	EQ051042209	30.9	85.1	67	7.5	1.3	0.2	110.9	-22.2	171.4	123.5	B
H1230x_XF	SKS	EQ051341002	30.9	85.1	69	18.0	0.9	0.4	106.0	-22.7	-176.7	119.2	B
H1230x_XF	SKS	EQ052040104	30.9	85.1	67	9.5	1.1	0.2	106.8	-15.2	167.6	125.7	B
H1230x_XF	SKS	EQ052180956	30.9	85.1	62	15.5	1.0	0.3	102.8	-19.6	-175.9	205.4	B
H1230x_XF	SKS	EQ052210526	30.9	85.1	53	14.0	1.1	0.4	108.7	-20.9	173.8	23.6	B
H1230x_XF	SKS	EQ052230908	30.9	85.1	61	5.0	1.3	0.2	112.2	-22.7	169.5	10.0	B
H1230x_XF	SKS	EQ052372309	30.9	85.1	70	2.5	1.1	0.1	108.3	-23.7	-180.0	530.7	B
H1240x_XF	SKKS	EQ043520713	31.0	85.1	54	11.0	0.7	0.2	106.4	-21.9	-179.3	593.3	B
H1240x_XF	SKKS	EQ050781734	31.0	85.1	51	3.5	0.9	0.1	106.5	-21.9	-179.5	598.7	A
H1240x_XF	SKS	EQ041740904	31.0	85.1	66	6.0	1.0	0.2	103.8	-10.9	166.3	152.8	B
H1240x_XF	SKS	EQ041742139	31.0	85.1	73	6.5	1.4	0.3	102.2	-19.1	-175.7	231.0	B
H1240x_XF	SKS	EQ041970427	31.0	85.1	73	7.5	1.1	0.2	102.2	-17.6	-178.6	560.0	A
H1240x_XF	SKS	EQ043101731	31.0	85.1	67	4.0	1.2	0.1	109.0	-18.6	169.0	186.7	B
H1240x_XF	SKS	EQ043450053	31.0	85.1	74	6.5	1.1	0.2	109.2	-18.9	169.0	137.5	B
H1240x_XF	SKS	EQ043520713	31.0	85.1	75	8.0	1.0	0.2	106.4	-21.9	-179.3	593.3	B
H1240x_XF	SKS	EQ043591339	31.0	85.1	72	10.0	0.9	0.2	104.7	-20.4	-178.7	614.5	B
H1240x_XF	SKS	EQ050391448	31.0	85.1	63	2.5	1.0	0.1	106.2	-14.3	167.3	206.3	A
H1240x_XF	SKS	EQ050781734	31.0	85.1	74	2.0	1.0	0.1	106.5	-21.9	-179.5	598.7	A
H1240x_XF	SKS	EQ051401240	31.0	85.1	72	2.5	1.1	0.1	109.6	-24.5	178.8	565.3	B
H1250x_XF	SKKS	EQ041970427	31.1	85.0	61	10.5	1.1	0.2	102.2	-17.6	-178.6	560.0	B
H1250x_XF	SKKS	EQ043520713	31.1	85.0	72	8.0	0.6	0.2	106.3	-21.9	-179.3	593.3	B
H1250x_XF	SKKS	EQ050781734	31.1	85.0	75	16.0	0.6	0.2	106.4	-21.9	-179.5	598.7	A
H1250x_XF	SKKS	EQ051401240	31.1	85.0	72	12.5	0.9	0.3	109.6	-24.5	178.8	565.3	B
H1250x_XF	SKS	EQ041601054	31.1	85.0	75	8.5	0.9	0.2	106.8	-15.2	167.5	115.7	B
H1250x_XF	SKS	EQ041740904	31.1	85.0	74	4.0	0.8	0.1	103.8	-10.9	166.3	152.8	A
H1250x_XF	SKS	EQ041970427	31.1	85.0	87	2.5	1.7	0.3	102.2	-17.6	-178.6	560.0	B
H1250x_XF	SKS	EQ042251559	31.1	85.0	71	7.0	0.7	0.2	104.4	-11.9	166.7	205.7	B
H1250x_XF	SKS	EQ043101731	31.1	85.0	75	7.0	0.9	0.2	108.9	-18.6	169.0	186.7	A
H1250x_XF	SKS	EQ043222109	31.1	85.0	86	11.0	0.9	0.3	104.4	-20.1	-178.7	622.6	B

Table S1. Well-defined Individual Splitting Parameters. (cont.)

H1250x_XF	SKS	EQ043261107	31.1	85.0	83	11.5	1.0	0.4	98.4	-15.4	-174.9	256.1	B
H1250x_XF	SKS	EQ043261141	31.1	85.0	75	4.0	1.7	0.3	320.6	15.7	-61.7	14.0	B
H1250x_XF	SKS	EQ043282104	31.1	85.0	82	4.0	1.0	0.1	109.3	-24.3	179.0	532.3	A
H1250x_XF	SKS	EQ043450053	31.1	85.0	72	4.0	0.9	0.1	109.2	-18.9	169.0	137.5	B
H1250x_XF	SKS	EQ043520713	31.1	85.0	85	5.0	0.9	0.2	106.3	-21.9	-179.3	593.3	B
H1250x_XF	SKS	EQ050182120	31.1	85.0	79	10.0	0.8	0.2	108.0	-22.9	179.0	588.9	B
H1250x_XF	SKS	EQ050391448	31.1	85.0	73	3.0	0.8	0.1	106.1	-14.3	167.3	206.3	A
H1250x_XF	SKS	EQ050580454	31.1	85.0	76	11.5	0.8	0.2	102.2	-17.7	-178.6	555.9	B
H1250x_XF	SKS	EQ050781734	31.1	85.0	85	5.0	1.0	0.2	106.4	-21.9	-179.5	598.7	A
H1250x_XF	SKS	EQ050981138	31.1	85.0	70	9.5	0.9	0.2	112.7	-23.1	169.3	10.0	B
H1250x_XF	SKS	EQ051011708	31.1	85.0	73	8.5	1.0	0.2	111.0	-22.0	170.6	68.0	B
H1250x_XF	SKS	EQ051401240	31.1	85.0	80	4.0	0.9	0.1	109.6	-24.5	178.8	565.3	A
H1250x_XF	SKS	EQ052230908	31.1	85.0	75	5.0	1.0	0.1	112.2	-22.7	169.5	10.0	A
H1260x_XF	SKKS	EQ043282104	31.2	85.0	64	15.5	0.7	0.2	109.3	-24.3	179.0	532.3	B
H1260x_XF	SKKS	EQ051580422	31.2	85.0	73	4.5	1.3	0.2	113.4	-29.5	-179.1	318.3	B
H1260x_XF	SKS	EQ042851814	31.2	85.0	66	14.0	0.9	0.2	108.3	-17.2	167.8	25.0	A
H1260x_XF	SKS	EQ043101731	31.2	85.0	63	12.0	1.1	0.3	108.9	-18.6	169.0	186.7	A
H1260x_XF	SKS	EQ043231227	31.2	85.0	82	4.5	1.3	0.2	105.4	-21.1	-179.1	625.4	B
H1260x_XF	SKS	EQ043282104	31.2	85.0	78	5.0	0.9	0.1	109.3	-24.3	179.0	532.3	A
H1260x_XF	SKS	EQ043450053	31.2	85.0	67	10.0	1.1	0.3	109.2	-18.9	169.0	137.5	B
H1260x_XF	SKS	EQ043520713	31.2	85.0	80	12.5	0.8	0.2	106.3	-21.9	-179.3	593.3	B
H1260x_XF	SKS	EQ050391448	31.2	85.0	73	4.5	0.9	0.1	106.1	-14.3	167.3	206.3	A
H1260x_XF	SKS	EQ050411653	31.2	85.0	59	6.0	1.2	0.2	112.7	-23.1	169.2	9.0	A
H1260x_XF	SKS	EQ050580454	31.2	85.0	81	2.0	1.5	0.2	102.2	-17.7	-178.6	555.9	B
H1260x_XF	SKS	EQ050781734	31.2	85.0	80	4.0	1.0	0.1	106.4	-21.9	-179.5	598.7	B
H1260x_XF	SKS	EQ050981138	31.2	85.0	65	9.0	1.1	0.2	112.7	-23.1	169.3	10.0	B
H1260x_XF	SKS	EQ051011708	31.2	85.0	68	6.0	1.0	0.1	111.0	-22.0	170.6	68.0	B
H1260x_XF	SKS	EQ051042209	31.2	85.0	49	7.0	1.3	0.3	110.8	-22.2	171.4	123.5	B
H1260x_XF	SKS	EQ051401240	31.2	85.0	79	10.5	0.9	0.3	109.6	-24.5	178.8	565.3	B

Table S1. Well-defined Individual Splitting Parameters. (cont.)

H1260x_XF	SKS	EQ052230908	31.2	85.0	69	6.5	1.1	0.2	112.2	-22.7	169.5	10.0	B
H1270x_XF	SKKS	EQ043282104	31.2	85.1	71	13.5	0.6	0.2	109.3	-24.3	179.0	532.3	A
H1270x_XF	SKKS	EQ043520713	31.2	85.1	80	5.5	0.9	0.2	106.3	-21.9	-179.3	593.3	B
H1270x_XF	SKKS	EQ050781734	31.2	85.1	77	9.0	0.8	0.2	106.4	-21.9	-179.5	598.7	A
H1270x_XF	SKKS	EQ051580422	31.2	85.1	63	7.0	0.9	0.2	113.4	-29.5	-179.1	318.3	B
H1270x_XF	SKS	EQ041740904	31.2	85.1	81	7.0	0.7	0.2	103.8	-10.9	166.3	152.8	B
H1270x_XF	SKS	EQ042251559	31.2	85.1	71	8.5	0.8	0.2	104.4	-11.9	166.7	205.7	B
H1270x_XF	SKS	EQ042851814	31.2	85.1	58	3.5	1.0	0.1	108.4	-17.2	167.8	25.0	B
H1270x_XF	SKS	EQ043101731	31.2	85.1	65	8.0	1.0	0.2	108.9	-18.6	169.0	186.7	B
H1270x_XF	SKS	EQ043282104	31.2	85.1	81	3.5	1.0	0.1	109.3	-24.3	179.0	532.3	A
H1270x_XF	SKS	EQ043450053	31.2	85.1	60	13.5	0.8	0.2	109.2	-18.9	169.0	137.5	B
H1270x_XF	SKS	EQ043520713	31.2	85.1	87	14.5	0.8	0.3	106.3	-21.9	-179.3	593.3	B
H1270x_XF	SKS	EQ050182120	31.2	85.1	79	10.5	1.0	0.2	108.0	-22.9	179.0	588.9	B
H1270x_XF	SKS	EQ050391448	31.2	85.1	72	6.0	0.8	0.1	106.1	-14.3	167.3	206.3	A
H1270x_XF	SKS	EQ050781734	31.2	85.1	79	3.0	0.9	0.1	106.4	-21.9	-179.5	598.7	A
H1270x_XF	SKS	EQ050981138	31.2	85.1	69	9.5	0.9	0.2	112.7	-23.1	169.3	10.0	B
H1270x_XF	SKS	EQ051011708	31.2	85.1	72	4.5	1.0	0.1	111.0	-22.0	170.6	68.0	B
H1270x_XF	SKS	EQ051401240	31.2	85.1	80	5.0	0.9	0.1	109.6	-24.5	178.8	565.3	A
H1270x_XF	SKS	EQ052230908	31.2	85.1	78	4.0	1.1	0.1	112.2	-22.7	169.5	10.0	A
H1280x_XF	SKKS	EQ043282104	31.3	85.1	57	14.0	0.9	0.3	109.3	-24.3	179.0	532.3	B
H1280x_XF	SKS	EQ043222109	31.3	85.1	-84	1.5	1.6	0.3	104.4	-20.1	-178.7	622.6	B
H1280x_XF	SKS	EQ043282104	31.3	85.1	85	15.0	0.8	0.3	109.3	-24.3	179.0	532.3	B
H1280x_XF	SKS	EQ050781734	31.3	85.1	-84	1.0	1.5	0.2	106.4	-21.9	-179.5	598.7	A
H1280x_XF	SKS	EQ050981138	31.3	85.1	-81	1.5	1.6	0.2	112.7	-23.1	169.3	10.0	B
H1280x_XF	SKS	EQ051042209	31.3	85.1	81	14.5	1.1	0.5	110.9	-22.2	171.4	123.5	B
H1280x_XF	SKS	EQ052180956	31.3	85.1	-85	2.0	1.5	0.3	102.7	-19.6	-175.9	205.4	B
H1290x_XF	SKKS	EQ041970427	31.4	85.1	26	5.0	1.5	0.5	102.1	-17.6	-178.6	560.0	A
H1290x_XF	SKS	EQ041740904	31.4	85.1	52	16.5	0.6	0.2	103.8	-10.9	166.3	152.8	B
H1300x_XF	SKKS	EQ041970427	31.5	85.2	73	13.0	0.8	0.3	102.1	-17.6	-178.6	560.0	A

Table S1. Well-defined Individual Splitting Parameters. (cont.)

H1300x_XF	SKKS	EQ042020340	31.5	85.2	53	15.5	0.9	0.3	110.2	-20.3	169.4	37.0	B
H1300x_XF	SKKS	EQ042552152	31.5	85.2	72	17.5	0.6	0.3	218.6	-58.0	-25.3	63.9	A
H1300x_XF	SKKS	EQ043282104	31.5	85.2	68	10.5	1.0	0.3	109.3	-24.3	179.0	532.3	A
H1300x_XF	SKS	EQ041740904	31.5	85.2	82	4.5	0.8	0.1	103.9	-10.9	166.3	152.8	A
H1300x_XF	SKS	EQ041970427	31.5	85.2	82	8.5	1.3	0.5	102.1	-17.6	-178.6	560.0	B
H1300x_XF	SKS	EQ043261107	31.5	85.2	83	6.5	1.1	0.3	98.3	-15.4	-174.9	256.1	B
H1300x_XF	SKS	EQ043282104	31.5	85.2	80	4.0	1.1	0.1	109.3	-24.3	179.0	532.3	A
H1300x_XF	SKS	EQ043520713	31.5	85.2	82	4.5	0.9	0.2	106.3	-21.9	-179.3	593.3	A
H1300x_XF	SKS	EQ050182120	31.5	85.2	83	5.0	1.1	0.2	108.0	-22.9	179.0	588.9	B
H1300x_XF	SKS	EQ050391448	31.5	85.2	69	8.0	0.7	0.2	106.2	-14.3	167.3	206.3	A
H1300x_XF	SKS	EQ050411653	31.5	85.2	77	14.5	0.9	0.3	112.7	-23.1	169.2	9.0	B
H1300x_XF	SKS	EQ050781734	31.5	85.2	84	3.0	1.1	0.1	106.4	-21.9	-179.5	598.7	A
H1300x_XF	SKS	EQ050981138	31.5	85.2	71	10.0	1.1	0.2	112.7	-23.1	169.3	10.0	B
H1310x_XF	PKS	EQ051321115	31.5	85.2	80	8.0	1.0	0.3	143.7	-57.4	-139.2	10.0	B
H1310x_XF	SKKS	EQ041970427	31.5	85.2	71	15.0	0.6	0.3	102.1	-17.6	-178.6	560.0	B
H1310x_XF	SKKS	EQ042552152	31.5	85.2	79	19.0	0.6	0.3	218.6	-58.0	-25.3	63.9	B
H1310x_XF	SKKS	EQ043282104	31.5	85.2	68	16.0	0.8	0.3	109.2	-24.3	179.0	532.3	A
H1310x_XF	SKKS	EQ050781734	31.5	85.2	75	12.5	0.8	0.2	106.4	-21.9	-179.5	598.7	A
H1310x_XF	SKS	EQ041740904	31.5	85.2	63	10.5	0.7	0.2	103.9	-10.9	166.3	152.8	B
H1310x_XF	SKS	EQ042721529	31.5	85.2	60	10.5	0.6	0.1	211.2	-52.5	28.0	10.0	A
H1310x_XF	SKS	EQ043101731	31.5	85.2	53	7.5	0.8	0.1	109.0	-18.6	169.0	186.7	A
H1310x_XF	SKS	EQ043231227	31.5	85.2	75	6.5	1.2	0.2	105.4	-21.1	-179.1	625.4	B
H1310x_XF	SKS	EQ043261107	31.5	85.2	72	19.5	0.6	0.3	98.3	-15.4	-174.9	256.1	B
H1310x_XF	SKS	EQ043282104	31.5	85.2	75	9.5	0.9	0.2	109.2	-24.3	179.0	532.3	A
H1310x_XF	SKS	EQ043520713	31.5	85.2	76	7.5	0.8	0.2	106.3	-21.9	-179.3	593.3	A
H1310x_XF	SKS	EQ043591339	31.5	85.2	76	14.5	0.7	0.2	104.6	-20.4	-178.7	614.5	B
H1310x_XF	SKS	EQ050182120	31.5	85.2	73	15.0	0.8	0.3	108.0	-22.9	179.0	588.9	B
H1310x_XF	SKS	EQ050391448	31.5	85.2	64	5.5	0.7	0.1	106.2	-14.3	167.3	206.3	B
H1310x_XF	SKS	EQ050781734	31.5	85.2	73	10.0	0.8	0.2	106.4	-21.9	-179.5	598.7	A

Table S1. Well-defined Individual Splitting Parameters. (cont.)

H1310x_XF	SKS	EQ050981138	31.5	85.2	67	14.0	1.0	0.3	112.7	-23.1	169.3	10.0	B
H1310x_XF	SKS	EQ051011708	31.5	85.2	58	3.0	0.9	0.1	111.1	-22.0	170.6	68.0	A
H1310x_XF	SKS	EQ051042209	31.5	85.2	64	8.5	0.8	0.2	110.9	-22.2	171.4	123.5	B
H1310x_XF	SKS	EQ052180956	31.5	85.2	69	5.0	0.9	0.1	102.6	-19.6	-175.9	205.4	B
H1310x_XF	SKS	EQ052230908	31.5	85.2	61	14.0	0.7	0.2	112.2	-22.7	169.5	10.0	A
H1320x_XF	SKKS	EQ043542013	31.6	85.2	38	11.5	0.7	0.2	102.6	-18.1	-178.9	563.8	B
H1320x_XF	SKKS	EQ050781734	31.6	85.2	60	19.0	0.5	0.4	106.4	-21.9	-179.5	598.7	B
H1320x_XF	SKS	EQ042251559	31.6	85.2	51	14.5	0.6	0.2	104.5	-11.9	166.7	205.7	B
H1320x_XF	SKS	EQ043101731	31.6	85.2	59	11.5	0.7	0.1	109.0	-18.6	169.0	186.7	A
H1320x_XF	SKS	EQ043222109	31.6	85.2	54	14.0	0.6	0.2	104.4	-20.1	-178.7	622.6	A
H1320x_XF	SKS	EQ043231227	31.6	85.2	70	15.0	0.7	0.2	105.4	-21.1	-179.1	625.4	B
H1320x_XF	SKS	EQ043282104	31.6	85.2	70	7.0	0.7	0.1	109.2	-24.3	179.0	532.3	A
H1320x_XF	SKS	EQ043450053	31.6	85.2	61	9.5	0.7	0.2	109.2	-18.9	169.0	137.5	B
H1320x_XF	SKS	EQ043520713	31.6	85.2	58	9.0	0.5	0.1	106.3	-21.9	-179.3	593.3	B
H1320x_XF	SKS	EQ043542013	31.6	85.2	62	5.5	0.7	0.1	102.6	-18.1	-178.9	563.8	A
H1320x_XF	SKS	EQ050182120	31.6	85.2	63	5.5	0.8	0.1	108.0	-22.9	179.0	588.9	B
H1320x_XF	SKS	EQ050221127	31.6	85.2	66	7.0	1.0	0.2	114.8	-31.6	-177.9	23.5	B
H1320x_XF	SKS	EQ050391448	31.6	85.2	53	8.0	0.7	0.1	106.2	-14.3	167.3	206.3	A
H1320x_XF	SKS	EQ050580454	31.6	85.2	57	12.5	0.8	0.2	102.2	-17.7	-178.6	555.9	B
H1320x_XF	SKS	EQ050781734	31.6	85.2	66	7.5	0.6	0.1	106.4	-21.9	-179.5	598.7	A
H1320x_XF	SKS	EQ051011708	31.6	85.2	63	6.5	0.8	0.1	111.1	-22.0	170.6	68.0	B
H1320x_XF	SKS	EQ051341002	31.6	85.2	53	12.0	0.6	0.1	105.8	-22.7	-176.7	119.2	A
H1330x_XF	SKKS	EQ042552152	31.7	85.2	-65	9.5	0.7	0.3	218.7	-58.0	-25.3	63.9	A
H1330x_XF	SKKS	EQ043170636	31.7	85.2	60	13.0	0.5	0.1	272.1	-26.7	-63.3	568.7	A
H1330x_XF	SKKS	EQ043381459	31.7	85.2	85	17.5	1.0	0.5	118.6	-34.4	179.3	157.4	B
H1330x_XF	SKKS	EQ050391448	31.7	85.2	80	8.0	0.6	0.2	106.2	-14.3	167.3	206.3	B
H1330x_XF	SKS	EQ041601054	31.7	85.2	69	11.0	0.7	0.2	106.9	-15.2	167.5	115.7	B
H1330x_XF	SKS	EQ041740904	31.7	85.2	90	7.0	1.1	0.4	103.9	-10.9	166.3	152.8	B
H1330x_XF	SKS	EQ043101731	31.7	85.2	85	18.0	0.9	0.4	108.9	-18.6	169.0	186.7	B

Table S1. Well-defined Individual Splitting Parameters. (cont.)

H1330x_XF	SKS	EQ043222109	31.7	85.2	85	11.5	1.0	0.3	104.3	-20.1	-178.7	622.6	B
H1330x_XF	SKS	EQ043282104	31.7	85.2	85	3.0	0.9	0.1	109.2	-24.3	179.0	532.3	A
H1330x_XF	SKS	EQ043450053	31.7	85.2	78	11.0	1.0	0.3	109.2	-18.9	169.0	137.5	B
H1330x_XF	SKS	EQ043520713	31.7	85.2	84	2.5	1.0	0.1	106.3	-21.9	-179.3	593.3	A
H1330x_XF	SKS	EQ043542013	31.7	85.2	78	7.0	0.8	0.2	102.6	-18.1	-178.9	563.8	B
H1330x_XF	SKS	EQ043591339	31.7	85.2	84	6.5	0.9	0.2	104.6	-20.4	-178.7	614.5	B
H1330x_XF	SKS	EQ050182120	31.7	85.2	84	4.0	0.9	0.2	107.9	-22.9	179.0	588.9	A
H1330x_XF	SKS	EQ050391448	31.7	85.2	81	5.5	0.7	0.2	106.2	-14.3	167.3	206.3	A
H1330x_XF	SKS	EQ050580454	31.7	85.2	81	10.0	1.1	0.4	102.1	-17.7	-178.6	555.9	B
H1330x_XF	SKS	EQ050781734	31.7	85.2	86	2.5	1.0	0.1	106.4	-21.9	-179.5	598.7	A
H1340x_XF	SKKS	EQ042020340	31.7	85.1	72	10.5	0.9	0.2	110.2	-20.3	169.4	37.0	B
H1340x_XF	SKKS	EQ043282104	31.7	85.1	86	7.0	1.3	0.3	109.2	-24.3	179.0	532.3	A
H1340x_XF	SKKS	EQ051401240	31.7	85.1	85	6.5	1.4	0.3	109.5	-24.5	178.8	565.3	B
H1340x_XF	SKS	EQ041740904	31.7	85.1	85	11.5	1.1	0.3	103.9	-10.9	166.3	152.8	B
H1340x_XF	SKS	EQ043231227	31.7	85.1	-89	5.5	1.4	0.4	105.4	-21.1	-179.1	625.4	B
H1340x_XF	SKS	EQ043261107	31.7	85.1	87	3.5	1.7	0.5	98.3	-15.4	-174.9	256.1	B
H1340x_XF	SKS	EQ043282104	31.7	85.1	88	5.5	1.2	0.3	109.2	-24.3	179.0	532.3	B
H1340x_XF	SKS	EQ043450053	31.7	85.1	77	8.5	1.0	0.2	109.2	-18.9	169.0	137.5	B
H1340x_XF	SKS	EQ050391448	31.7	85.1	83	2.5	1.1	0.1	106.2	-14.3	167.3	206.3	B
H1340x_XF	SKS	EQ050411653	31.7	85.1	75	13.5	1.0	0.3	112.7	-23.1	169.2	9.0	B
H1340x_XF	SKS	EQ050580454	31.7	85.1	86	7.5	1.2	0.4	102.1	-17.7	-178.6	555.9	B
H1340x_XF	SKS	EQ050781734	31.7	85.1	89	3.0	1.4	0.2	106.3	-21.9	-179.5	598.7	B
H1340x_XF	SKS	EQ051011708	31.7	85.1	82	5.5	1.1	0.2	111.0	-22.0	170.6	68.0	A
H1340x_XF	SKS	EQ051341002	31.7	85.1	88	4.5	1.2	0.2	105.8	-22.7	-176.7	119.2	B
H1340x_XF	SKS	EQ051401240	31.7	85.1	-88	5.0	1.2	0.3	109.5	-24.5	178.8	565.3	B
H1340x_XF	SKS	EQ052210526	31.7	85.1	69	18.0	0.7	0.3	108.6	-20.9	173.8	23.6	B
H1340x_XF	SKS	EQ052230908	31.7	85.1	77	9.0	0.9	0.2	112.2	-22.7	169.5	10.0	B
H1350x_XF	SKS	EQ043101731	31.8	85.0	72	13.0	0.7	0.2	108.9	-18.6	169.0	186.7	B
H1350x_XF	SKS	EQ043282104	31.8	85.0	89	8.5	0.7	0.2	109.1	-24.3	179.0	532.3	A

Table S1. Well-defined Individual Splitting Parameters. (cont.)

H1350x_XF	SKS	EQ043450053	31.8	85.0	76	16.0	0.7	0.3	109.1	-18.9	169.0	137.5	B
H1350x_XF	SKS	EQ043520713	31.8	85.0	89	12.5	0.7	0.3	106.2	-21.9	-179.3	593.3	B
H1350x_XF	SKS	EQ050391448	31.8	85.0	88	4.0	1.0	0.2	106.1	-14.3	167.3	206.3	A
H1350x_XF	SKS	EQ051341002	31.8	85.0	89	17.5	1.1	0.6	105.7	-22.7	-176.7	119.2	B
H1350x_XF	SKS	EQ052230908	31.8	85.0	76	4.5	1.0	0.1	112.1	-22.7	169.5	10.0	B
H1360x_XF	SKS	EQ043231227	31.9	85.0	85	9.0	1.0	0.3	105.2	-21.1	-179.1	625.4	B
H1360x_XF	SKS	EQ043282104	31.9	85.0	-89	2.0	1.2	0.2	109.1	-24.3	179.0	532.3	A
H1360x_XF	SKS	EQ043450053	31.9	85.0	82	11.5	1.0	0.3	109.1	-18.9	169.0	137.5	B
H1360x_XF	SKS	EQ043520713	31.9	85.0	-88	2.0	1.4	0.2	106.1	-21.9	-179.3	593.3	B
H1360x_XF	SKS	EQ050391448	31.9	85.0	88	2.5	1.3	0.2	106.0	-14.3	167.3	206.3	B
H1360x_XF	SKS	EQ050781734	31.9	85.0	-89	2.0	1.6	0.2	106.2	-21.9	-179.5	598.7	B
H1360x_XF	SKS	EQ050981138	31.9	85.0	75	14.5	1.0	0.3	112.6	-23.1	169.3	10.0	B
H1360x_XF	SKS	EQ051011708	31.9	85.0	84	4.0	1.1	0.1	110.9	-22.0	170.6	68.0	A
H1360x_XF	SKS	EQ051401240	31.9	85.0	89	4.5	1.2	0.2	109.3	-24.5	178.8	565.3	B
H1370x_XF	SKKS	EQ042552152	32.0	84.9	-66	3.5	1.4	0.3	218.8	-58.0	-25.3	63.9	B
H1370x_XF	SKKS	EQ050781734	32.0	84.9	87	5.0	1.1	0.2	106.2	-21.9	-179.5	598.7	A
H1370x_XF	SKS	EQ043101731	32.0	84.9	67	8.5	1.2	0.2	108.8	-18.6	169.0	186.7	A
H1370x_XF	SKS	EQ043231227	32.0	84.9	-89	3.0	1.7	0.3	105.2	-21.1	-179.1	625.4	B
H1370x_XF	SKS	EQ043282104	32.0	84.9	-87	3.5	1.4	0.3	109.0	-24.3	179.0	532.3	B
H1370x_XF	SKS	EQ043450053	32.0	84.9	81	7.0	1.5	0.4	109.1	-18.9	169.0	137.5	B
H1370x_XF	SKS	EQ043520713	32.0	84.9	82	4.5	1.3	0.3	106.1	-21.9	-179.3	593.3	B
H1370x_XF	SKS	EQ043550739	32.0	84.9	89	7.0	1.6	0.8	98.4	-15.9	-174.6	227.8	B
H1370x_XF	SKS	EQ043591339	32.0	84.9	83	8.0	1.0	0.3	104.4	-20.4	-178.7	614.5	B
H1370x_XF	SKS	EQ050411653	32.0	84.9	-85	6.5	1.5	0.4	112.5	-23.1	169.2	9.0	B
H1370x_XF	SKS	EQ050781734	32.0	84.9	89	3.0	1.4	0.3	106.2	-21.9	-179.5	598.7	B
H1370x_XF	SKS	EQ051011708	32.0	84.9	87	6.0	1.1	0.2	110.9	-22.0	170.6	68.0	A
H1380x_XF	SKS	EQ043282104	32.0	84.8	90	2.5	1.3	0.2	109.0	-24.3	179.0	532.3	B
H1380x_XF	SKS	EQ043450053	32.0	84.8	79	9.0	1.3	0.3	109.0	-18.9	169.0	137.5	B
H1380x_XF	SKS	EQ043520713	32.0	84.8	86	2.0	1.2	0.1	106.0	-21.9	-179.3	593.3	A

Table S1. Well-defined Individual Splitting Parameters. (cont.)

H1380x_XF	SKS	EQ043591339	32.0	84.8	86	6.0	1.1	0.3	104.3	-20.4	-178.7	614.5	B
H1380x_XF	SKS	EQ050391448	32.0	84.8	86	7.0	1.4	0.4	106.0	-14.3	167.3	206.3	B
H1380x_XF	SKS	EQ051401240	32.0	84.8	87	2.5	1.2	0.1	109.2	-24.5	178.8	565.3	B
H1380x_XF	SKS	EQ052040104	32.0	84.8	81	8.0	1.1	0.3	106.6	-15.2	167.6	125.7	B
H1380x_XF	SKS	EQ052210526	32.0	84.8	89	8.0	1.4	0.4	108.4	-20.9	173.8	23.6	B
H1380x_XF	SKS	EQ052230908	32.0	84.8	77	7.5	1.1	0.2	112.0	-22.7	169.5	10.0	B
H1390x_XF	SKS	EQ041740904	32.1	84.9	82	7.5	1.5	0.4	103.8	-10.9	166.3	152.8	B
H1400x_XF	SKKS	EQ043282104	32.1	84.7	-84	3.5	1.6	0.4	108.9	-24.3	179.0	532.3	B
H1400x_XF	SKKS	EQ051580422	32.1	84.7	88	11.5	0.8	0.3	112.9	-29.5	-179.1	318.3	B
H1400x_XF	SKS	EQ043101731	32.1	84.7	-87	6.5	1.3	0.4	108.7	-18.6	169.0	186.7	B
H1400x_XF	SKS	EQ043180024	32.1	84.7	87	9.5	1.3	0.4	104.0	-10.3	164.7	10.0	B
H1400x_XF	SKS	EQ043282104	32.1	84.7	-81	1.5	1.6	0.2	108.9	-24.3	179.0	532.3	B
H1400x_XF	SKS	EQ050391448	32.1	84.7	-87	4.0	1.2	0.3	105.9	-14.3	167.3	206.3	B
H1400x_XF	SKS	EQ050411653	32.1	84.7	-86	11.0	1.0	0.3	112.4	-23.1	169.2	9.0	B
H1400x_XF	SKS	EQ051011708	32.1	84.7	-87	5.0	1.3	0.3	110.7	-22.0	170.6	68.0	B
H1405x_XF	PKS	EQ041810701	32.2	84.5	30	18.5	0.4	0.2	347.9	10.7	-87.0	9.0	A
H1405x_XF	SKKS	EQ042411341	32.2	84.5	31	10.5	0.9	0.2	255.0	-35.2	-70.5	5.0	B
H1410x_XF	SKKS	EQ042010801	32.2	84.4	72	18.5	1.1	0.4	19.8	49.6	-127.0	23.7	B
H1410x_XF	SKKS	EQ050801223	32.2	84.4	23	11.0	1.6	0.8	276.1	-25.0	-63.5	579.1	B
H1410x_XF	SKKS	EQ050801243	32.2	84.4	28	2.5	1.8	0.2	276.7	-24.7	-63.5	570.1	B
H1410x_XF	SKS	EQ043261107	32.2	84.4	33	10.0	1.0	0.3	97.7	-15.4	-174.9	256.1	B
H1410x_XF	SKS	EQ043450053	32.2	84.4	71	18.5	0.6	0.3	108.8	-18.9	169.0	137.5	B
H1410x_XF	SKS	EQ043520713	32.2	84.4	63	13.5	0.6	0.2	105.7	-21.9	-179.3	593.3	A
H1410x_XF	SKS	EQ050182120	32.2	84.4	56	19.5	0.7	0.4	107.4	-22.9	179.0	588.9	B
H1410x_XF	SKS	EQ050781734	32.2	84.4	55	17.0	0.6	0.2	105.8	-21.9	-179.5	598.7	A
H1410x_XF	SKS	EQ050981138	32.2	84.4	35	6.5	1.5	0.5	112.2	-23.1	169.3	10.0	B
H1410x_XF	SKS	EQ051011708	32.2	84.4	75	15.0	0.6	0.2	110.6	-22.0	170.6	68.0	B
H1410x_XF	SKS	EQ051401240	32.2	84.4	68	8.5	0.6	0.1	109.0	-24.5	178.8	565.3	A
H1415x_XF	PKS	EQ041810701	32.3	84.2	62	5.0	1.3	0.3	347.5	10.7	-87.0	9.0	B

Table S1. Well-defined Individual Splitting Parameters. (cont.)

H1415x_XF	SKKS	EQ042010801	32.3	84.2	85	5.5	1.6	0.3	19.7	49.6	-127.0	23.7	B
H1415x_XF	SKS	EQ042721529	32.3	84.2	49	9.5	1.1	0.4	210.8	-52.5	28.0	10.0	B
H1415x_XF	SKS	EQ043071002	32.3	84.2	72	6.0	1.9	0.3	20.9	49.3	-128.8	10.0	B
H1420x_XF	PKS	EQ041810701	31.9	83.8	17	6.0	0.7	0.1	346.9	10.7	-87.0	9.0	A
H1420x_XF	SKS	EQ042721529	31.9	83.8	-17	14.0	0.5	0.2	210.6	-52.5	28.0	10.0	B
H1421x_XF	PKS	EQ041810701	32.0	83.9	26	15.0	0.6	0.2	346.9	10.7	-87.0	9.0	A
H1421x_XF	PKS	EQ042310903	32.0	83.9	36	18.5	0.7	0.2	358.5	16.4	-94.9	62.9	B
H1421x_XF	PKS	EQ043250807	32.0	83.9	17	12.5	0.6	0.1	342.5	9.6	-84.2	16.0	A
H1422x_XF	PKS	EQ041662254	32.1	83.9	57	14.5	0.7	0.2	2.3	16.3	-97.8	10.0	B
H1422x_XF	PKS	EQ041810701	32.1	83.9	61	5.0	1.0	0.2	347.0	10.7	-87.0	9.0	A
H1422x_XF	SKKS	EQ051062241	32.1	83.9	52	15.5	0.8	0.3	294.7	-17.6	-69.7	118.7	B
H1422x_XF	SKS	EQ042552152	32.1	83.9	63	9.5	0.9	0.2	218.8	-58.0	-25.3	63.9	B
H1422x_XF	SKS	EQ050580454	32.1	83.9	29	18.0	0.8	0.3	101.4	-17.7	-178.6	555.9	B
H1423x_XF	SKKS	EQ041810701	32.2	83.9	1	13.5	1.7	0.6	347.1	10.7	-87.0	9.0	B
H1423x_XF	SKS	EQ042851814	32.2	83.9	38	9.0	0.8	0.3	107.7	-17.2	167.8	25.0	B
H1423x_XF	SKS	EQ043101731	32.2	83.9	71	13.0	0.5	0.1	108.3	-18.6	169.0	186.7	B
H1425x_XF	PKS	EQ043250807	32.3	84.1	-65	12.0	0.5	0.1	342.9	9.6	-84.2	16.0	A
H1430x_XF	SKKS	EQ042411341	32.4	84.1	32	12.0	0.8	0.2	255.5	-35.2	-70.5	5.0	B
H1430x_XF	SKKS	EQ042511153	32.4	84.1	44	8.0	1.4	0.3	270.4	-28.6	-65.8	22.3	A
H1430x_XF	SKKS	EQ042552152	32.4	84.1	65	8.0	1.1	0.2	219.0	-58.0	-25.3	63.9	A
H1430x_XF	SKKS	EQ050781734	32.4	84.1	54	10.0	0.8	0.2	105.7	-21.9	-179.5	598.7	A
H1430x_XF	SKKS	EQ050900146	32.4	84.1	53	18.5	1.2	0.6	104.8	-18.4	176.0	10.0	B
H1430x_XF	SKKS	EQ051401240	32.4	84.1	65	17.0	1.1	0.4	108.8	-24.5	178.8	565.3	B
H1430x_XF	SKKS	EQ052260239	32.4	84.1	47	7.0	1.0	0.2	290.9	-19.8	-69.0	113.8	B
H1430x_XF	SKS	EQ042721529	32.4	84.1	51	3.5	1.3	0.2	210.8	-52.5	28.0	10.0	B
H1430x_XF	SKS	EQ043101731	32.4	84.1	55	8.5	1.2	0.2	108.4	-18.6	169.0	186.7	B
H1430x_XF	SKS	EQ043450053	32.4	84.1	58	5.5	1.2	0.2	108.6	-18.9	169.0	137.5	B
H1430x_XF	SKS	EQ043520713	32.4	84.1	52	8.0	1.1	0.2	105.6	-21.9	-179.3	593.3	B
H1430x_XF	SKS	EQ043542013	32.4	84.1	51	9.5	1.2	0.3	101.9	-18.1	-178.9	563.8	B

Table S1. Well-defined Individual Splitting Parameters. (cont.)

H1430x_XF	SKS	EQ050391448	32.4	84.1	53	3.5	1.2	0.1	105.6	-14.3	167.3	206.3	B
H1430x_XF	SKS	EQ050781734	32.4	84.1	52	8.5	1.4	0.3	105.7	-21.9	-179.5	598.7	B
H1430x_XF	SKS	EQ050981138	32.4	84.1	51	4.5	1.2	0.2	112.1	-23.1	169.3	10.0	B
H1430x_XF	SKS	EQ051011708	32.4	84.1	50	4.5	1.3	0.2	110.4	-22.0	170.6	68.0	B
H1430x_XF	SKS	EQ051401240	32.4	84.1	55	3.5	1.4	0.1	108.8	-24.5	178.8	565.3	B
H1430x_XF	SKS	EQ052180956	32.4	84.1	45	6.0	1.6	0.3	101.9	-19.6	-175.9	205.4	B
H1430x_XF	SKS	EQ052230908	32.4	84.1	49	8.0	1.1	0.3	111.6	-22.7	169.5	10.0	A
H1440x_XF	SKKS	EQ042010801	32.5	84.2	86	5.5	1.5	0.3	19.7	49.6	-127.0	23.7	B
H1440x_XF	SKKS	EQ051401240	32.5	84.2	57	10.5	1.4	0.3	108.9	-24.5	178.8	565.3	B
H1440x_XF	SKKS	EQ051531056	32.5	84.2	58	11.5	1.0	0.3	280.6	-24.2	-67.0	196.2	B
H1440x_XF	SKKS	EQ052260239	32.5	84.2	70	9.5	1.1	0.2	291.2	-19.8	-69.0	113.8	B
H1440x_XF	SKS	EQ041740904	32.5	84.2	74	18.5	0.7	0.3	103.4	-10.9	166.3	152.8	B
H1440x_XF	SKS	EQ043450053	32.5	84.2	68	3.0	1.3	0.1	108.7	-18.9	169.0	137.5	B
H1440x_XF	SKS	EQ043520713	32.5	84.2	64	7.5	1.3	0.3	105.6	-21.9	-179.3	593.3	B
H1440x_XF	SKS	EQ050391448	32.5	84.2	74	3.0	1.3	0.1	105.7	-14.3	167.3	206.3	B
H1440x_XF	SKS	EQ050411653	32.5	84.2	61	10.5	1.1	0.2	112.1	-23.1	169.2	9.0	A
H1440x_XF	SKS	EQ050781734	32.5	84.2	61	3.0	1.2	0.1	105.7	-21.9	-179.5	598.7	A
H1440x_XF	SKS	EQ050981138	32.5	84.2	56	4.0	1.4	0.2	112.1	-23.1	169.3	10.0	B
H1440x_XF	SKS	EQ051011708	32.5	84.2	66	6.0	1.1	0.1	110.5	-22.0	170.6	68.0	B
H1440x_XF	SKS	EQ051401240	32.5	84.2	70	5.0	1.2	0.2	108.9	-24.5	178.8	565.3	B
H1440x_XF	SKS	EQ052230908	32.5	84.2	60	7.0	1.2	0.2	111.6	-22.7	169.5	10.0	B
H1450x_XF	SKKS	EQ043170636	32.5	84.3	49	3.5	1.3	0.1	273.2	-26.7	-63.3	568.7	B
H1450x_XF	SKS	EQ041740904	32.5	84.3	77	14.0	1.0	0.3	103.4	-10.9	166.3	152.8	B
H1450x_XF	SKS	EQ042851814	32.5	84.3	65	12.0	0.9	0.2	107.9	-17.2	167.8	25.0	B
H1450x_XF	SKS	EQ043101731	32.5	84.3	63	17.0	0.8	0.4	108.4	-18.6	169.0	186.7	B
H1450x_XF	SKS	EQ043282104	32.5	84.3	79	9.0	1.1	0.3	108.6	-24.3	179.0	532.3	A
H1450x_XF	SKS	EQ043450053	32.5	84.3	80	16.0	1.0	0.3	108.7	-18.9	169.0	137.5	A
H1450x_XF	SKS	EQ043520713	32.5	84.3	72	17.5	1.0	0.4	105.6	-21.9	-179.3	593.3	B
H1450x_XF	SKS	EQ043542013	32.5	84.3	64	9.5	1.3	0.3	102.0	-18.1	-178.9	563.8	B

Table S1. Well-defined Individual Splitting Parameters. (cont.)

H1450x_XF	SKS	EQ051401240	32.5	84.3	73	11.0	1.0	0.3	108.9	-24.5	178.8	565.3	B
H1460x_XF	SKKS	EQ043170636	32.6	84.2	43	6.5	1.2	0.2	273.3	-26.7	-63.3	568.7	B
H1460x_XF	SKKS	EQ043282104	32.6	84.2	75	17.0	0.7	0.3	108.5	-24.3	179.0	532.3	B
H1460x_XF	SKKS	EQ043520713	32.6	84.2	61	11.0	0.9	0.2	105.6	-21.9	-179.3	593.3	B
H1460x_XF	SKKS	EQ050781734	32.6	84.2	81	5.0	0.9	0.2	105.7	-21.9	-179.5	598.7	B
H1460x_XF	SKKS	EQ050801223	32.6	84.2	45	9.0	1.3	0.3	276.7	-25.0	-63.5	579.1	B
H1460x_XF	SKKS	EQ051401240	32.6	84.2	69	16.0	0.7	0.2	108.8	-24.5	178.8	565.3	B
H1460x_XF	SKKS	EQ052260239	32.6	84.2	62	16.5	0.7	0.3	291.4	-19.8	-69.0	113.8	B
H1460x_XF	SKS	EQ041740904	32.6	84.2	70	2.0	0.9	0.1	103.4	-10.9	166.3	152.8	A
H1460x_XF	SKS	EQ042820827	32.6	84.2	50	6.5	0.9	0.2	105.7	-11.0	162.2	36.0	B
H1460x_XF	SKS	EQ043101731	32.6	84.2	62	19.0	0.9	0.4	108.4	-18.6	169.0	186.7	B
H1460x_XF	SKS	EQ043282104	32.6	84.2	59	13.0	0.9	0.2	108.5	-24.3	179.0	532.3	B
H1460x_XF	SKS	EQ043450053	32.6	84.2	71	7.0	1.2	0.2	108.7	-18.9	169.0	137.5	B
H1460x_XF	SKS	EQ043520713	32.6	84.2	58	14.5	0.8	0.2	105.6	-21.9	-179.3	593.3	B
H1460x_XF	SKS	EQ050182120	32.6	84.2	58	9.5	1.1	0.3	107.2	-22.9	179.0	588.9	B
H1460x_XF	SKS	EQ050391448	32.6	84.2	62	4.5	0.8	0.1	105.6	-14.3	167.3	206.3	A
H1460x_XF	SKS	EQ050781734	32.6	84.2	54	6.0	1.0	0.1	105.7	-21.9	-179.5	598.7	A
H1460x_XF	SKS	EQ050981138	32.6	84.2	62	5.5	1.2	0.2	112.1	-23.1	169.3	10.0	B
H1460x_XF	SKS	EQ051011708	32.6	84.2	60	4.0	1.1	0.1	110.5	-22.0	170.6	68.0	A
H1460x_XF	SKS	EQ051401240	32.6	84.2	61	7.5	0.9	0.2	108.8	-24.5	178.8	565.3	A
H1470x_XF	SKKS	EQ042010801	32.7	84.2	84	6.0	1.5	0.3	19.7	49.6	-127.0	23.7	B
H1470x_XF	SKKS	EQ042400043	32.7	84.2	58	8.5	1.2	0.3	277.1	-27.4	-70.8	30.0	B
H1470x_XF	SKKS	EQ050781734	32.7	84.2	71	13.0	0.5	0.1	105.6	-21.9	-179.5	598.7	A
H1470x_XF	SKKS	EQ051531056	32.7	84.2	42	9.5	1.2	0.3	281.1	-24.2	-67.0	196.2	B
H1470x_XF	SKKS	EQ051580422	32.7	84.2	52	9.0	0.9	0.2	112.5	-29.5	-179.1	318.3	B
H1470x_XF	SKKS	EQ052040851	32.7	84.2	65	18.5	0.7	0.3	112.8	-30.3	-178.1	10.0	B
H1470x_XF	SKS	EQ041740904	32.7	84.2	57	6.5	0.6	0.1	103.4	-10.9	166.3	152.8	A
H1470x_XF	SKS	EQ041970427	32.7	84.2	44	12.0	1.0	0.3	101.4	-17.6	-178.6	560.0	B
H1470x_XF	SKS	EQ042721529	32.7	84.2	66	6.5	1.0	0.2	210.9	-52.5	28.0	10.0	B

Table S1. Well-defined Individual Splitting Parameters. (cont.)

H1470x_XF	SKS	EQ043101731	32.7	84.2	59	10.5	0.9	0.2	108.4	-18.6	169.0	186.7	B
H1470x_XF	SKS	EQ043261107	32.7	84.2	44	14.5	0.7	0.2	97.5	-15.4	-174.9	256.1	B
H1470x_XF	SKS	EQ043282104	32.7	84.2	51	14.5	0.6	0.2	108.5	-24.3	179.0	532.3	A
H1470x_XF	SKS	EQ043450053	32.7	84.2	71	15.0	0.6	0.2	108.7	-18.9	169.0	137.5	A
H1470x_XF	SKS	EQ050391448	32.7	84.2	66	8.5	0.6	0.1	105.6	-14.3	167.3	206.3	A
H1470x_XF	SKS	EQ050781734	32.7	84.2	54	7.0	0.7	0.1	105.6	-21.9	-179.5	598.7	A
H1470x_XF	SKS	EQ050981138	32.7	84.2	49	9.0	1.1	0.3	112.1	-23.1	169.3	10.0	B
H1470x_XF	SKS	EQ051011708	32.7	84.2	58	7.0	0.8	0.1	110.4	-22.0	170.6	68.0	B
H1470x_XF	SKS	EQ051401240	32.7	84.2	50	7.0	0.6	0.1	108.8	-24.5	178.8	565.3	B
H1470x_XF	SKS	EQ052230908	32.7	84.2	64	13.5	0.7	0.2	111.6	-22.7	169.5	10.0	B
H1480x_XF	PKS	EQ041662254	32.8	84.2	49	15.0	0.8	0.3	2.6	16.3	-97.8	10.0	B
H1480x_XF	SKKS	EQ043170636	32.8	84.2	62	7.5	1.0	0.2	273.5	-26.7	-63.3	568.7	B
H1480x_XF	SKS	EQ041740904	32.8	84.2	78	6.0	1.1	0.2	103.4	-10.9	166.3	152.8	A
H1480x_XF	SKS	EQ041970427	32.8	84.2	54	11.5	1.0	0.3	101.3	-17.6	-178.6	560.0	B
H1480x_XF	SKS	EQ042721529	32.8	84.2	71	15.5	0.6	0.2	210.9	-52.5	28.0	10.0	B
H1480x_XF	SKS	EQ042851814	32.8	84.2	70	9.0	0.8	0.2	107.8	-17.2	167.8	25.0	B
H1490x_XF	SKKS	EQ043170636	32.8	84.3	65	3.5	1.2	0.2	273.7	-26.7	-63.3	568.7	A
H1490x_XF	SKKS	EQ043282104	32.8	84.3	-85	7.0	1.3	0.4	108.5	-24.3	179.0	532.3	B
H1490x_XF	SKKS	EQ050801243	32.8	84.3	63	11.5	1.0	0.2	277.6	-24.7	-63.5	570.1	B
H1490x_XF	SKKS	EQ051531056	32.8	84.3	52	15.5	0.9	0.4	281.4	-24.2	-67.0	196.2	B
H1490x_XF	SKS	EQ041740904	32.8	84.3	87	7.0	1.2	0.3	103.4	-10.9	166.3	152.8	B
H1490x_XF	SKS	EQ042851814	32.8	84.3	82	12.5	0.9	0.3	107.9	-17.2	167.8	25.0	B
H1490x_XF	SKS	EQ043071002	32.8	84.3	-89	2.5	1.7	0.2	21.0	49.3	-128.8	10.0	B
H1490x_XF	SKS	EQ043101731	32.8	84.3	77	5.5	0.9	0.1	108.4	-18.6	169.0	186.7	B
H1490x_XF	SKS	EQ043282104	32.8	84.3	70	11.5	0.7	0.2	108.5	-24.3	179.0	532.3	A
H1490x_XF	SKS	EQ043450053	32.8	84.3	81	16.5	0.9	0.4	108.7	-18.9	169.0	137.5	B
H1490x_XF	SKS	EQ043542013	32.8	84.3	57	16.5	0.7	0.3	101.9	-18.1	-178.9	563.8	B
H1490x_XF	SKS	EQ050391448	32.8	84.3	83	4.0	0.9	0.1	105.7	-14.3	167.3	206.3	B
H1490x_XF	SKS	EQ050781734	32.8	84.3	73	10.5	0.7	0.1	105.6	-21.9	-179.5	598.7	A

Table S1. Well-defined Individual Splitting Parameters. (cont.)

H1490x_XF	SKS	EQ050981138	32.8	84.3	83	14.0	0.8	0.3	112.1	-23.1	169.3	10.0	B
H1490x_XF	SKS	EQ051011708	32.8	84.3	76	4.5	0.9	0.1	110.4	-22.0	170.6	68.0	A
H1490x_XF	SKS	EQ051401240	32.8	84.3	70	4.5	0.7	0.1	108.8	-24.5	178.8	565.3	A
H1490x_XF	SKS	EQ052230908	32.8	84.3	81	11.0	1.0	0.3	111.6	-22.7	169.5	10.0	B
H1500x_XF	SKKS	EQ050781734	32.9	84.3	65	19.0	0.5	0.5	105.6	-21.9	-179.5	598.7	B
H1500x_XF	SKKS	EQ050801223	32.9	84.3	39	14.5	1.2	0.4	277.2	-25.0	-63.5	579.1	A
H1500x_XF	SKKS	EQ050801243	32.9	84.3	68	11.5	1.0	0.3	277.7	-24.7	-63.5	570.1	B
H1500x_XF	SKS	EQ042721529	32.9	84.3	-86	4.0	1.2	0.2	210.9	-52.5	28.0	10.0	A
H1500x_XF	SKS	EQ050391448	32.9	84.3	87	8.5	1.1	0.3	105.7	-14.3	167.3	206.3	B
H1500x_XF	SKS	EQ050411653	32.9	84.3	76	10.0	1.3	0.3	112.1	-23.1	169.2	9.0	B
H1500x_XF	SKS	EQ050781734	32.9	84.3	73	8.0	0.8	0.2	105.6	-21.9	-179.5	598.7	A
H1500x_XF	SKS	EQ050981138	32.9	84.3	78	16.5	0.8	0.3	112.1	-23.1	169.3	10.0	B
H1500x_XF	SKS	EQ051011708	32.9	84.3	80	5.0	1.0	0.1	110.4	-22.0	170.6	68.0	A
H1500x_XF	SKS	EQ051401240	32.9	84.3	70	9.5	0.9	0.2	108.8	-24.5	178.8	565.3	B
H1510x_XF	SKKS	EQ050801223	33.0	84.3	37	10.0	1.3	0.3	277.4	-25.0	-63.5	579.1	A
H1510x_XF	SKKS	EQ050801243	33.0	84.3	80	8.0	1.6	0.5	277.9	-24.7	-63.5	570.1	B
H1510x_XF	SKS	EQ050391448	33.0	84.3	89	15.5	1.1	0.4	105.7	-14.3	167.3	206.3	B
H1510x_XF	SKS	EQ050411653	33.0	84.3	67	9.5	1.1	0.2	112.1	-23.1	169.2	9.0	B
H1510x_XF	SKS	EQ050781734	33.0	84.3	82	13.5	1.0	0.4	105.6	-21.9	-179.5	598.7	B
H1510x_XF	SKS	EQ051011708	33.0	84.3	84	7.0	1.1	0.2	110.4	-22.0	170.6	68.0	B
H1510x_XF	SKS	EQ051401240	33.0	84.3	85	7.0	1.3	0.3	108.7	-24.5	178.8	565.3	B
H1520x_XF	SKKS	EQ042010801	33.0	84.3	-85	13.5	1.5	0.7	19.8	49.6	-127.0	23.7	B
H1520x_XF	SKKS	EQ042552152	33.0	84.3	-71	8.5	0.8	0.2	219.3	-58.0	-25.3	63.9	A
H1520x_XF	SKKS	EQ043170636	33.0	84.3	68	11.5	0.7	0.2	274.1	-26.7	-63.3	568.7	B
H1520x_XF	SKKS	EQ043261141	33.0	84.3	-58	14.5	1.0	0.4	320.8	15.7	-61.7	14.0	B
H1520x_XF	SKKS	EQ050801223	33.0	84.3	55	12.0	0.9	0.2	277.5	-25.0	-63.5	579.1	A
H1530x_XF	PKS	EQ043481523	33.1	84.2	52	6.0	0.9	0.2	351.4	13.4	-89.4	62.3	B
H1530x_XF	SKS	EQ042721529	33.1	84.2	71	6.0	0.9	0.1	210.9	-52.5	28.0	10.0	B
H1530x_XF	SKS	EQ043282104	33.1	84.2	53	14.0	0.6	0.2	108.4	-24.3	179.0	532.3	B

Table S1. Well-defined Individual Splitting Parameters. (cont.)

H1530x_XF	SKS	EQ043542013	33.1	84.2	62	9.0	0.7	0.1	101.8	-18.1	-178.9	563.8	B
H1530x_XF	SKS	EQ050781734	33.1	84.2	36	11.5	0.8	0.3	105.5	-21.9	-179.5	598.7	B
H1530x_XF	SKS	EQ051401240	33.1	84.2	48	15.5	0.5	0.2	108.7	-24.5	178.8	565.3	B
H1530x_XF	SKS	EQ051660250	33.1	84.2	84	10.0	1.3	0.4	22.7	41.3	-126.0	16.0	B
H1540x_XF	PKS	EQ043200906	33.2	84.2	74	4.5	1.3	0.3	331.9	4.7	-77.5	15.0	A
H1540x_XF	SKKS	EQ043170636	33.2	84.2	56	17.5	0.5	0.2	274.3	-26.7	-63.3	568.7	B
H1540x_XF	SKKS	EQ050242323	33.2	84.2	-79	12.5	1.4	0.5	333.0	-1.4	-80.8	16.9	B
H1550x_XF	PKS	EQ051252341	33.3	84.3	88	14.0	0.8	0.4	339.1	5.1	-82.4	10.0	A
H1550x_XF	SKKS	EQ042552152	33.3	84.3	-64	13.5	1.0	0.5	219.4	-58.0	-25.3	63.9	B
H1550x_XF	SKKS	EQ051631926	33.3	84.3	-74	17.5	1.0	0.4	221.6	-56.3	-27.1	94.1	A
H1550x_XF	SKS	EQ041740904	33.3	84.3	-89	1.5	1.6	0.2	103.4	-10.9	166.3	152.8	B
H1550x_XF	SKS	EQ043542013	33.3	84.3	72	13.5	1.1	0.4	101.8	-18.1	-178.9	563.8	B
H1550x_XF	SKS	EQ050391448	33.3	84.3	-89	8.5	1.1	0.4	105.6	-14.3	167.3	206.3	B
H1560x_XF	PKS	EQ043200906	33.3	84.3	71	8.5	1.6	0.6	332.0	4.7	-77.5	15.0	B
H1560x_XF	PKS	EQ051252341	33.3	84.3	-90	7.5	1.0	0.2	339.1	5.1	-82.4	10.0	A
H1560x_XF	SKKS	EQ042552152	33.3	84.3	-78	13.0	0.5	0.2	219.4	-58.0	-25.3	63.9	A
H1560x_XF	SKS	EQ042721529	33.3	84.3	82	10.5	0.9	0.2	210.9	-52.5	28.0	10.0	B
H1570x_XF	PKS	EQ041810701	33.4	84.3	-64	12.0	0.5	0.1	347.8	10.7	-87.0	9.0	A
H1580x_XF	PKS	EQ041810701	33.5	84.3	-78	10.5	0.9	0.3	347.9	10.7	-87.0	9.0	A
H1580x_XF	PKS	EQ042832126	33.5	84.3	-84	13.5	1.3	0.5	347.5	11.4	-86.7	35.0	B
H1580x_XF	PKS	EQ043200906	33.5	84.3	-90	3.5	1.4	0.1	332.1	4.7	-77.5	15.0	A
H1580x_XF	PKS	EQ051830216	33.5	84.3	-90	4.0	1.7	0.4	346.8	11.2	-86.2	27.0	B
H1580x_XF	SKKS	EQ042552152	33.5	84.3	-71	12.5	1.0	0.4	219.5	-58.0	-25.3	63.9	A
H1580x_XF	SKKS	EQ051631926	33.5	84.3	-79	15.0	0.6	0.2	221.8	-56.3	-27.1	94.1	B
H1590x_XF	SKKS	EQ051631926	33.6	84.2	-67	13.0	0.9	0.4	221.8	-56.3	-27.1	94.1	B
H1600x_XF	PKS	EQ043200906	33.8	84.3	-85	17.5	0.6	0.2	332.2	4.7	-77.5	15.0	A
H1600x_XF	PKS	EQ051252341	33.8	84.3	-88	4.5	1.1	0.2	339.4	5.1	-82.4	10.0	B
H1600x_XF	PKS	EQ051812126	33.8	84.3	-80	11.0	1.0	0.3	341.4	8.4	-82.9	37.6	B
H1600x_XF	SKKS	EQ042552152	33.8	84.3	-67	4.5	1.3	0.3	219.6	-58.0	-25.3	63.9	A

Table S1. Well-defined Individual Splitting Parameters. (cont.)

H1600x_XF	SKS	EQ042552152	33.8	84.3	-77	9.0	1.4	0.5	219.6	-58.0	-25.3	63.9	B
H1610x_XF	PKS	EQ041810701	33.9	84.3	-87	2.0	1.4	0.2	347.9	10.7	-87.0	9.0	B
H1610x_XF	PKS	EQ043200906	33.9	84.3	82	4.0	1.4	0.2	332.3	4.7	-77.5	15.0	B
H1610x_XF	PKS	EQ051812126	33.9	84.3	-90	6.5	1.4	0.4	341.4	8.4	-82.9	37.6	B
H1610x_XF	SKKS	EQ042552152	33.9	84.3	82	17.5	0.6	0.3	219.7	-58.0	-25.3	63.9	A
H1610x_XF	SKKS	EQ051410511	33.9	84.3	83	6.5	1.6	0.3	332.5	-3.3	-81.0	39.5	B
H1610x_XF	SKS	EQ050781734	33.9	84.3	-89	2.5	1.7	0.2	105.3	-21.9	-179.5	598.7	B
H1610x_XF	SKS	EQ051011708	33.9	84.3	-84	4.5	1.4	0.3	110.3	-22.0	170.6	68.0	B
H1610x_XF	SKS	EQ052190217	33.9	84.3	82	14.0	1.2	0.4	211.9	-47.1	33.6	10.0	B
H1620x_XF	PKS	EQ041810701	34.0	84.2	-83	12.5	0.8	0.2	347.9	10.7	-87.0	9.0	A
H1620x_XF	PKS	EQ042832126	34.0	84.2	-77	7.0	0.9	0.2	347.5	11.4	-86.7	35.0	A
H1620x_XF	PKS	EQ043200906	34.0	84.2	-84	15.5	1.0	0.3	332.3	4.7	-77.5	15.0	A
H1630x_XF	PKS	EQ043250807	34.1	84.2	83	12.5	0.8	0.5	343.7	9.6	-84.2	16.0	B
H1630x_XF	PKS	EQ051252341	34.1	84.2	90	5.0	1.2	0.2	339.4	5.1	-82.4	10.0	B
H1630x_XF	SKKS	EQ042552152	34.1	84.2	89	15.0	0.7	0.3	219.8	-58.0	-25.3	63.9	B
H1630x_XF	SKS	EQ043071002	34.1	84.2	-87	11.0	1.9	0.7	20.9	49.3	-128.8	10.0	B
NBENSx_XF	SKS	EQ030040515	28.2	84.4	-86	16.0	1.1	0.5	104.9	-20.6	-177.7	378.0	B
NBENSx_XF	SKS	EQ030160053	28.2	84.4	90	10.0	0.6	0.2	23.8	44.3	-129.0	10.0	B
NDOMLx_XF	PKS	EQ030210246	28.0	84.3	-86	3.5	1.5	0.3	352.8	13.6	-90.8	24.0	A
NG020x_XF	PKS	EQ030210246	27.6	84.3	-83	4.5	1.5	0.4	352.8	13.6	-90.8	24.0	B
NG020x_XF	SKKS	EQ023571346	27.6	84.3	-74	6.0	1.2	0.2	346.4	17.0	-85.6	33.0	B
NG040x_XF	PKS	EQ023191958	27.8	84.5	-80	13.5	0.8	0.3	218.8	-56.1	-36.4	10.0	A
NG050x_XF	PKS	EQ023191958	27.9	84.6	80	12.0	0.7	0.2	218.8	-56.1	-36.4	10.0	B
NGUMBx_XF	PKS	EQ023130014	27.6	83.8	-78	4.5	1.5	0.3	352.7	13.7	-91.2	33.0	B
NGUMBx_XF	PKS	EQ030210246	27.6	83.8	-81	4.5	1.8	0.4	352.1	13.6	-90.8	24.0	B
NJANAx_XF	PKS	EQ030210246	26.7	85.9	-60	13.5	0.6	0.2	355.0	13.6	-90.8	24.0	A
NP035x_XF	PKS	EQ040620347	27.8	83.5	-88	6.5	1.4	0.4	345.2	11.6	-86.8	28.0	A
NP040x_XF	PKS	EQ030210246	27.9	83.5	-90	2.0	1.7	0.3	351.7	13.6	-90.8	24.0	B
NP050x_XF	PKS	EQ030210246	27.9	83.6	-82	6.5	1.2	0.3	351.8	13.6	-90.8	24.0	A

Table S1. Well-defined Individual Splitting Parameters. (cont.)

NP050x_XF	SKS	EQ030160053	27.9	83.6	-75	3.0	1.5	0.4	23.4	44.3	-129.0	10.0	B
NP060x_XF	PKS	EQ030210246	28.0	83.8	-87	1.0	1.6	0.2	352.0	13.6	-90.8	24.0	A
NP060x_XF	PKS	EQ030321630	28.0	83.8	-80	2.0	1.6	0.2	355.4	16.6	-92.9	211.2	B
NP060x_XF	SKS	EQ030160053	28.0	83.8	-75	2.5	1.2	0.3	23.5	44.3	-129.0	10.0	B
NP071x_XF	PKS	EQ040351159	28.1	83.8	-86	5.5	1.1	0.3	338.6	8.4	-82.9	29.2	B
NP071x_XF	PKS	EQ040561822	28.1	83.8	-85	1.0	1.4	0.2	354.2	14.0	-92.1	35.5	A
NP071x_XF	PKS	EQ040620347	28.1	83.8	-88	3.5	1.6	0.3	345.7	11.6	-86.8	28.0	B
NP080x_XF	PKS	EQ023191958	28.2	84.0	-88	9.5	0.7	0.1	219.0	-56.1	-36.4	10.0	A
NP085x_XF	PKS	EQ041200057	28.4	84.0	-84	19.5	0.7	0.3	344.6	10.8	-86.0	10.0	B
NP090x_XF	PKS	EQ023130014	28.3	83.6	-82	18.5	0.8	0.4	352.4	13.7	-91.2	33.0	A
NSINDx_XF	SKKS	EQ030040515	27.2	85.9	88	6.5	1.0	0.3	105.8	-20.6	-177.7	378.0	B
NSINDx_XF	SKKS	EQ030731254	27.2	85.9	82	12.5	0.9	0.3	101.8	-17.4	-175.2	274.9	B
SINDxx_YL	SKKS	EQ022511315	27.2	85.9	-88	7.5	0.9	0.3	109.2	-22.8	178.9	618.8	B
SINDxx_YL	SKS	EQ021111758	27.2	85.9	66	8.0	1.8	0.3	114.3	-20.5	162.2	33.0	B
SINDxx_YL	SKS	EQ022311108	27.2	85.9	-82	3.5	1.0	0.2	110.4	-23.9	178.5	675.4	B
SINDxx_YL	SKS	EQ022951139	27.2	85.9	-84	2.5	1.2	0.3	106.1	-20.6	-178.4	549.0	B
THAKxx_YL	SKS	EQ013212210	27.6	85.6	-62	11.0	1.0	0.3	151.8	-60.6	154.1	10.0	B
THAKxx_YL	SKS	EQ022311108	27.6	85.6	-78	6.5	1.2	0.4	110.2	-23.9	178.5	675.4	B
WT09xx_Y2	SKKS	EQ093211530	32.4	83.6	77	12.0	1.4	0.4	20.7	52.1	-131.4	17.0	B
WT09xx_Y2	SKKS	EQ093260748	32.4	83.6	45	17.5	0.8	0.3	101.2	-17.8	-178.4	522.6	B
WT09xx_Y2	SKKS	EQ093430946	32.4	83.6	87	15.0	0.9	0.3	110.2	-22.2	171.0	45.0	A
WT09xx_Y2	SKKS	EQ103620834	32.4	83.6	61	10.0	0.8	0.2	106.9	-23.4	-179.8	551.0	B
WT09xx_Y2	SKKS	EQ110521057	32.4	83.6	74	6.5	0.8	0.1	110.3	-26.1	178.4	558.1	A
WT09xx_Y2	SKKS	EQ110931407	32.4	83.6	67	7.0	0.9	0.2	101.1	-17.6	-178.6	551.7	A
WT09xx_Y2	SKS	EQ092751547	32.4	83.6	65	6.5	1.3	0.2	104.0	-17.0	174.5	10.0	A
WT09xx_Y2	SKS	EQ092852059	32.4	83.6	79	8.0	0.9	0.2	105.7	-14.1	166.3	35.0	B
WT09xx_Y2	SKS	EQ092901318	32.4	83.6	87	8.5	1.1	0.4	104.7	-13.0	166.4	35.0	B
WT09xx_Y2	SKS	EQ093041909	32.4	83.6	78	17.0	0.8	0.4	103.4	-11.4	166.4	133.9	A
WT09xx_Y2	SKS	EQ093061047	32.4	83.6	54	15.5	1.2	0.6	105.5	-24.1	-175.2	9.0	B

Table S1. Well-defined Individual Splitting Parameters. (cont.)

WT09xx_Y2	SKS	EQ093121546	32.4	83.6	74	17.5	0.8	0.3	106.4	-16.0	168.0	179.4	B
WT09xx_Y2	SKS	EQ093131044	32.4	83.6	70	12.5	0.8	0.2	102.3	-17.2	178.3	595.0	A
WT09xx_Y2	SKS	EQ093260748	32.4	83.6	68	7.5	0.7	0.2	101.2	-17.8	-178.4	522.6	A
WT09xx_Y2	SKS	EQ093281247	32.4	83.6	83	17.0	1.1	0.5	101.8	-20.7	-174.0	18.0	B
WT09xx_Y2	SKS	EQ093430946	32.4	83.6	69	6.0	1.0	0.1	110.2	-22.2	171.0	45.0	A
WT09xx_Y2	SKS	EQ100631402	32.4	83.6	84	5.5	1.0	0.2	104.8	-13.6	167.2	176.0	A
WT09xx_Y2	SKS	EQ102222318	32.4	83.6	77	7.5	0.9	0.2	105.4	-14.5	167.3	191.6	A
WT09xx_Y2	SKS	EQ102892008	32.4	83.6	42	12.0	1.2	0.3	101.4	-20.4	-173.8	8.0	B
WT09xx_Y2	SKS	EQ103261618	32.4	83.6	77	9.5	0.9	0.2	116.3	-33.6	-178.9	10.0	B
WT09xx_Y2	SKS	EQ103620834	32.4	83.6	89	7.5	1.3	0.3	106.9	-23.4	-179.8	551.0	A
WT09xx_Y2	SKS	EQ110050646	32.4	83.6	75	4.0	1.0	0.1	109.9	-22.3	171.6	112.2	A
WT09xx_Y2	SKS	EQ110231915	32.4	83.6	61	9.5	1.1	0.2	102.5	-20.3	-176.3	236.1	B
WT09xx_Y2	SKS	EQ110521057	32.4	83.6	69	10.5	0.7	0.2	110.3	-26.1	178.4	558.1	A
WT09xx_Y2	SKS	EQ110931407	32.4	83.6	80	15.5	0.9	0.4	101.1	-17.6	-178.6	551.7	A
WT09xx_Y2	SKS	EQ111081303	32.4	83.6	82	19.5	0.9	0.5	117.4	-34.3	179.9	86.0	A
XIXIxx_YL	SKS	EQ022951139	28.7	85.7	86	17.5	0.8	0.4	105.7	-20.6	-178.4	549.0	B

Table S2. Null Individual Splitting Parameters.

Station	**Phase**	**Event**	**St-lat.**	**St-lon.**	**Phi**	**STD of Phi**	**DT**	**STD of DT**	**BAZ**	**Ev-Lat.**	**Ev-Lon.**	**Ev-Dep.**	**R.**
BUNGxx_YL	SKS	EQ020021722	27.9	85.9	24.0	3.0	1.8	1.1	109.2	-17.6	167.9	21.0	N
H0010x_XF	PKS	EQ030220206	27.0	84.9	15.0	1.5	4.0	4.0	11.8	18.8	-104.1	24.0	N
H0010x_XF	PKS	EQ032160437	27.0	84.9	-56.0	5.0	1.8	2.9	211.3	-60.5	-43.4	10.0	N
H0010x_XF	SKKS	EQ033611600	27.0	84.9	34.0	17.0	1.3	0.7	111.8	-22.0	169.8	10.0	N
H0020x_XF	PKS	EQ032160437	27.0	84.9	42.0	21.5	0.4	0.5	211.4	-60.5	-43.4	10.0	N
H0030x_XF	PKS	EQ030220206	27.0	84.9	15.0	22.5	4.0	4.0	11.8	18.8	-104.1	24.0	N
H0030x_XF	SKS	EQ022951139	27.0	84.9	22.0	6.5	1.1	0.4	105.8	-20.6	-178.4	549.0	N
H0040x_XF	PKS	EQ032160437	27.1	84.9	-77.0	22.5	0.4	2.2	211.4	-60.5	-43.4	10.0	N
H0060x_XF	SKS	EQ030040515	27.1	85.0	18.0	22.5	4.0	4.0	105.5	-20.6	-177.7	378.0	N

Table S2. Null Individual Splitting Parameters. (cont.)

H0060x_XF	SKS	EQ030731254	27.1	85.0	-76.0	22.5	2.2	3.1	101.5	-17.4	-175.2	274.9	N
H0070x_XF	PKS	EQ030220206	27.1	85.0	15.0	1.0	4.0	4.0	11.9	18.8	-104.1	24.0	N
H0070x_XF	SKS	EQ022900423	27.1	85.0	10.0	1.0	1.6	1.9	105.1	-19.8	-178.4	627.6	N
H0080x_XF	SKS	EQ030731254	27.2	85.0	-75.0	3.5	1.6	0.8	101.5	-17.4	-175.2	274.9	N
H0090x_XF	PKS	EQ030220206	27.2	85.0	3.0	22.5	0.2	2.1	11.9	18.8	-104.1	24.0	N
H0090x_XF	SKS	EQ022951139	27.2	85.0	12.0	3.5	1.2	2.6	105.8	-20.6	-178.4	549.0	N
H0100x_XF	PKS	EQ030220206	27.2	85.0	-73.0	3.5	1.7	2.9	11.9	18.8	-104.1	24.0	N
H0100x_XF	PKS	EQ032160437	27.2	85.0	-55.0	22.5	2.4	3.2	211.4	-60.5	-43.4	10.0	N
H0100x_XF	SKS	EQ030651024	27.2	85.0	-76.0	22.5	1.3	2.6	107.6	-23.6	-175.8	10.0	N
H0100x_XF	SKS	EQ032080204	27.2	85.0	-77.0	22.5	1.9	2.9	105.5	-21.1	-176.6	212.9	N
H0100x_XF	SKS	EQ032880219	27.2	85.0	18.0	12.5	2.5	1.5	103.3	-17.8	-178.7	582.6	N
H0100x_XF	SKS	EQ033131952	27.2	85.0	-81.0	22.5	4.0	4.0	276.2	-0.7	-19.7	10.0	N
H0120x_XF	SKS	EQ033101038	27.3	85.0	-78.0	22.5	1.4	2.0	109.8	-19.3	168.9	113.7	N
H0120x_XF	SKS	EQ033611600	27.3	85.0	-87.0	12.5	0.9	0.4	111.8	-22.0	169.8	10.0	N
H0120x_XF	SKS	EQ040722213	27.3	85.0	-83.0	2.5	2.9	3.2	99.7	-15.6	-175.1	271.5	N
H0130x_XF	SKS	EQ040722213	27.3	85.0	-76.0	2.0	2.0	0.5	99.7	-15.6	-175.1	271.5	N
H0150x_XF	PKS	EQ030220206	27.4	85.0	-77.0	22.5	4.0	4.0	11.9	18.8	-104.1	24.0	N
H0150x_XF	SKS	EQ030731254	27.4	85.0	13.0	22.5	2.5	3.3	101.4	-17.4	-175.2	274.9	N
H0150x_XF	SKS	EQ031292026	27.4	85.0	54.0	18.5	0.6	0.3	212.2	-48.2	32.3	10.0	N
H0150x_XF	SKS	EQ040510558	27.4	85.0	-73.0	22.5	3.6	3.8	104.2	-11.6	166.5	84.0	N
H0170x_XF	PKS	EQ040012331	27.4	85.0	6.0	22.5	1.6	2.8	8.6	17.5	-101.3	29.4	N
H0180x_XF	PKS	EQ032372324	27.5	85.0	-59.0	22.5	0.3	2.1	15.3	18.5	-106.7	10.0	N
H0190x_XF	SKS	EQ032451828	27.5	85.0	-89.0	22.5	1.0	2.5	98.5	-15.2	-173.2	10.0	N
H0190x_XF	SKS	EQ033611600	27.5	85.0	79.0	13.0	0.8	0.3	111.8	-22.0	169.8	10.0	N
H0210x_XF	PKS	EQ030220206	27.5	85.1	17.0	22.5	0.8	2.4	11.9	18.8	-104.1	24.0	N
H0210x_XF	SKS	EQ032451828	27.5	85.1	-84.0	1.0	4.0	4.0	98.5	-15.2	-173.2	10.0	N
H0210x_XF	SKS	EQ040510558	27.5	85.1	-83.0	5.5	1.1	0.6	104.2	-11.6	166.5	84.0	N
H0220x_XF	PKS	EQ030220206	27.6	85.1	23.0	22.5	0.5	2.3	11.9	18.8	-104.1	24.0	N
H0230x_XF	PKS	EQ030220206	27.6	85.1	-83.0	22.5	0.7	2.3	11.9	18.8	-104.1	24.0	N

Table S2. Null Individual Splitting Parameters. (cont.)

H0240x_XF	PKS	EQ030220206	27.6	85.1	24.0	22.5	0.3	2.1	12.0	18.8	-104.1	24.0	N
H0240x_XF	SKS	EQ032451828	27.6	85.1	-79.0	22.5	2.3	3.2	98.5	-15.2	-173.2	10.0	N
H0250x_XF	PKS	EQ030220206	27.6	85.1	11.0	22.5	2.4	3.2	12.0	18.8	-104.1	24.0	N
H0250x_XF	SKS	EQ032451828	27.6	85.1	6.0	22.5	2.2	3.1	98.5	-15.2	-173.2	10.0	N
H0260x_XF	PKS	EQ032160437	27.7	85.1	36.0	22.5	0.7	2.4	211.6	-60.5	-43.4	10.0	N
H0260x_XF	SKS	EQ030731254	27.7	85.1	-80.0	22.5	4.0	4.0	101.4	-17.4	-175.2	274.9	N
H0270x_XF	PKS	EQ030220206	27.7	85.1	-73.0	22.5	1.2	2.6	11.9	18.8	-104.1	24.0	N
H0270x_XF	SKS	EQ030871731	27.7	85.1	-87.0	22.5	1.2	2.6	98.7	-15.3	-173.5	41.2	N
H0270x_XF	SKS	EQ030952203	27.7	85.1	-76.0	22.5	1.0	2.5	107.5	-16.2	167.9	177.5	N
H0280x_XF	PKS	EQ032160437	27.7	85.1	-80.0	22.5	0.4	0.5	211.6	-60.5	-43.4	10.0	N
H0310x_XF	PKS	EQ030220206	27.8	85.0	8.0	2.0	2.6	0.9	11.8	18.8	-104.1	24.0	N
H0330x_XF	PKS	EQ030220206	27.9	85.1	10.0	22.5	2.6	3.3	11.9	18.8	-104.1	24.0	N
H0340x_XF	PKS	EQ031711330	27.9	85.2	87.0	22.5	0.8	1.6	256.8	-30.6	-71.6	33.0	N
H0350x_XF	SKS	EQ040510558	27.9	85.1	11.0	22.5	2.6	3.3	104.2	-11.6	166.5	84.0	N
H0360x_XF	SKKS	EQ022852009	27.9	85.2	42.0	2.5	1.8	0.8	307.5	-8.3	-71.7	534.3	N
H0360x_XF	SKS	EQ041001523	27.9	85.2	-73.0	22.5	4.0	4.0	105.3	-13.2	167.2	228.4	N
H0370x_XF	SKS	EQ040510558	28.0	85.2	18.0	22.5	4.0	4.0	104.3	-11.6	166.5	84.0	N
H0380x_XF	PKS	EQ032160437	28.0	85.2	-64.0	10.0	1.1	0.6	211.7	-60.5	-43.4	10.0	N
H0390x_XF	PKS	EQ030220206	28.0	85.2	10.0	22.5	4.0	4.0	12.0	18.8	-104.1	24.0	N
H0400x_XF	PKS	EQ030220206	28.1	85.2	9.0	1.0	4.0	4.0	12.1	18.8	-104.1	24.0	N
H0440x_XF	PKS	EQ030220206	28.2	85.3	10.0	22.5	2.5	3.3	12.2	18.8	-104.1	24.0	N
H0440x_XF	SKS	EQ032160437	28.2	85.3	-61.0	22.5	4.0	4.0	211.8	-60.5	-43.4	10.0	N
H0460x_XF	PKS	EQ032160437	28.2	85.4	-81.0	22.5	0.4	1.3	211.8	-60.5	-43.4	10.0	N
H0460x_XF	SKS	EQ032451828	28.2	85.4	11.0	22.5	2.3	3.2	98.4	-15.2	-173.2	10.0	N
H0480x_XF	SKS	EQ032451828	28.3	85.4	13.0	22.5	0.8	2.4	98.4	-15.2	-173.2	10.0	N
H0490x_XF	PKS	EQ032160437	28.3	85.4	-76.0	22.5	0.5	2.2	211.9	-60.5	-43.4	10.0	N
H0490x_XF	SKS	EQ033611600	28.3	85.4	55.0	19.0	0.6	0.2	111.9	-22.0	169.8	10.0	N
H0500x_XF	PKS	EQ032160437	28.3	85.4	37.0	22.5	0.7	2.3	211.9	-60.5	-43.4	10.0	N
H0510x_XF	SKS	EQ033611600	28.4	85.4	34.0	12.0	1.3	1.2	111.9	-22.0	169.8	10.0	N

Table S2. Null Individual Splitting Parameters. (cont.)

H0540x_XF	PKS	EQ032160437	28.5	85.2	-66.0	17.5	1.1	1.5	212.0	-60.5	-43.4	10.0	N
H0550x_XF	SKS	EQ031340603	28.5	85.2	53.0	22.5	3.0	3.5	318.7	18.3	-58.6	41.5	N
H0550x_XF	SKS	EQ040510558	28.5	85.2	22.0	22.5	1.5	2.8	104.3	-11.6	166.5	84.0	N
H0560x_XF	SKS	EQ033131952	28.6	85.3	-86.0	22.5	1.4	2.7	276.6	-0.7	-19.7	10.0	N
H0570x_XF	PKS	EQ041200057	28.6	85.3	-10.0	22.5	3.9	3.9	346.6	10.8	-86.0	10.0	N
H0570x_XF	SKS	EQ033101038	28.6	85.3	32.0	15.0	1.7	0.7	109.8	-19.3	168.9	113.7	N
H0570x_XF	SKS	EQ033592042	28.6	85.3	31.0	22.5	0.9	2.5	112.2	-22.3	169.5	10.0	N
H0580x_XF	SKS	EQ033611600	28.6	85.3	26.0	22.5	2.6	3.3	111.8	-22.0	169.8	10.0	N
H0590x_XF	SKKS	EQ033611600	28.7	85.3	25.0	22.5	1.7	2.8	111.8	-22.0	169.8	10.0	N
H0600x_XF	PKS	EQ040012331	28.7	85.3	-1.0	22.5	0.5	2.2	8.7	17.5	-101.3	29.4	N
H0600x_XF	SKKS	EQ033611600	28.7	85.3	-73.0	22.5	0.9	2.4	111.8	-22.0	169.8	10.0	N
H0600x_XF	SKKS	EQ040561822	28.7	85.3	-89.0	6.0	2.2	3.1	356.3	14.0	-92.1	35.5	N
H0600x_XF	SKS	EQ032331212	28.7	85.3	55.0	15.5	1.6	0.8	133.6	-45.1	167.1	28.0	N
H0610x_XF	SKS	EQ032080204	28.8	85.3	-84.0	22.5	0.3	2.2	105.2	-21.1	-176.6	212.9	N
H0610x_XF	SKS	EQ032650445	28.8	85.3	65.0	22.5	1.9	2.9	331.5	19.8	-70.7	10.0	N
H0610x_XF	SKS	EQ033611600	28.8	85.3	28.0	22.5	1.3	2.7	111.8	-22.0	169.8	10.0	N
H0610x_XF	SKS	EQ040510558	28.8	85.3	21.0	22.5	0.3	2.2	104.4	-11.6	166.5	84.0	N
H0620x_XF	PKS	EQ040620347	28.8	85.3	81.0	22.5	1.2	2.6	348.1	11.6	-86.8	28.0	N
H0620x_XF	SKS	EQ032080204	28.8	85.3	-73.0	22.5	3.4	3.7	105.2	-21.1	-176.6	212.9	N
H0620x_XF	SKS	EQ032331212	28.8	85.3	-55.0	17.5	1.4	1.6	133.6	-45.1	167.1	28.0	N
H0620x_XF	SKS	EQ040510558	28.8	85.3	13.0	22.5	3.8	3.9	104.4	-11.6	166.5	84.0	N
H0630x_XF	PKS	EQ040012331	28.8	85.3	11.0	22.5	1.4	2.7	8.7	17.5	-101.3	29.4	N
H0630x_XF	PKS	EQ040620347	28.8	85.3	-13.0	22.5	3.8	3.9	348.1	11.6	-86.8	28.0	N
H0630x_XF	PKS	EQ041200057	28.8	85.3	84.0	22.5	0.6	2.3	346.7	10.8	-86.0	10.0	N
H0630x_XF	SKS	EQ032080204	28.8	85.3	13.0	22.5	2.7	3.3	105.2	-21.1	-176.6	212.9	N
H0630x_XF	SKS	EQ040251143	28.8	85.3	-83.0	22.5	2.1	3.1	100.2	-16.8	-174.2	129.8	N
H0630x_XF	SKS	EQ040510558	28.8	85.3	10.0	22.5	3.7	3.9	104.4	-11.6	166.5	84.0	N
H0641x_XF	PKS	EQ041200057	28.9	85.3	83.0	22.5	0.7	2.4	346.7	10.8	-86.0	10.0	N
H0641x_XF	PKS	EQ041810701	28.9	85.3	-19.0	22.5	1.1	2.5	348.2	10.7	-87.0	9.0	N

Table S2. Null Individual Splitting Parameters. (cont.)

H0641x_XF	PKS	EQ043252201	28.9	85.3	-4.0	22.5	4.0	4.0	353.3	13.4	-90.1	40.6	N
H0641x_XF	SKS	EQ041800949	28.9	85.3	-69.0	22.5	2.3	3.2	21.6	54.8	-134.3	20.0	N
H0660x_XF	PKS	EQ040620347	28.9	85.4	-24.0	22.5	0.7	1.0	348.3	11.6	-86.8	28.0	N
H0660x_XF	SKS	EQ032080204	28.9	85.4	12.0	22.5	1.3	2.7	105.2	-21.1	-176.6	212.9	N
H0660x_XF	SKS	EQ033611600	28.9	85.4	-72.0	22.5	4.0	4.0	111.9	-22.0	169.8	10.0	N
H0670x_XF	SKS	EQ032080204	28.9	85.4	-73.0	22.5	2.2	3.1	105.2	-21.1	-176.6	212.9	N
H0670x_XF	SKS	EQ032731408	28.9	85.4	30.0	3.5	1.6	1.2	114.5	-30.4	-177.4	10.0	N
H0670x_XF	SKS	EQ033611600	28.9	85.4	-70.0	22.5	3.3	3.6	111.9	-22.0	169.8	10.0	N
H0670x_XF	SKS	EQ041182328	28.9	85.4	24.0	22.5	1.1	2.6	109.1	-17.8	167.8	10.0	N
H0670x_XF	SKS	EQ041280126	28.9	85.4	24.0	22.5	3.1	3.5	111.6	-22.0	170.3	14.0	N
H0680x_XF	SKS	EQ033060532	29.0	85.4	41.0	22.5	2.4	3.2	133.9	-45.2	166.5	10.0	N
H0680x_XF	SKS	EQ033101038	29.0	85.4	-72.0	22.5	4.0	4.0	109.9	-19.3	168.9	113.7	N
H0700x_XF	PKS	EQ041200057	29.1	85.4	-15.0	22.5	2.9	3.5	347.0	10.8	-86.0	10.0	N
H0700x_XF	SKKS	EQ033602126	29.1	85.4	35.0	22.5	0.6	1.6	112.3	-22.3	169.3	10.0	N
H0700x_XF	SKS	EQ033592042	29.1	85.4	-74.0	22.5	1.1	2.5	112.2	-22.3	169.5	10.0	N
H0700x_XF	SKS	EQ040510558	29.1	85.4	-66.0	22.5	0.6	2.3	104.4	-11.6	166.5	84.0	N
H0700x_XF	SKS	EQ040692256	29.1	85.4	-71.0	17.0	1.6	1.2	116.6	-32.3	-178.4	18.4	N
H0700x_XF	SKS	EQ040962034	29.1	85.4	-84.0	22.5	0.6	2.3	103.4	-20.4	-173.9	8.0	N
H0700x_XF	SKS	EQ041071658	29.1	85.4	-84.0	22.5	0.6	2.3	108.1	-24.5	-175.9	10.0	N
H0710x_XF	PKS	EQ041200057	29.1	85.4	76.0	22.5	4.0	4.0	346.9	10.8	-86.0	10.0	N
H0710x_XF	SKS	EQ040561652	29.1	85.4	-80.0	22.5	2.4	3.2	104.1	-20.7	-175.0	55.8	N
H0710x_XF	SKS	EQ041001523	29.1	85.4	14.0	22.5	3.0	3.5	105.4	-13.2	167.2	228.4	N
H0710x_XF	SKS	EQ041071658	29.1	85.4	15.0	1.5	2.4	3.2	108.1	-24.5	-175.9	10.0	N
H0720x_XF	SKS	EQ032451828	29.1	85.4	-85.0	22.5	2.3	3.1	98.2	-15.2	-173.2	10.0	N
H0720x_XF	SKS	EQ033131952	29.1	85.4	76.0	22.5	0.7	1.7	276.8	-0.7	-19.7	10.0	N
H0730x_XF	SKS	EQ032080204	29.2	85.4	-78.0	22.5	1.6	2.8	105.1	-21.1	-176.6	212.9	N
H0730x_XF	SKS	EQ032331212	29.2	85.4	-49.0	22.5	2.6	3.3	133.6	-45.1	167.1	28.0	N
H0730x_XF	SKS	EQ032451828	29.2	85.4	14.0	22.5	0.9	2.4	98.2	-15.2	-173.2	10.0	N
H0730x_XF	SKS	EQ033101038	29.2	85.4	-72.0	22.5	2.6	3.3	109.8	-19.3	168.9	113.7	N

Table S2. Null Individual Splitting Parameters. (cont.)

H0730x_XF	SKS	EQ033592042	29.2	85.4	-70.0	22.5	2.6	3.3	112.2	-22.3	169.5	10.0	N
H0730x_XF	SKS	EQ040510558	29.2	85.4	-65.0	22.5	0.7	2.3	104.4	-11.6	166.5	84.0	N
H0730x_XF	SKS	EQ040692256	29.2	85.4	28.0	22.5	2.6	3.3	116.5	-32.3	-178.4	18.4	N
H0730x_XF	SKS	EQ040962034	29.2	85.4	16.0	22.5	2.9	1.5	103.4	-20.4	-173.9	8.0	N
H0740x_XF	PKS	EQ040620347	29.2	85.4	81.0	22.5	2.8	3.4	348.3	11.6	-86.8	28.0	N
H0740x_XF	PKS	EQ041200057	29.2	85.4	79.0	22.5	1.6	2.8	346.9	10.8	-86.0	10.0	N
H0740x_XF	SKS	EQ033561915	29.2	85.4	27.0	22.5	0.7	2.4	22.8	35.7	-121.1	8.4	N
H0740x_XF	SKS	EQ033592042	29.2	85.4	-71.0	22.5	3.3	3.6	112.2	-22.3	169.5	10.0	N
H0740x_XF	SKS	EQ041001523	29.2	85.4	16.0	22.5	4.0	4.0	105.4	-13.2	167.2	228.4	N
H0750x_XF	SKS	EQ032331212	29.2	85.3	-52.0	4.5	1.3	1.4	133.5	-45.1	167.1	28.0	N
H0760x_XF	SKKS	EQ033611600	29.3	85.2	-77.0	9.0	1.0	0.5	111.8	-22.0	169.8	10.0	N
H0760x_XF	SKS	EQ033592042	29.3	85.2	30.0	22.5	0.6	2.3	112.1	-22.3	169.5	10.0	N
H0770x_XF	SKS	EQ040110929	29.3	85.2	-78.0	22.5	1.7	2.8	105.2	-20.1	-179.2	673.1	N
H0770x_XF	SKS	EQ040692256	29.3	85.2	-60.0	1.5	4.0	4.0	116.4	-32.3	-178.4	18.4	N
H0790x_XF	PKS	EQ042832126	29.4	85.2	-15.0	22.5	1.9	2.9	347.9	11.4	-86.7	35.0	N
H0790x_XF	SKS	EQ041800949	29.4	85.2	26.0	5.0	2.8	1.3	21.6	54.8	-134.3	20.0	N
H0790x_XF	SKS	EQ042721529	29.4	85.2	38.0	11.0	1.3	0.7	211.1	-52.5	28.0	10.0	N
H0810x_XF	PKS	EQ041810701	29.5	85.2	-17.0	22.5	1.2	2.6	348.3	10.7	-87.0	9.0	N
H0810x_XF	SKKS	EQ051642244	29.5	85.2	-73.0	22.5	4.0	4.0	286.3	-20.0	-69.2	115.6	N
H1000x_XF	PKS	EQ051321115	29.3	85.9	53.0	22.5	1.4	2.7	145.0	-57.4	-139.2	10.0	N
H1000x_XF	SKS	EQ043272026	29.3	85.9	44.0	5.0	4.0	1.9	136.0	-46.7	164.7	10.0	N
H1010x_XF	PKS	EQ042531633	29.3	85.8	77.0	22.5	1.9	2.9	343.8	17.8	-81.6	25.2	N
H1010x_XF	PKS	EQ051830216	29.3	85.8	80.0	22.5	4.0	4.0	348.0	11.2	-86.2	27.0	N
H1010x_XF	SKKS	EQ051642244	29.3	85.8	-68.0	13.5	1.9	1.4	286.7	-20.0	-69.2	115.6	N
H1010x_XF	SKS	EQ043272026	29.3	85.8	-38.0	22.5	1.2	2.6	135.9	-46.7	164.7	10.0	N
H1050x_XF	PKS	EQ041810701	29.6	85.7	-84.0	22.5	0.1	2.1	349.1	10.7	-87.0	9.0	N
H1070x_XF	PKS	EQ041810701	29.8	85.8	77.0	22.5	2.5	3.3	349.2	10.7	-87.0	9.0	N
H1071x_XF	SKS	EQ050781734	29.8	85.8	-76.0	1.0	3.6	3.5	107.1	-21.9	-179.5	598.7	N
H1080x_XF	PKS	EQ041810701	29.9	85.8	86.0	22.5	0.7	2.3	349.2	10.7	-87.0	9.0	N

Table S2. Null Individual Splitting Parameters. (cont.)

H1080x_XF	PKS	EQ043250807	29.9	85.8	80.0	22.5	1.0	2.4	344.6	9.6	-84.2	16.0	N
H1080x_XF	PKS	EQ043252201	29.9	85.8	-4.0	22.5	3.2	3.6	354.1	13.4	-90.1	40.6	N
H1080x_XF	SKS	EQ041970427	29.9	85.8	-80.0	22.5	0.9	2.5	102.8	-17.6	-178.6	560.0	N
H1080x_XF	SKS	EQ050391448	29.9	85.8	-78.0	22.5	2.2	3.1	106.5	-14.3	167.3	206.3	N
H1090x_XF	PKS	EQ042832126	29.9	85.7	-7.0	22.5	1.4	2.7	348.8	11.4	-86.7	35.0	N
H1090x_XF	PKS	EQ043250807	29.9	85.7	-5.0	22.5	0.5	1.7	344.6	9.6	-84.2	16.0	N
H1090x_XF	PKS	EQ051830216	29.9	85.7	-11.0	22.5	4.0	4.0	348.0	11.2	-86.2	27.0	N
H1090x_XF	SKS	EQ043002048	29.9	85.7	-55.0	22.5	1.8	2.9	219.0	-57.1	-24.8	10.0	N
H1100x_XF	PKS	EQ041810701	30.0	85.7	-5.0	17.0	1.1	0.7	349.1	10.7	-87.0	9.0	N
H1100x_XF	SKKS	EQ043200906	30.0	85.7	68.0	22.5	1.3	2.7	332.2	4.7	-77.5	15.0	N
H1100x_XF	SKS	EQ042471904	30.0	85.7	-89.0	9.5	1.7	0.8	98.1	-15.3	-173.3	10.0	N
H1120x_XF	SKS	EQ042501242	30.1	85.4	35.0	22.5	4.0	4.0	221.2	-55.4	-29.0	10.0	N
H1140x_XF	PKS	EQ041810701	30.3	85.3	80.0	22.5	1.9	2.9	348.6	10.7	-87.0	9.0	N
H1140x_XF	PKS	EQ043252201	30.3	85.3	-3.0	3.0	1.8	0.8	353.4	13.4	-90.1	40.6	N
H1150x_XF	SKS	EQ042721529	30.4	85.3	-55.0	22.5	2.0	3.0	211.2	-52.5	28.0	10.0	N
H1160x_XF	SKS	EQ042721529	30.4	85.3	-55.0	22.5	1.4	0.9	211.2	-52.5	28.0	10.0	N
H1160x_XF	SKS	EQ050411653	30.4	85.3	-64.0	22.5	4.0	4.0	112.9	-23.1	169.2	9.0	N
H1170x_XF	SKS	EQ043272026	30.5	85.2	-46.0	22.5	4.0	4.0	135.5	-46.7	164.7	10.0	N
H1180x_XF	PKS	EQ043250807	30.6	85.2	78.0	22.5	1.4	2.7	344.0	9.6	-84.2	16.0	N
H1190x_XF	PKS	EQ051830216	30.7	85.1	-14.0	22.5	2.9	3.5	347.3	11.2	-86.2	27.0	N
H1190x_XF	SKKS	EQ051642244	30.7	85.1	-85.0	22.5	0.5	2.3	288.6	-20.0	-69.2	115.6	N
H1200x_XF	PKS	EQ043250807	30.7	85.1	-19.0	22.5	2.4	3.2	343.9	9.6	-84.2	16.0	N
H1210x_XF	PKS	EQ043252201	30.8	85.1	-9.0	22.5	2.3	3.1	353.2	13.4	-90.1	40.6	N
H1210x_XF	PKS	EQ051830216	30.8	85.1	76.0	22.5	1.6	2.8	347.3	11.2	-86.2	27.0	N
H1210x_XF	SKS	EQ042501242	30.8	85.1	45.0	22.5	3.9	3.9	221.6	-55.4	-29.0	10.0	N
H1220x_XF	PKS	EQ042832126	30.9	85.1	80.0	22.5	4.0	4.0	348.0	11.4	-86.7	35.0	N
H1220x_XF	PKS	EQ043252201	30.9	85.1	86.0	1.0	3.8	0.9	353.2	13.4	-90.1	40.6	N
H1220x_XF	SKS	EQ043272026	30.9	85.1	-77.0	22.5	0.6	1.2	135.4	-46.7	164.7	10.0	N
H1230x_XF	PKS	EQ042832126	30.9	85.1	82.0	1.0	4.0	0.4	348.1	11.4	-86.7	35.0	N

Table S2. Null Individual Splitting Parameters. (cont.)

H1230x_XF	PKS	EQ043200906	30.9	85.1	-50.0	22.5	0.4	1.0	331.8	4.7	-77.5	15.0	N
H1230x_XF	PKS	EQ043250807	30.9	85.1	77.0	22.5	1.3	2.7	344.0	9.6	-84.2	16.0	N
H1250x_XF	SKS	EQ042721529	31.1	85.0	48.0	22.5	0.2	1.9	211.1	-52.5	28.0	10.0	N
H1260x_XF	PKS	EQ041810701	31.2	85.0	86.0	22.5	1.0	2.5	348.4	10.7	-87.0	9.0	N
H1260x_XF	PKS	EQ043250807	31.2	85.0	72.0	22.5	1.7	2.9	343.9	9.6	-84.2	16.0	N
H1260x_XF	SKKS	EQ051642244	31.2	85.0	-69.0	22.5	3.5	3.7	289.5	-20.0	-69.2	115.6	N
H1270x_XF	PKS	EQ042832126	31.2	85.1	-14.0	22.5	2.1	3.1	348.1	11.4	-86.7	35.0	N
H1280x_XF	SKS	EQ043550739	31.3	85.1	-84.0	22.5	4.0	4.0	98.7	-15.9	-174.6	227.8	N
H1300x_XF	PKS	EQ042832126	31.5	85.2	76.0	6.0	4.0	4.0	348.3	11.4	-86.7	35.0	N
H1300x_XF	PKS	EQ043250807	31.5	85.2	71.0	22.5	2.2	3.1	344.2	9.6	-84.2	16.0	N
H1320x_XF	PKS	EQ042832126	31.6	85.2	75.0	1.5	4.0	1.1	348.4	11.4	-86.7	35.0	N
H1320x_XF	PKS	EQ043250807	31.6	85.2	70.0	22.5	1.5	2.8	344.3	9.6	-84.2	16.0	N
H1320x_XF	PKS	EQ051830216	31.6	85.2	-15.0	22.5	4.0	4.0	347.6	11.2	-86.2	27.0	N
H1330x_XF	PKS	EQ041810701	31.7	85.2	-6.0	22.5	2.7	3.3	348.7	10.7	-87.0	9.0	N
H1330x_XF	PKS	EQ043200906	31.7	85.2	67.0	22.5	1.3	2.6	332.4	4.7	-77.5	15.0	N
H1330x_XF	SKS	EQ042471904	31.7	85.2	-89.0	5.0	1.2	0.5	97.4	-15.3	-173.3	10.0	N
H1340x_XF	PKS	EQ042832126	31.7	85.1	71.0	22.5	1.0	2.5	348.3	11.4	-86.7	35.0	N
H1340x_XF	PKS	EQ043200906	31.7	85.1	-30.0	22.5	3.0	3.5	332.3	4.7	-77.5	15.0	N
H1340x_XF	PKS	EQ051830216	31.7	85.1	79.0	22.5	4.0	4.0	347.6	11.2	-86.2	27.0	N
H1350x_XF	PKS	EQ042832126	31.8	85.0	80.0	22.5	2.2	3.1	348.2	11.4	-86.7	35.0	N
H1370x_XF	PKS	EQ042832126	32.0	84.9	76.0	22.5	2.4	3.2	348.0	11.4	-86.7	35.0	N
H1370x_XF	PKS	EQ043252201	32.0	84.9	-75.0	22.5	0.3	2.2	353.1	13.4	-90.1	40.6	N
H1400x_XF	PKS	EQ042832126	32.1	84.7	-15.0	22.5	3.8	3.9	347.8	11.4	-86.7	35.0	N
H1421x_XF	PKS	EQ043200906	32.0	83.9	-19.0	22.5	0.6	1.3	330.7	4.7	-77.5	15.0	N
H1421x_XF	SKS	EQ050981138	32.0	83.9	-62.0	22.5	0.8	2.4	112.0	-23.1	169.3	10.0	N
H1422x_XF	PKS	EQ043200906	32.1	83.9	-31.0	22.5	3.9	4.0	330.8	4.7	-77.5	15.0	N
H1440x_XF	PKS	EQ051830216	32.5	84.2	72.0	10.0	1.8	2.0	346.5	11.2	-86.2	27.0	N
H1450x_XF	SKKS	EQ041970427	32.5	84.3	-86.0	22.5	0.8	2.4	101.4	-17.6	-178.6	560.0	N
H1490x_XF	PKS	EQ043200906	32.8	84.3	-36.0	8.0	1.1	0.5	331.7	4.7	-77.5	15.0	N

Table S2. Null Individual Splitting Parameters. (cont.)

H1500x_XF	PKS	EQ050761337	32.9	84.3	83.0	22.5	4.0	4.0	354.4	15.1	-91.4	197.4	N
H1510x_XF	PKS	EQ041810701	33.0	84.3	-15.0	22.5	3.8	3.9	347.8	10.7	-87.0	9.0	N
H1520x_XF	PKS	EQ042832126	33.0	84.3	73.0	22.5	1.3	2.7	347.4	11.4	-86.7	35.0	N
H1520x_XF	PKS	EQ043200906	33.0	84.3	-31.0	22.5	4.0	4.0	331.9	4.7	-77.5	15.0	N
H1520x_XF	SKS	EQ042501242	33.0	84.3	39.0	22.5	3.9	3.9	222.8	-55.4	-29.0	10.0	N
H1540x_XF	SKKS	EQ041970427	33.2	84.2	-82.0	22.5	1.1	2.5	101.2	-17.6	-178.6	560.0	N
H1580x_XF	SKS	EQ041970427	33.5	84.3	-73.0	22.5	1.6	2.8	101.2	-17.6	-178.6	560.0	N
H1580x_XF	SKS	EQ051680621	33.5	84.3	-68.0	22.5	4.0	4.0	23.4	40.8	-126.6	12.0	N
H1590x_XF	PKS	EQ043252201	33.6	84.2	85.0	22.5	2.5	3.3	352.3	13.4	-90.1	40.6	N
H1610x_XF	SKS	EQ041970427	33.9	84.3	10.0	22.5	3.2	3.6	101.1	-17.6	-178.6	560.0	N
H1620x_XF	SKS	EQ041970427	34.0	84.2	-81.0	22.5	4.0	4.0	101.0	-17.6	-178.6	560.0	N
NBENSx_XF	PKS	EQ030220206	28.2	84.4	-81.0	22.5	2.7	3.4	10.9	18.8	-104.1	24.0	N
NBUNGx_XF	PKS	EQ030220206	27.9	85.9	-3.0	14.5	0.5	0.2	12.9	18.8	-104.1	24.0	N
NG030x_XF	PKS	EQ030221941	27.7	84.4	9.0	22.5	3.8	3.9	11.4	18.8	-104.4	10.0	N
NG040x_XF	PKS	EQ030220206	27.8	84.5	13.0	1.5	1.7	1.2	11.1	18.8	-104.1	24.0	N
NJANAx_XF	PKS	EQ030220206	26.7	85.9	-73.0	22.5	0.6	2.3	13.2	18.8	-104.1	24.0	N
NP080x_XF	PKS	EQ030220206	28.2	84.0	-86.0	22.5	0.9	2.0	10.5	18.8	-104.1	24.0	N

REFERENCES

Agius, M., & Lebedev, S. (2017). Complex, multilayered azimuthal anisotropy beneath Tibet: evidence for co-existing channel flow and pure-shear crustal thickening. Geophysical Journal International, 210(3), 1823–1844. https://doi.org/10.1093/gji/ggx266

Basuyau, C., Diament, M., Tiberi, C., Hetényi, G., Vergne, J., & Peyrefitte, A. (2013). Joint inversion of teleseismic and GOCE gravity data: application to the Himalayas. Geophysical Journal International, 193(1), 149160. https://doi.org/10.1093/gji/ggs110

Beaumont, C., Jamieson, R. A., Nguyen, M. H., & Medvedev, S. (2004). Crustal channel flows: 1. Numerical models with applications to the tectonics of the Himalayan - Tibetan orogen. Journal of Geophysical Research, 109(B6). https://doi.org/10.1029/2003jb002809

Chen, H., Hou, M., Xiong, F., Tang, H., & Shao, G. (2021). Petrogenesis and Geodynamic Implications of Miocene Felsic Magmatic Rocks in the Wuyu Basin, Southern Gangdese Belt, Qinghai-Tibet Plateau. Minerals, 11(6), 655. https://doi.org/10.3390/min11060655

Chen, W., Martin, M., Tseng, T., Nowack, R., Hung, S., & Huang, B. (2010). Shear-wave birefringence and current configuration of converging lithosphere under Tibet. Earth and Planetary Science Letters, 295(1–2), 297–304. https://doi.org/10.1016/j.epsl.2010.04.017

Chen, W. P., & Özalaybey, S. (1998). Correlation between seismic anisotropy and Bouguer gravity anomalies in Tibet and its implications for lithospheric structures. Geophysical Journal International, 135(1), 93–101. https://doi.org/10.1046/j.1365-246x.1998.00611.x

Chen, Y., Li, W., Yuan, X., Badal, J., & Teng, J. (2015). Tearing of the Indian lithospheric slab beneath southern Tibet revealed by SKS-wave splitting measurements. Earth and Planetary Science Letters, 413, 13–24. https://doi.org/10.1016/j.epsl.2014.12.041

Christensen, N. I. (1984). The magnitude, symmetry and origin of upper mantle anisotropy based on fabric analyses of ultramafic tectonites. Geophysical Journal International, 76(1), 89–111. https://doi.org/10.1111/j.1365-246x.1984.tb05025.x

Conrad, C. P., & Behn, M. D. (2010). Constraints on lithosphere net rotation and asthenospheric viscosity from global mantle flow models and seismic anisotropy. Geochemistry, Geophysics, Geosystems, 11(5). https://doi.org/10.1029/2009gc002970

Crampin, S. (1981). A review of wave motion in anisotropic and cracked elastic-media. Wave Motion, 3(4), 343–391. https://doi.org/10.1016/0165-2125(81)90026-3

Duan, Y., Tian, X., Liang, X., Li, W., Wu, C., Zhou, B., & Iqbal, J. (2017). Subduction of the Indian slab into the mantle transition zone revealed by receiver functions. Tectonophysics, 702, 61–69. https://doi.org/10.1016/j.tecto.2017.02.025

Frederiksen, A. W., & Bostock, M. G. (2000). Modelling teleseismic waves in dipping anisotropic structures. Geophysical Journal International, 141(2), 401–412. https://doi.org/10.1046/j.1365-246x.2000.00090.x

Fu, Y., Chen, Y., Li, A., Zhou, S., Liang, X., Ye, G., Jin, G., Jiang, M., & Ning, J. (2008). Indian mantle corner flow at southern Tibet revealed by shear wave splitting measurements. Geophysical Research Letters, 35(2). https://doi.org/10.1029/2007gl031753

Gao, S., & Liu, K. (2009). Significant seismic anisotropy beneath the southern Lhasa Terrane, Tibetan Plateau. Geochemistry, Geophysics, Geosystems, 10(2). https://doi.org/10.1029/2008gc002227

Gilligan, A., & Priestley, K. (2018). Lateral variations in the crustal structure of the Indo–Eurasian collision zone. Geophysical Journal International, 214(2), 975–989. https://doi.org/10.1093/gji/ggy172

Gripp, A. E., & Gordon, R. G. (2002). Young tracks of hotspots and current plate velocities. Geophysical Journal International, 150(2), 321–361. https://doi.org/10.1046/j.1365-246x.2002.01627.x

Guo, Z., Gao, X., Yao, H., Li, J., & Wang, W. (2009). Midcrustal low-velocity layer beneath the central Himalaya and southern Tibet revealed by ambient noise array tomography. Geochemistry, Geophysics, Geosystems, 10(5). https://doi.org/10.1029/2009gc002458

Hess, H. H. (1964). Seismic Anisotropy of the Uppermost Mantle under Oceans. Nature, 203(4945), 629–631. https://doi.org/10.1038/203629a0

Hirn, A., Jiang, M., Sapin, M., Diaz, J., Nercessian, A., Lu, Q. T., Lépine, J. C., Shi, D. N., Sachpazi, M., Pandey, M. R., Ma, K., & Gallart, J. (1995). Seismic anisotropy as an indicator of mantle flow beneath the Himalayas and Tibet. Nature, 375(6532), 571–574. https://doi.org/10.1038/375571a0

Hollister, L. S., & Crawford, M. L. (1986). Melt-enhanced deformation: A major tectonic process. Geology, 14(7), 558. https://doi.org/10.1130/0091-7613(1986)14

Hsü, K. J., Guitang, P., & Sengör, A. M. C. (1995). Tectonic Evolution of the Tibetan Plateau: A Working Hypothesis Based on the Archipelago Model of Orogenesis. International Geology Review, 37(6), 473–508. https://doi.org/10.1080/00206819509465414

Hu, N., Li, Y., & Xu, L. (2019). Crustal seismic anisotropy of the Northeastern Tibetan Plateau and the adjacent areas from shear-wave splitting measurements. Geophysical Journal International, 220(3), 1491–1503. https://doi.org/10.1093/gji/ggz489

Huang, W., Ni, J., Tilmann, F., Nelson, D., Guo, J., Zhao, W., Mechie, J., Kind, R., Saul, J., Rapine, R., & Hearn, T. (2000). Seismic polarization anisotropy beneath the central Tibetan Plateau. Journal of Geophysical Research: Solid Earth, 105(B12), 27979–27989. https://doi.org/10.1029/2000jb900339

Hung, S. H., Chen, W. P., Chiao, L. Y., & Tseng, T. L. (2010). First multi-scale, finite-frequency tomography illuminates 3-D anatomy of the Tibetan Plateau. Geophysical Research Letters, 37(6). https://doi.org/10.1029/2009gl041875

IsmaïL, W. B., & Mainprice, D. (1998). An olivine fabric database: an overview of upper mantle fabrics and seismic anisotropy. Tectonophysics, 296(1–2), 145–157. https://doi.org/10.1016/s0040-1951(98)00141-3

Jia, Y., Liu, K. H., Kong, F., Liu, L., & Gao, S. S. (2021). A systematic investigation of piercing-point-dependent seismic azimuthal anisotropy. Geophysical Journal International, 227(3), 1496–1511. https://doi.org/10.1093/gji/ggab285

Jiang, M., Ai, Y., Zhou, S., & Chen, Y. J. (2014). Distribution of the low velocity bulk in the middle-to-lower crust of southern Tibet: implications for formation of the north–south trending rift zones. Earthquake Science, 27(2), 149–157. https://doi.org/10.1007/s11589-014-0080-1

Jin, Y., McNutt, M. K., & Zhu, Y. S. (1996). Mapping the descent of Indian and Eurasian plates beneath the Tibetan Plateau from gravity anomalies. Journal of Geophysical Research: Solid Earth, 101(B5), 11275–11290. https://doi.org/10.1029/96jb00531

Jolivet, L., Faccenna, C., Becker, T., Tesauro, M., Sternai, P., & Bouilhol, P. (2018). Mantle Flow and Deforming Continents: From India‐Asia Convergence to Pacific Subduction. Tectonics, 37(9), 2887‐2914. https://doi.org/10.1029/2018tc005036

Kapp, J. L., Harrison, T. M., Kapp, P., Grove, M., Lovera, O. M., & Ding, L. (2005). Nyainqentanglha Shan: A window into the tectonic, thermal, and geochemical evolution of the Lhasa block, southern Tibet. Journal of Geophysical Research, 110(B8). https://doi.org/10.1029/2004jb003330

Kapp, P., Taylor, M., Stockli, D., & Ding, L. (2008). Development of active low-angle normal fault systems during orogenic collapse: Insight from Tibet. Geology, 36(1), 7. https://doi.org/10.1130/g24054a.1

Kendall, E., Faccenda, M., Ferreira, A. M. G., & Chang, S. (2022). On the Relationship Between Oceanic Plate Speed, Tectonic Stress, and Seismic Anisotropy. Geophysical Research Letters, 49(15). https://doi.org/10.1029/2022gl097795

Klemperer, S. L. (2006). Crustal flow in Tibet: geophysical evidence for the physical state of Tibetan lithosphere, and inferred patterns of active flow. Geological Society, London, Special Publications, 268(1), 39–70. https://doi.org/10.1144/gsl.sp.2006.268.01.03

Ko, B., & Jung, H. (2015). Crystal preferred orientation of an amphibole experimentally deformed by simple shear. Nature Communications, 6(1). https://doi.org/10.1038/ncomms7586

Kong, F., Wu, J., Liu, K., & Gao, S. (2016). Crustal anisotropy and ductile flow beneath the eastern Tibetan Plateau and adjacent areas. Earth and Planetary Science Letters, 442, 72–79. https://doi.org/10.1016/j.epsl.2016.03.003

Langille, J. M., Jessup, M. J., Cottle, J. M., Newell, D., & Seward, G. (2010). Kinematic evolution of the Ama Drime detachment: Insights into orogen-parallel extension and exhumation of the Ama Drime Massif, Tibet–Nepal. Journal of Structural Geology, 32(7), 900–919. https://doi.org/10.1016/j.jsg.2010.04.005

Lease, R. O., Burbank, D. W., Zhang, H., Liu, J., & Yuan, D. (2012). Cenozoic shortening budget for the northeastern edge of the Tibetan Plateau: Is lower crustal flow necessary? Tectonics, 31(3). https://doi.org/10.1029/2011tc003066

Lee, H., Chung, S., & Yang, H. (2016). Late Cenozoic volcanism in central Myanmar: Geochemical characteristics and geodynamic significance. Lithos, 245, 174–190. https://doi.org/10.1016/j.lithos.2015.09.018

Lei, J., Zhao, D., Xu, X., Xu, Y., & Du, M. (2019). Is there a big mantle wedge under eastern Tibet? Physics of the Earth and Planetary Interiors, 292, 100–113. https://doi.org/10.1016/j.pepi.2019.04.005

Li, H., Ye, Z., Gao, R., & Huang, X. (2022). A distinct contrast in the lithospheric structure and limited crustal flow across the northeastern Tibetan Plateau: Evidence from Vs and Vp/Vs imaging. Tectonophysics, 836, 229413. https://doi.org/10.1016/j.tecto.2022.229413

Li, J., & Song, X. (2018). Tearing of Indian mantle lithosphere from high-resolution seismic images and its implications for lithosphere coupling in southern Tibet. Proceedings of the National Academy of Sciences, 115(33), 8296–8300. https://doi.org/10.1073/pnas.1717258115

Ligorría, J. P., & Ammon, C. J. (1999). Iterative deconvolution and receiver-function estimation. Bulletin of the Seismological Society of America, 89(5), 1395–1400. https://doi.org/10.1785/bssa0890051395

Liu, K., & Gao, S. (2011). Estimation of the Depth of Anisotropy Using Spatial Coherency of Shear-Wave Splitting Parameters. Bulletin of the Seismological Society of America, 101(5), 2153–2161. https://doi.org/10.1785/0120100258

Liu, K., & Gao, S. (2013). Making Reliable Shear-Wave Splitting Measurements. Bulletin of the Seismological Society of America, 103(5), 2680–2693. https://doi.org/10.1785/0120120355

Liu, L., Gao, S. S., Liu, K. H., Li, S., Tong, S., & Kong, F. (2019). Toroidal mantle flow induced by slab subduction and rollback beneath the Eastern Himalayan syntaxis and adjacent areas. Geophysical Research Letters, 46(20), 11080–11090. https://doi.org/10.1029/2019gl084961

Long, M. D., & Silver, P. G. (2009). Shear Wave Splitting and Mantle Anisotropy: Measurements, Interpretations, and New Directions. Surveys in Geophysics, 30(4–5), 407–461. https://doi.org/10.1007/s10712-009-9075-1

McKenzie, D. (1978). Active tectonics of the Alpine--Himalayan belt: the Aegean Sea and surrounding regions. Geophysical Journal International, 55(1), 217–254. https://doi.org/10.1111/j.1365-246x.1978.tb04759.x

Molnar, P., England, P., & Martinod, J. (1993). Mantle dynamics, uplift of the Tibetan Plateau, and the Indian Monsoon. Reviews of Geophysics, 31(4), 357. https://doi.org/10.1029/93rg02030

Molnar, P., Fitch, T. J., & Wu, F. T. (1973). Fault plane solutions of shallow earthquakes and contemporary tectonics in Asia. Earth and Planetary Science Letters, 19(2), 101–112. https://doi.org/10.1016/0012-821x(73)90104-0

Nabelek, J. (2002). Collaborative Research: Lithospheric Scale Dynamics of Active Mountain Building along the Himalayan-Tibetan Collision Zone [Data]. International Federation of Digital Seismograph Networks. https://doi.org/10.7914/SN/XF_2002

Nabelek, J., Hetenyi, G., Vergne, J., Sapkota, S., Kafle, B., Jiang, M., Su, H., Chen, J., Huang, B. S., & Team, T. H. C. (2009). Underplating in the Himalaya-Tibet Collision Zone Revealed by the Hi-CLIMB Experiment. Science, 325(5946), 1371–1374. https://doi.org/10.1126/science.1167719

Nair, S., Gao, S., Liu, K., & Silver, P. (2006). Southern African crustal evolution and composition: Constraints from receiver function studies. Journal of Geophysical Research: Solid Earth, 111(B2). https://doi.org/10.1029/2005jb003802

Nie, S., Tian, X., Liang, X., Chen, Y., & Xu, T. (2020). Pn uppermost mantle tomography of Central Tibet: Implication for mechanisms of N-S rifts and conjugate faults. Tectonophysics, 788, 228499. https://doi.org/10.1016/j.tecto.2020.228499

Pang, Y., Zhang, H., Gerya, T. V., Liao, J., Cheng, H., & Shi, Y. (2018). The Mechanism and Dynamics of N-S Rifting in Southern Tibet: Insight From 3-D Thermomechanical Modeling. Journal of Geophysical Research: Solid Earth, 123(1), 859–877. https://doi.org/10.1002/2017jb014011

Pasyanos, M. E., Masters, T. G., Laske, G., & Ma, Z. (2014). LITHO1.0: An updated crust and lithospheric model of the Earth. Journal of Geophysical Research: Solid Earth, 119(3), 2153–2173. https://doi.org/10.1002/2013jb010626

Roecker, S., & Levin, V. (2007). Collaborative Research: Imaging the Upper Mantle Beneath the Western Tibetan Plateau [Data]. International Federation of Digital Seismograph Networks. https://doi.org/10.7914/SN/Y2_2007

Rümpker, G., Kaviani, A., & Latifi, K. (2014). Ps-splitting analysis for multilayered anisotropic media by azimuthal stacking and layer stripping. Geophysical Journal International, 199(1), 146–163. https://doi.org/10.1093/gji/ggu154

Rümpker, G., & Silver, P. G. (1998). Apparent shear-wave splitting parameters in the presence of vertically varying anisotropy. Geophysical Journal International, 135(3), 790–800. https://doi.org/10.1046/j.1365-246x.1998.00660.x

Russo, R. M., & Silver, P. G. (1994). Trench-Parallel Flow Beneath the Nazca Plate from Seismic Anisotropy. Science, 263(5150), 1105–1111. https://doi.org/10.1126/science.263.5150.1105

Sandvol, E., Ni, J., Kind, R., & Zhao, W. (1997). Seismic anisotropy beneath the southern Himalayas-Tibet collision zone. Journal of Geophysical Research: Solid Earth, 102(B8), 17813–17823. https://doi.org/10.1029/97jb01424

Savage, M. K. (1999). Seismic anisotropy and mantle deformation: What have we learned from shear wave splitting? Reviews of Geophysics, 37(1), 65–106. https://doi.org/10.1029/98rg02075

Schellart, W., & Rawlinson, N. (2010). Convergent plate margin dynamics: New perspectives from structural geology, geophysics and geodynamic modelling. Tectonophysics, 483(1–2), 4–19. https://doi.org/10.1016/j.tecto.2009.08.030

Sheehan, A., Wu, F., & Bilham, R. (2001). Himalayan Seismotectonics, Nepal and Tibet [Data]. International Federation of Digital Seismograph Networks. https://doi.org/10.7914/SN/YL_2001

Shi, D., Lü, Q., Xu, W., Yan, J., Zhao, J., Dong, S., & Chang, Y. (2013). Crustal structure beneath the middle–lower Yangtze metallogenic belt in East China: Constraints from passive source seismic experiment on the Mesozoic intra-continental mineralization. Tectonophysics, 606, 48–59. https://doi.org/10.1016/j.tecto.2013.01.012

Shi, D., Zhao, W., Klemperer, S. L., Wu, Z., Mechie, J., Shi, J., Xue, G., & Su, H. (2016). West–east transition from underplating to steep subduction in the India–Tibet collision zone revealed by receiver-function profiles. Earth and Planetary Science Letters, 452, 171–177. https://doi.org/10.1016/j.epsl.2016.07.051

Shibutani, T., Ueno, T., & Hirahara, K. (2008). Improvement in the Extended-Time Multitaper Receiver function estimation technique. Bulletin of the Seismological Society of America, 98(2), 812–816. https://doi.org/10.1785/0120070226

Silver, P., & Chan, W. (1991). Shear wave splitting and subcontinental mantle deformation. Journal of Geophysical Research, 96(B10), 16429. https://doi.org/10.1029/91jb00899

Silver, P. G. (1996). SEISMIC ANISOTROPY BENEATH THE CONTINENTS: Probing the Depths of Geology. Annual Review of Earth and Planetary Sciences, 24(1), 385–432. https://doi.org/10.1146/annurev.earth.24.1.385

Silver, P., & Savage, M. (1994). The Interpretation of Shear-Wave Splitting Parameters In the Presence of Two Anisotropic Layers. Geophysical Journal International, 119(3), 949–963. https://doi.org/10.1111/j.1365-246x.1994.tb04027.x

Singh, A. D., Kumar, M., Raju, P. S., & Ramesh, D. S. (2006). Shear wave anisotropy of the northeast Indian lithosphere. Geophysical Research Letters, 33(16). https://doi.org/10.1029/2006gl026106

Singh, A., Eken, T., Mohanty, D. D., Saikia, D., Singh, C., & Ravi Kumar, M. (2016). Significant seismic anisotropy beneath southern Tibet inferred from splitting of direct S-waves. Physics of the Earth and Planetary Interiors, 250, 1–11. https://doi.org/10.1016/j.pepi.2015.11.001

Tao, Y., Zhang, H., Zhang, J., Pang, J., Wang, Y., Wu, Y., Zhao, X., Huang, F., & Ma, Z. (2022). Late Cretaceous–Early Cenozoic exhumation across the Yalong thrust belt in eastern Tibet and its implications for outward plateau growth. Global and Planetary Change, 216, 103897. https://doi.org/10.1016/j.gloplacha.2022.103897

Wang, Q., Hawkesworth, C. J., Wyman, D. A., Chung, S., Wu, F. Y., Li, X. H., Li, Z., Gou, G. N., Zhang, X., Tang, G., Wei, D., Ma, L., & Yu, D. (2016). Pliocene-Quaternary crustal melting in central and northern Tibet and insights into crustal flow. Nature Communications, 7(1). https://doi.org/10.1038/ncomms11888

Wessel, P., Luis, J. F., Uieda, L., Scharroo, R., Wobbe, F., Smith, W. H. F., & Tian, D. (2019). The Generic Mapping Tools version 6 [Software]. Geochemistry, Geophysics, Geosystems, 20(11), 5556–5564. https://doi.org/10.1029/2019GC008515

Wu, C., Tian, X., Xu, T., Liang, X., Chen, Y., Taylor, M., Badal, J., Bai, Z., Duan, Y., Yu, G., & Teng, J. (2019). Deformation of crust and upper mantle in central Tibet caused by the northward subduction and slab tearing of the Indian lithosphere: New evidence based on shear wave splitting measurements. Earth and Planetary Science Letters, 514, 75–83. https://doi.org/10.1016/j.epsl.2019.02.037

Wu, J., Zhang, Z., Kong, F., Yang, B. B., Yu, Y., Liu, K. H., & Gao, S. S. (2015). Complex seismic anisotropy beneath western Tibet and its geodynamic implications. Earth and Planetary Science Letters, 413, 167–175. https://doi.org/10.1016/j.epsl.2015.01.002

Yin, A., & Harrison, T. M. (2000). Geologic Evolution of the Himalayan-Tibetan Orogen. Annual Review of Earth and Planetary Sciences, 28(1), 211–280. https://doi.org/10.1146/annurev.earth.28.1.211

Zhang, B., Bao, X., Wu, Y., Xu, Y., & Yang, W. (2023). Southern Tibetan rifting since late Miocene enabled by basal shear of the underthrusting Indian lithosphere. Nature Communications, 14(1). https://doi.org/10.1038/s41467-023-38296-w

Zhang, H., Zhao, D., Yu, C., & Zhao, J. (2016). Varying deformation patterns in central Tibet revealed by radial anisotropy tomography. Journal of Geophysical Research: Solid Earth, 121(5), 3445–3461. https://doi.org/10.1002/2016jb012832

Zhao, W., Nelson, K. D., Che, J., Quo, J., Lu, D., Wu, C., & Liu, X. (1993). Deep seismic reflection evidence for continental underthrusting beneath southern Tibet. Nature, 366(6455), 557–559. https://doi.org/10.1038/366557a0

Zheng, T., Ding, Z., Ning, J., Chang, L., Wang, X., Kong, F., Liu, K., & Gao, S. (2018). Crustal Azimuthal Anisotropy Beneath the Southeastern Tibetan Plateau and its Geodynamic Implications. Journal of Geophysical Research: Solid Earth, 123(11), 9733–9749. https://doi.org/10.1029/2018jb015995

Zheng, T., Wang, J., Gao, S. S., Ding, Z., Liu, K. H., Yu, Y., Gu, Q., Fan, X., & Chang, L. (2024). Crustal Deformation Associated with the Tan-Lu Fault Zone in East China Revealed by Receiver Function Analysis. Tectonophysics, 816, 229014. https://doi.org/10.2139/ssrn.4598990

Zhu, L., & Kanamori, H. (2000). Moho depth variation in southern California from teleseismic receiver functions. Journal of Geophysical Research: Solid Earth, 105(B2), 2969–2980. https://doi.org/10.1029/1999jb900322

II. ANNUAL PERIODICITY OF SEISMIC VELOCITIES IN YELLOWSTONE CALDERA AND ITS SURROUNDING AREAS REVEALED BY VELOCITY VARIATION ANALYSIS

ABSTRACT

In our study of seismic velocity variations in the Yellowstone caldera and its adjacent area, we utilized ambient noise-based methods in conjunction with moving window across spectrum and stretching techniques to analyze 13 years of seismic data from multiple permanent stations. Most station pairs displayed a relatively stable annual velocity change trend, with three regions - Norris Geyser Basin, Hot Spring Basin, and Jackson Lake - exhibiting pronounced annual periodicity compared to the rest of the study area. These variations were influenced by different geological structures, resulting in varying degrees of impact from environmental factors on velocity changes in these regions. The Norris Geyser Basin, characterized by its porous medium, is highly responsive to external conditions. The correlation coefficient exceeding 0.5 between atmospheric temperature and the annual cyclical function suggests that temperature predominantly drives the strong periodicity in earthquake velocities in this region. Similarly, in Hot Spring Basins where independent water storage entities lack interconnectedness, there's a notable correlation between the annual period function and environmental factors, indicating that the robust annual periodicity in this area results from pore pressure changes triggered by rainfall or atmospheric pressure. In contrast, Jackson Lake, with its extensive water coverage, exhibits a significant temporal overlap between the high seismic velocity zone and the peak water volume period. This suggests

that the intense annual periodicity in seismic velocity in this area is primarily due to variations in water storage capacity.

Keywords: velocity variation, annual cycle, external environmental factors, ambient noise

PLAIN LANGUAGE SUMMARY

This study investigates changes in seismic velocities over time within the Yellowstone region, particularly near the caldera. Using an approach similar to ambient noise tomography methods, we focus on velocity variations between two stations within the study area. Our findings reveal that seismic velocity across Yellowstone National Park generally exhibits an annual periodicity, with the most pronounced effects observed in the Norris Geyser Basin (northwest corner of the caldera), the Hot Spring Basin (east of the caldera), and Jackson Lake (south of the caldera). The strong annual periodicity in these three regions is the result of a combination of various factors. Temperature acts as the primary driver in the Norris Geyser Basin, while air pressure and rainfall play pivotal roles in the Hot Spring Basin. In Jackson Lake, the dominant factor is water discharge. This study is the first to emphasize the strength of the annual velocity cycle as the central focus and analyze its underlying causes. It identifies areas with robust annual seismic velocity cycles influenced by distinct factors, offering a new perspective for future volcanic activity monitoring.

1. INTRODUCTION

Understanding changes in shallow seismic velocities is critical for interpreting geophysical data, assessing seismic hazards, and conducting subsurface mapping. Seismic velocity, the speed at which seismic waves travel through the Earth's layers, is not constant but can vary significantly based on a range of geological and environmental factors. This change is particularly noticeable at shallow depths (De Fazio et al., 1973; Roumelioti et al., 2020). The composition of soil and rock stands as a primary determinant of seismic wave propagation velocities (Schnabel et al., 1972). Consolidated rocks typically show higher velocities compared to unconsolidated sediments (Houtz et al., 1968). Within this framework, factors such as porosity and moisture content play pivotal roles in dictating propagation velocities within the same medium. High porosity generally correlates with diminished velocities due to greater wave dispersion space (Winkler, 1983; Son & Kang, 2012). Beyond intrinsic medium characteristics, external elements also contribute to shallow seismic wave velocity variations. For instance, alterations in temperature can markedly impact seismic velocity at shallow (Jones & Nur, 1983) as well as at depth (Anderson, 1987), particularly in regions marked by substantial temperature fluctuations. High temperatures tend to reduce material rigidity, consequently lowering seismic velocities (Jones & Nur, 1983). Additionally, subsurface pressure and stress conditions exert a discernible influence, with augmented pressure typically resulting in heightened velocities (Kern, 1978). The presence of cracks or faults can significantly disrupt seismic wave propagation, frequently leading to reduced velocities in these regions (Al-Shukri & Mitchell, 1988; Pointer et al., 2000; Taira et al.,

2015). Lastly, the degree of rock weathering and alteration is a factor of significance (Aster & Shearer, 1991), as weathered material often manifests lower seismic velocities compared to unaltered counterparts (Mohamad et al., 2010).

Research on the shallow seismic velocity structure in Yellowstone Park has reached a considerable level of maturity. Pioneering work by Miller and Smith (1999) and Husen et al. (2004) involved predicting the P-wave velocity structure and Vp/Vs ratio in the vicinity of the caldera. This was achieved by conducting inversions based on the first arrival times of local earthquakes and controlled source explosions. Furthermore, the identification of a low-velocity zone beneath the caldera, as revealed by teleseismic tomography, lends support to the presence of hot, potentially moisture-rich rocks ascending from the mantle transition zone, which contributes to the occurrence of hot spot volcanism (Waite et al., 2006; Yuan & Dueker, 2005). Similarly, Rayleigh wave tomography has unveiled a comparable low-velocity plume layer (Schutt et al., 2008), albeit with some disparities in the extent of the low-velocity region between the two methods. Recent research endeavors have tended to adopt a multi-methodological approach. For instance, Pasquet et al. (2016) employed a combination of resistivity tomography, seismic refraction, and surface wave profile analysis to image the subsurface at depths ranging from 15 to 30 meters. Other progress involves enhancing the accuracy of velocity structure determination by augmenting station distribution and refining associated algorithms by limiting generalized parameters to make them more relevant to local conditions (e.g., Maguire et al., 2022). These efforts aim to provide a more precise comprehension of the subterranean dynamics surrounding the caldera, including the localization of underground magma chambers, magma flow patterns, the

property of hydrothermal reservoirs, etc. (e.g., Ciraula et al., 2023; Maguire et al., 2022; Nayak et al., 2020).

While the aforementioned studies explore the seismic velocity variations at shallow depths specific to the Yellowstone area, it is also crucial to contextualize these findings within the larger framework of global seismic research. In this regard, exploring the existing body of work on annual velocity changes in diverse geological settings becomes imperative. Clements and Denolle (2018) leveraged ambient seismic noise to observe variations in seismic velocity (dv/v) associated with groundwater level fluctuations caused by drought and recharge in the San Gabriel Valley, California. Additionally, Polley et al. (2020) noted that seismic events in the L'Aquila region of Italy induced rapid shifts in near-surface velocities, whereas the hydrologic cycle induced slower changes in mid-crustal velocities. Powerful earthquakes have been shown to trigger short-term velocity reductions at stations near the rupture area, followed by recovery periods spanning days to months. This phenomenon was exemplified in events such as the 2019 Mw 7.1 Ridgecrest earthquake (Boschelli et al., 2021) and the 2021 Mw 7.4 Maduo earthquake (Huang et al., 2022). Furthermore, beyond seismic activity, other geodynamic occurrences such as volcanic activity can also correlate with seismic velocity alterations, as evidenced by the 2014 intrusion of the Bárðarbunga-Holuhraun dyke in Iceland (Donaldson et al., 2019).

Moreover, clear seasonal cycles in dv/v have been simulated and attributed to elastic and poroelastic responses linked to variations in snow thickness, atmospheric pressure, and groundwater levels. The influence of cyclical climatic factors on earthquake velocity has been observed in numerous regions, including the San Jacinto fault area. In

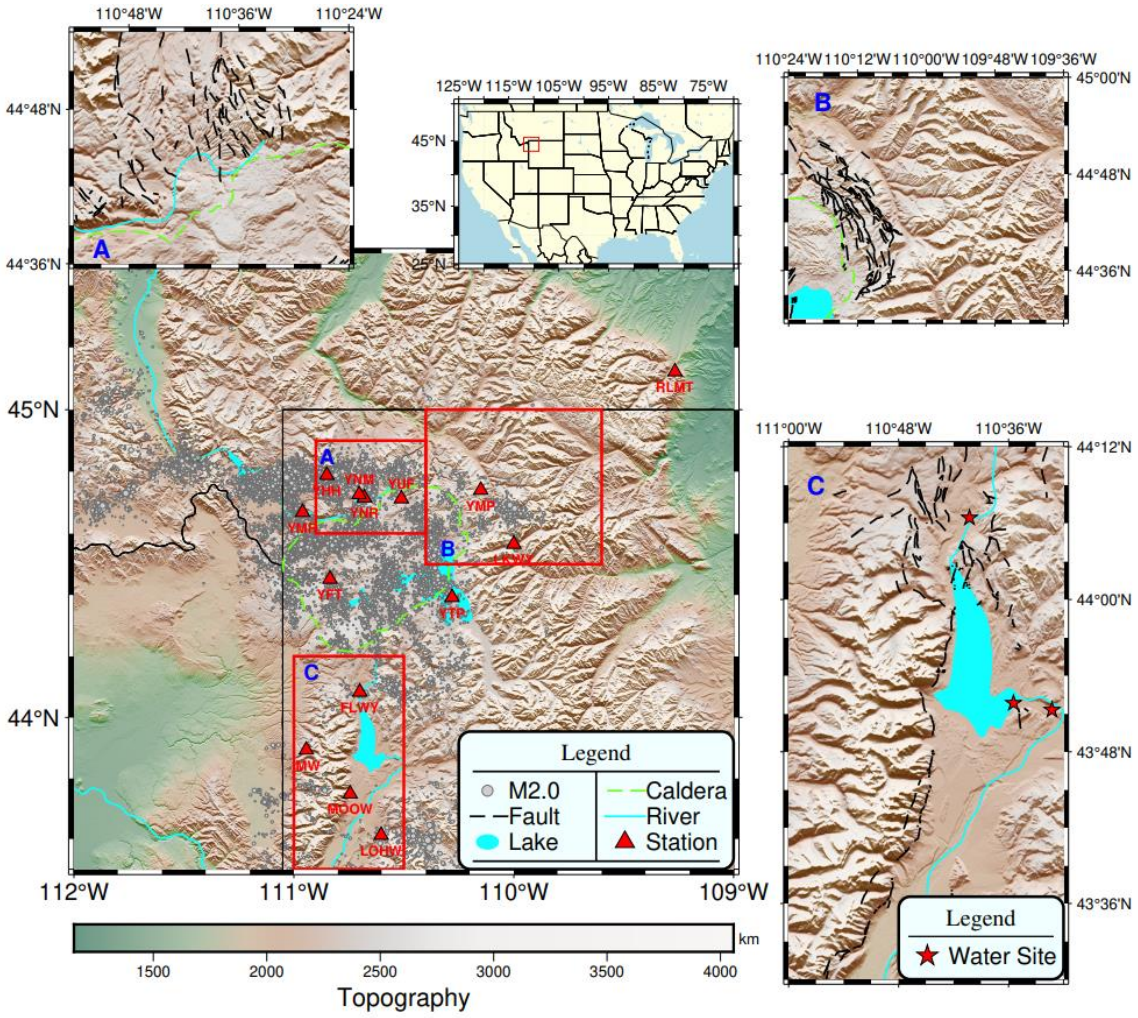

Figure 1. Yellowstone topographical map, depicting state boundaries (black solid line) and caldera demarcation (green dashed line). The gray circles, varying in size, denote earthquake events recorded from January 1, 2000, to December 31, 2022, with diverse magnitudes. The red triangles indicate the positions of permanent seismic stations employed in the study. The upper right inset offers a macroscopic overview of the research region's location. Red rectangular outlines three spots with strong seismic velocity annual cycles, and their geological features are shown in the enlarged subfigures.

this region, the primary source mechanism for the velocity's annual cycle is identified as thermoelastic strain induced by fluctuations in atmospheric temperature (Hillers et al., 2015). A similar influence is noted in Taiwan, where velocity variations are significantly

shaped by intense precipitation events associated with the Madden–Julian Oscillation (Hillers et al., 2014).

In this study, we employed approaches using ambient noise-based procedures to derive noise cross-correlation functions, which serve as the cornerstone of our analysis. This methodology was further complemented by the application of the moving window cross-spectral and stretching method, a technique pivotal in extracting precise velocity perturbations from the gathered data. The results of our comprehensive analysis reveal striking findings: three distinct areas exhibiting strong annual cycles in seismic velocity. These areas are located near the Norris Geyser Basin (Area A), the Hot Spring Basin (Area B), and Jackson Lake (Area C). Intriguingly, each of these areas is influenced by its unique set of dominating factors that contribute to the observed strong annual velocity cycles. The identification of these areas not only underscores the spatial variability of seismic velocity changes but also highlights the complex interplay of various factors at play in these regions.

Our research marks a significant advancement in our understanding of seismic velocity variations at shallow surface levels, particularly in the Yellowstone region. Spanning an unprecedented duration of 12 years, our study is the first to document long-term seismic velocity changes in Yellowstone and its adjacent area, addressing a notable gap in existing literature that largely focuses on shorter time frames. Additionally, while previous studies have primarily concentrated on limited factors influencing velocity variations near Yellowstone, our research provides a comprehensive analysis of multiple factors contributing to these changes. A particularly novel aspect of our work is the exploration of the strength and implications of the annual velocity cycle, a topic that has

not been thoroughly examined in prior studies. Furthermore, we expand the geographical scope of the investigation beyond the customary confines of the caldera rim, incorporating a broader area including regions south of the caldera. This expansive approach not only enhances the depth of our understanding but also contributes to a more holistic view of seismic behavior in this geologically significant area. Our findings offer invaluable insights for future seismic monitoring and research, paving the way for more detailed and extensive studies in this field.

2. GEOLOGICAL SETTINGS

The cyclical occurrence of rhyolite and basalt within the Yellowstone volcanic stratigraphy reflects volcanic events in the geological past: the Huckleberry Ridge Tuff Eruption (2.1 Ma), the Island Park Caldera Formation (1.3 Ma), and the Lava Creek Tuff Eruption (0.6 Ma). The outcrops from the first two stages are challenging to trace due to various geological processes, including glacial erosion. In contrast, the geological features from the third stage and the results of recent magmatic activities are observable in the vicinity of the caldera rim (White et al., 1988).

2.1. NORRIS GEYSER BASIN

Norris Geyser Basin is one of the places where Lava Creek Tuff is exposed. The vulnerability of Norris Geyser Basin's crust is supported by the presence of northeast-trending fault zones (Gardner et al., 2013) and the high b-value in seismic events (Farrell et al., 2009). Within Norris Geyser Basin, the interplay of external climatic influences

and the complex hydrological system involving a shallow low-temperature aquifer and a deep high-temperature hydrothermal reservoir (Gardner et al., 2013) amplifies the seasonal geyser eruptions (Reed et al., 2021). The presence of magnetic anomalies aligned with faults and geysers indicates that the hydrothermal alteration processes in this area are highly active (Finn & Morgan, 2002).

2.2. HOT SPRING BASIN

Hot spring basins consist primarily of multiple isolated acidification zones (Allen et al., 1935), contributing to the large lateral inhomogeneity within the crust using P wave seismic profiling (R. B. Smith et al., 1982). These acidified zones exhibit a grid-like distribution above the geothermally active land and are primarily characterized by lithologies such as Lava Creek Tuff, basalt, and Quaternary sediments (Werner et al., 2008). This location is also characterized by a relatively rare fault trend in the Yellowstone area, running almost parallel to the edge of the caldera. It also coincides with the area showing the highest horizontal gradient in both geomagnetism and pseudo-gravity data (Finn & Morgan, 2002).

2.3. JACKSON LAKE

Behrendt et al. (1968) conducted extensive geophysical studies, including gravity, seismic refraction, and aeromagnetic surveys, to uncover that the predominant rock composition in the vicinity of Jackson Lake and its surrounding mountains is gneiss. In addition to natural influences such as rainfall and snowfall, the ecological dynamics of Jackson Lake are also influenced by human activities, particularly the operation of the

Jackson Lake Dam (Marston et al., 2005). Notably, a normal fault running along the western edge of Jackson Lake introduces slight variations, including differences in riverbed permeability on both sides of the fault (McGreevy & Gordon, 1964).

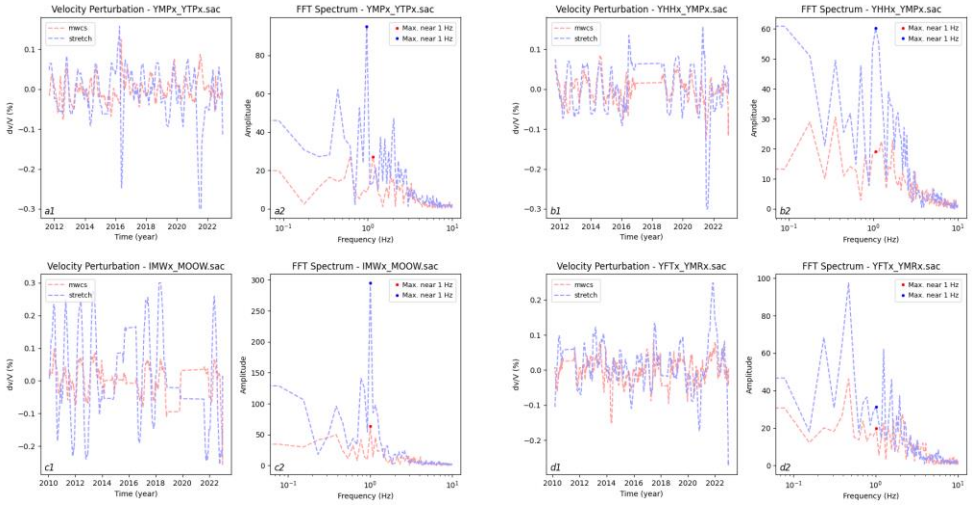

Figure 2. Velocity perturbation map spanning from January 1, 2010, to December 31, 2022. (A1) displays the dv/V results derived via the moving window cross-spectral method (red curve) and the stretching method (blue curve) for station pair YMP-YTP. (b1) represents (a1) in the frequency domain, with spheres highlighting absolute maximum amplitudes at approximately 1.0 Hz, signifying the strength of the annual cycle. (b1, b2), (c1, c2), and (d1, d2) parallel the content of (a1, a2) but pertain to station pairs YHH-YMP, IMW-MOOW, YFT-YMR, respectively.

3. DATA AND METHOD

The relative velocity perturbation approach is rooted in the principles of ambient noise theory and represents an alternative technique for investigating temporal variations in seismic velocity. As such, the data preprocessing closely resembles ambient noise tomography and encompasses procedures such as instrument response correction,

normalization, spectral whitening, cross-correlation, and stacking of the seismic traces obtained from 14 permanent stations.

To capture the temporal variations in seismic velocity occurring at daily intervals, it is imperative to obtain stacked empirical Green's functions that are both time-sensitive and exhibit high signal-to-noise ratios. To achieve this, we first conduct an initial assessment to determine if the amplitude is abnormal, defined as exceeding five times the local amplitude maximum median, for each half-hour-long data segment. If such abnormal amplitudes are detected, we proceed to artificially clip the corresponding segments, setting the clipped portion to 0. Then we down-sample the original data to intervals of half an hour instead of one day, resulting in the potential presence of up to 48 cross-correlation functions per day in theory, given a fixed station pair. We perform linear stacking of approximately 200 cross-correlation functions obtained over five consecutive days. The resulting traces, representing the empirical Green's function on the third day of the five-day period, serve as the initial input of the seismic velocity variations.

In previous studies, two primary methods were commonly employed for rapid retrieval of seismic velocity changes. These methods are known as Stretching and Moving Window Cross Spectral techniques, which were initially introduced by Sens-Schönfelder and Wegler (2006) and Poupinet et al. (1984), respectively. In this study, we utilize the empirical Green's function stacked over 13 years, from the beginning of 2010 to the end of 2022, as a static velocity model for reference. Additionally, we construct a control group for comparison by superimposing the empirical Green's function over a 10-day period.

When the propagation medium and structure do not undergo significant changes, the variation in seismic velocity (Δv) exhibits a negative correlation with the change in delay time (Δt) (Ratdomopurbo & Poupinet, 1995):

$$\frac{\Delta v}{v} = -\frac{\Delta t}{t}$$

3.1. STRETCHING

The stretching method involves adjusting Green's function in the time domain within a specific time window of the control group by retrieving a predetermined stretching coefficient. This adjustment aims to maximize the similarity between the stretched/compressed cross-correlation function and the cross-correlation function within the corresponding time window of the reference group. The error associated with the stretching method can be calculated using the approach proposed by Weaver et al. (2011):

$$Error = \frac{\sqrt{1 - X^2}}{2X} \sqrt{\frac{6\sqrt{\frac{\pi}{2}}T}{\omega_c^2(t_2^3 - t_1^3)}}$$

where X represents the maximum correlation coefficient between the identical cross-correlation functions in the control group and reference group, T is the center of the inverse of the pre-assumed frequency band, ω_c is the central pulsation, and t1 and t2 are the start and end of the time window.

3.2. MOVING WINDOW CROSS SPECTRUM

In the analysis of the paired Normalized Cross-Correlation Function between the reference group and the control group, we initiate the process by partitioning the entire function into multiple overlapping segments based on a fixed time window and a step size. These smaller segments are initially combined with an 85% taper and then transformed into the frequency domain through a fast Fourier transform ($F_{ref}(v)$ and $F_{con}(v)$ for Cross-Correlation Function in reference and control group, respectively). Subsequently, the cross-spectrum $X(v)$ is derived using a cross-correlation method, presented in the form of amplitude $|X(v)|$ and phase $\varphi(v)$:

$$X(v) = |X(v)|e^{i\varphi(v)}$$

In the absence of intricate structural complexities, it is feasible to regard velocity perturbation over a designated time frame as homogeneous. Consequently, the gradient of the cross-correlation lag time and the frequency can be approximated as a delay time parameter (Δt), localized at the midpoint of the time window. To ensure that the compared segments meet the minimum requirements for comparison, we followed the cross-coherence $C(v)$ calculation method proposed by Clarke et al. (2011) to constrain all segments. This approach enables us to establish reliable comparisons between the fragments by applying appropriate threshold (e.g., 0.65):

$$C(v) = \frac{\left|\overline{X(v)}\right|}{\sqrt{\overline{|F_{\mathrm{ref}}(v)|^2} \cdot \overline{|F_{\mathrm{con}}(v)|^2}}}$$

where the bar above represents the desired smoothing process. Additional constraints, including the maximum permissible delay time and the range for selecting the time window, should be incorporated based on the geological context and the interstation

spacing. Segments that fulfill the specified criteria will be selected, and a weighted linear regression, incorporating the weighting factor, which is the reciprocal of the error for local delay time estimation, will be executed. The reciprocal of the resultant slope value obtained through this process represents the velocity perturbation at a specific time node.

3.3. THE STRENGTH OF SEISMIC VELOCITY ANNUAL CYCLE

Surface structures on Earth are susceptible to external environmental changes, leading to periodic variations in seismic wave velocity, often occurring over yearly cycles. To investigate these periodic patterns and their spatial distribution determinants, we introduced the concept of amplitude ratio as a quantitative measure of periodicity strength. In this approach, we resampled the velocity variation curve for each station pair at a rate of one day per year (1.0/365.25) and employed fast Fourier transform to identify the local maximum value nearest to 1 Hz, denoted as A_{max}. Simultaneously, we calculated the average amplitude across the 0.5 Hz to 10 Hz range, termed A_{ave}. The ratio of A_{max} to A_{ave}, referred to as A_{rel}, served as an indicator of local cycle intensity, mitigating the influence of uncertain factors on propagation paths and velocity curves. Additionally, to counteract the impact of geometric spreading, we employed the distance (D_{x_y}) between two stations as a divisor. The resultant relative strength (A_{rel}/D_{x_y}) is evenly distributed along the assumed propagation path and is recorded on the path's grid. For all grids, we calculated the arithmetic mean and further smoothed the resultant grid image using the generalized minimum-curvature method.

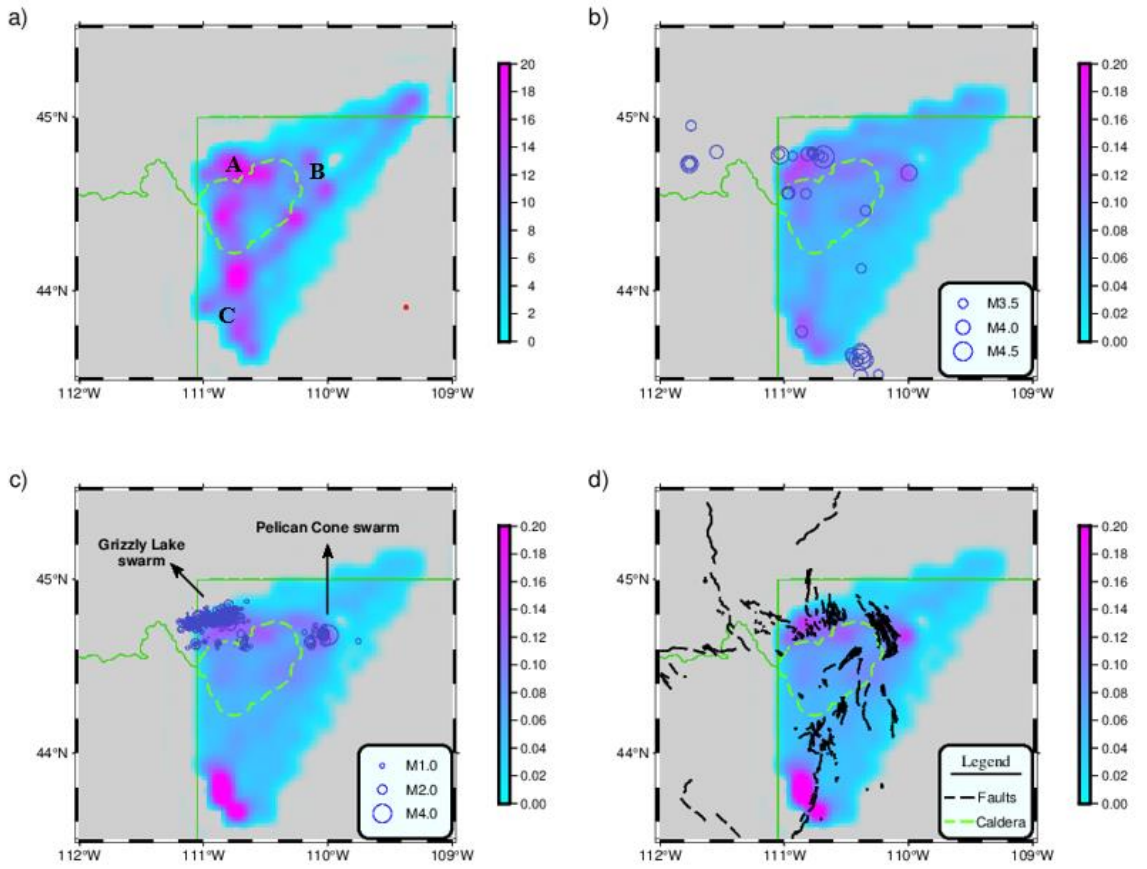

Figure 3. (a) Ray density distribution. A, B, and C mark three areas with strong annual cycle. (b) Resulting spatial distribution of annual cycle strength, obtained using the MWCS method. The current traces are composed of 40-day stacking, while the reference traces encompass a 12-year stacking. The frequency band for the traces is 0.05-0.5 Hz. Blue circles denote significant earthquake events (Ms>=3.5) since 2010. (c) Resulting spatial distribution of annual cycle strength map. Current and reference traces match those in (b) but the frequency band is set to 0.1-1.0 Hz. Blue circles signify two major earthquake swarms that occurred in 2022. (d) Same as (b) and (c) but for frequency bands 0.5-1.5 Hz.

3.4. WEATHER AND HYDROLOGICAL DATA PROCESSING

The weather, climate, and hydrological data are obtained from National Water Information System, National Oceanic and Atmospheric Administration, and Jackson Lake at Dam on Snake River near Moran operated by US Geological Survey, US Department of Commerce, and Bureau of Reclamation, respectively. The average

unregulated flow, reservoir water surface elevation, snow water equivalent, reservoir water storage, average stream discharge, precipitation and the average air temperature are calculated daily from January 1st, 2010, to Dec. 31st, 2022. The blue curves in Figure 4, 5, 6 and Figure S2, S3, S4 display all the factors in terms of time. Note that all data are normalized to correlate with strength of annual cycle.

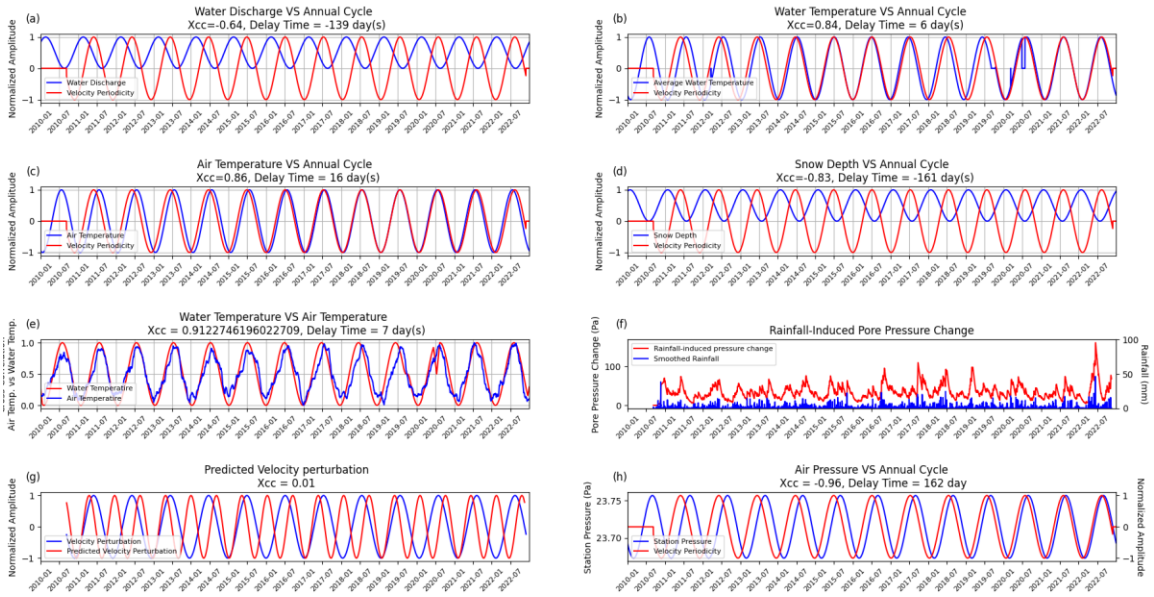

Figure 4. Cross-correlation coefficient between two parameters for Norris Geyser Basin. (a), (b), (c), (d), and (h) presents a direct comparison between various external factors and the functions exhibiting annual cycles after sinusoidal curve fitting. Subtitles within the figure provide information on different external factors, their correlation coefficients, and associated delay times. (e) A comparison between atmospheric temperature and water temperature. (f) The curve showing changes in pore pressure attributed to rainfall. (g) A comparison between the predicted curve showcasing velocity changes solely due to rainfall and the actual velocity variation curve.

4. RESULTS

4.1. VELOCITY PERTURBATION AND THE STRENGTH OF ANNUAL CYCLE

Figure 2 (a1, b1, c1, d1) illustrates the temporal evolution of dv/v for four sets of station pairs. To ensure comparability between the reference and current groups, we pre-calibrated and established coherence and cross-correlation thresholds for the MWCS and Stretching methods, respectively. Given the use of 13 years of stacking results as the reference group and a time lag window spanning a lengthy interval of -120s to +120s, we opted for a threshold of 0.5 for both methods to maintain a reasonably high signal-to-noise ratio while ensuring an adequate number of dv/v curves. The findings reveal that the trends of both methods are largely consistent, displaying a discernible annual periodicity while the stretching method exhibits slightly higher vibrational amplitudes compared to the MWCS method, resulting in a larger standard deviation in error estimation.

To ascertain whether the annual cycle predominantly influences the 13-year velocity variation, we transformed the time-domain curves into the frequency domain and denoted the absolute amplitudes (a2, b2, c2, d2 in Figure 2) acquired through the two methods. It is evident that the annual cycle plays an unequivocal dominant role in the YMP-YTP and IMW-MOOW station pairs (a2, c2 in Figure 2). In the YHH-YMP station pair, it is relatively pronounced but less so compared to the first two (b2 in Figure 2). In contrast, the YFT-YMR station pair exhibits a weaker annual cycle, and its presence is inconspicuous (d2 in Figure 2). The strength of the seismic velocity annual cycle across the entire study area falls into the above three categories: strong, relative strong, and

weak, and the three bright spots (A, B and C in Figure 1) highlight the distribution of the areas with strong annual cycles.

4.2. THE SEASONAL VARIATION AND THE CLIMATE DATA

Like velocity variation curves over time, meteorological data (water discharge a in Figure 4, ground water level h in Figure S1, water temperature b in Figure 4, and air temperature c in Figure 4.1) across the entire study area also demonstrate annual fluctuations while some specific weather data reveal either local annual periodicity (e.g., snow depth in Figure 4d) or semiannual periodicity with interannual variability (e.g., rain fall in Figure 4f). For each candidate factor, we apply feature scaling, adjusting the range to either 0 to 1 or -1 to 1, based on whether negative values held physical significance. Subsequently, we compare these normalized factors with either the highly filtered dv/v curve using a bandpass filter with corner frequencies set at 0.9 and 1.1 Hz or fitting sinusoidal functions with different orders. These two resultant curves are then subjected to full-mode cross-correlation analysis, from which we derive the lag time between the two curves and the correlation coefficient following the corresponding time shift.

4.2.1. Norris Geyser Basin (Area A). In this area, the correlation between atmospheric air temperature and surface water temperature is notably strong at 0.86, with a lag time of 16 days (Figure 4e). Furthermore, the correlation coefficient peaks at 0.84 within 6 days for the annual cycle function and the water temperature curve (refer to Figure 4b). Moreover, a qualitative examination of the association between snow depth and the annual periodic function reveals a negative correlation (depicted in Figure 4d), while the annual periodic function appears to have no direct relationship with water flow

(Figure 4a). No direct relation can be found between the annual cycle and the rainfall-or-air induced pore pressure change, evidenced my Figure 4g and 4h.

4.2.2. Hot Spring Basin Group (Area B). The region experiences abundant rainfall. While seismic velocity changes exhibit a weak direct correlation with rainfall, the alteration in pore pressure resulting from rainfall constitutes one of the primary factors influencing seismic wave velocity variations (as discussed in section 5.2), with a near perfect cross correlation for the fitting curves (Figure 5g). Different from area A, the annual cycle curves are not comparable to water temperature variations with a correlation coefficient of -0.10 (Figure 5b) and air temperature variations with a correlation coefficient of -0.12 (Figure 5c). Furthermore, the annual cycle function displays a large negative correlation with snow depth (as shown in Figure 5d) and water discharge (as shown in Figure 5a).

4.2.3. Jackson Lake (Area C). Given the extensive coverage of this area, we have selected seven stations (Figure S1) to monitor historical water flow changes. Although each station operates at varying times, they all exhibit a positive correlation between water flow (moisture content) and velocity variations (Figure S1). Rainfall exerts some influence on water flow. The annual cycle function and atmospheric temperature curve reach a peak cross-correlation coefficient after a 52-day lag (Figure 6c). The melted snow water volume itself has no clear contribution to the annual cycle, with an absolute cross-correlation coefficient close to 0 (Figure 6d). The diminutive magnitude of the cross-correlation coefficient between the annual cyclical function and factors related to pressure (Figure 6g and 6h) negates the hypothesis of their principal

causative role. Notably, the water content in this area surpasses that in areas A and B, rendering it impractical to estimate water temperature based on atmospheric temperature.

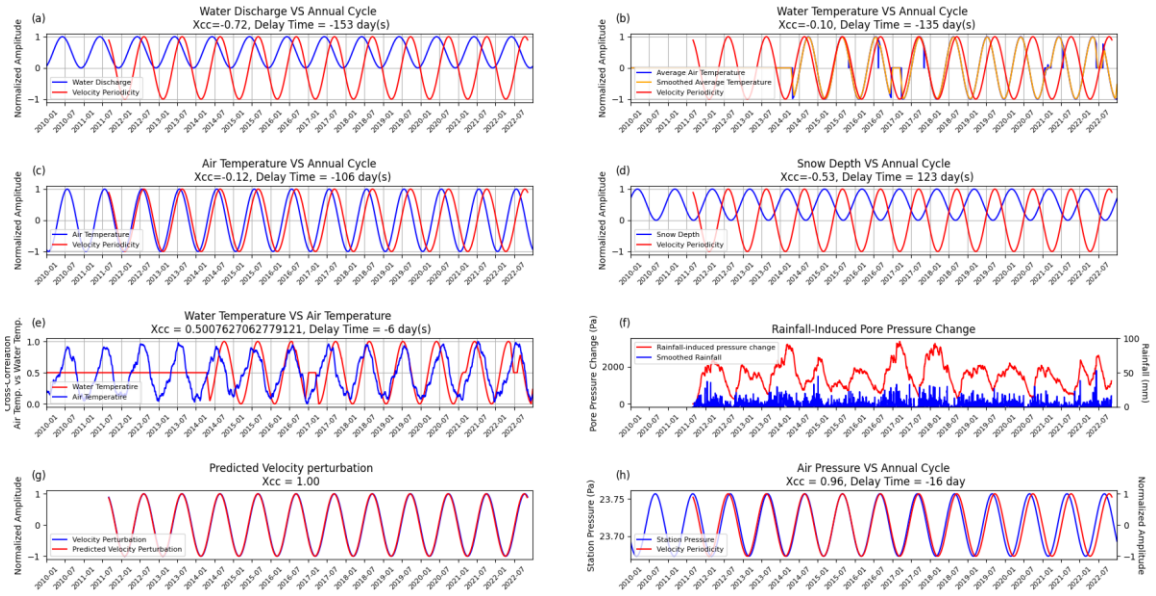

Figure 5. Same as Figure 4 but for Hot Spring Basin.

4.3. FREQUENCY-DEPENDENT ANNUAL CYCLICAL STRENGTH

In seismic exploration, the perennial debate revolves around the trade-off between high-frequency, high-resolution shallow penetration and low-frequency, low-resolution deep penetration. However, guided by the theoretical limit of ambient noise and recognizing minimal structural constraints below 15 km, this study pragmatically prescribes the frequency range to 0.04-2.00 Hz, ensuring the retention of shallow noise. The results at the lowest frequency of 0.05-0.5 Hz are depicted in Figure 3b. The comparison between the results at 0.1-1.0 Hz (Figure 3c) and 0.5-1.5 Hz (Figure 3d) reveals little marked disparities. This variance in outcomes between high and low

frequencies affirms that shallower depths are generally more prone to manifest robust annual cycles. This heightened sensitivity arises from their responsiveness to seasonal changes in surface conditions, indicating that seismic measurements in shallower layers are more attuned to surface conditions. Roumelioti et al. (2020) identified substantial impacts of seasonal variations in seismic wave velocities within shallow sediments on soil response, leading to discernible disparities in high-frequency ground motions between dry and wet seasons. Concurrently, surface temperature emerges as a principal determinant of the annual cyclical intensity. Beyond its influence on water temperature, low temperatures can induce soil frost or freezing, with the extent of impact diminishing with increasing depth. Consequently, near-surface earthquake velocities experience a marginal increase compared to normal temperatures, as substantiated by Miao et al. (2019).

5. DISCUSSION

Given that surface structures are particularly responsive to climatic changes, certain secondary surface structures or velocity-related factors (e.g., water saturation) influenced by meteorological factors may exhibit the same periodic pattern as meteorological data. However, there might be a discernible phase difference between the two due to differing response times. Owing to the intricate geological structures surrounding the Yellowstone crater, including but not limited to hydrological and altitudinal variations, the influence of diverse meteorological factors on seismic velocity varies, and the extent of their impact differs significantly, especially in three bright spots.

5.1. THE IMPACT OF ATMOSPHERIC TEMPERATURE

The influence of atmospheric temperature on the temperature gradient within the shallow crust is characterized by distinct lag times at different locations (e.g., 35 days in Japan, as observed in Wang et al., 2017; 40 to 45 days in the San Jacinto Fault Zone, as reported by Hillers et al., 2015), contingent upon the thermoelastic strain characteristics in terms of thermal expansion and diffusivity coefficient (Ben-Zion & Allam, 2013). Even though the surface water body is generally less susceptible to rapid changes in atmospheric temperature-induced thermoelastic strain due to high thermal conductivity and heat capacity, the thermal diffusivity coefficient for unconsolidated soil increases with the water content, which further indicates the better ability for moisture soil to absorbs and release heat. Furthermore, fluctuations in atmospheric temperature can induce alterations in fluid pressure within the porous and fractured matrices of geological formations, consequently modifying velocity by affecting the effective stress exerted on rock grains. Experimental findings by Zeinali and Abdelaziz (2020) indicate that pore water pressure increases with rising temperature, reaching a peak before sharply decreasing when temperature stabilizes. Variations in pore water pressure, influenced by factors like fluid saturation and porosity, can subsequently affect bulk modulus (Berryman, 1999), thereby influencing seismic wave velocity. Notably, the significance of pore pressure effects may vary, with consolidated rocks exhibiting lower porosity showing potentially less impact compared to unconsolidated sediments with higher porosity (Wyllie et al., 1958).

While the distribution of stations dictates the kilometer resolution of the annual cyclical intensity profile, the densest concentration in Norris Geyser Basin (area A) is in

its southeastern region near the crater rim. In contrast to the hard quartzite and chalcedony sinter deposits in the northern part of the basin, the rock fragments in this area are incompletely cemented by opal, leading to the creation of relatively large porosity (White et al., 1988). The consistency of temperature with the annual cyclical function shows the dominant role in this region (Figure 4c). Within the framework of a two-dimensional elastic half-space subjected to plane strain conditions, the sensitivity kernel is estimated to span 3-5 km for frequencies ranging from 0.1 to 1.0 Hz, enabling the derivation of strain delay relative to temperature variations as 8 /T, with T symbolizing the wave's period (Tsai, 2011). In the context of Area A, the calculated delay duration approximates 36 days, which is significantly larger than the realistic 16 days. A potential explanation is that the fault pores within this region are saturated with water, enhancing the propagation velocity of thermoelastic strain, and thereby diminishing the delay interval. An alternative theory posits that the heat source is not situated at the Earth's surface but rather at a proximal upper stratum, which abbreviates the delay period by curtailing the propagation path (Ben‐Zion & Leary, 1986). The source heat can be the water temperature variation affected by the air temperature (Figure 4c and 4e). The lower correlation coefficient in the hot spring basin (area B) excludes the possibility that temperature plays a dominant role in this area. For Jackson Lake (area C), the relatively high similarity between atmospheric temperature and the annual cycle (Figure 6c) indicates secondary factors affecting velocity variations. The primary explanations for different regions will be elucidated later.

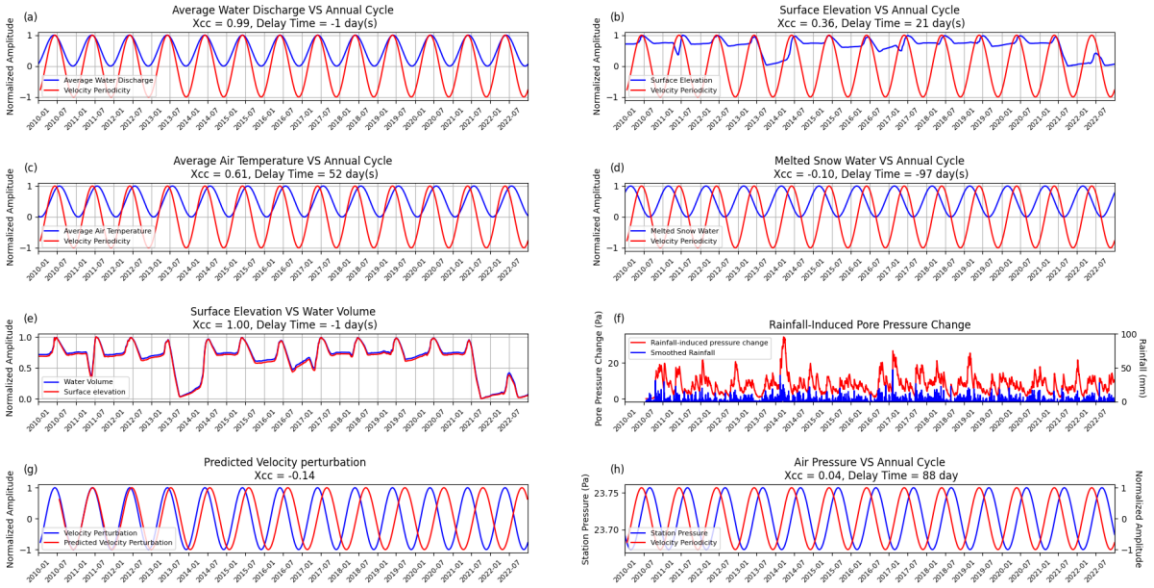

Figure 6. Same as Figure4 but for Jackson Lake. Note that (e) is the comparison between water surface elevation and the water volume.

5.2. THE IMPACT OF PRECIPITATION

Regional external factors, such as seasonal rainfall, inevitably impact surface seismic velocity, with their contribution contingent on precipitation volume and local geological and hydrological structures. The interaction of heavy rainfall with unconsolidated sediments can induce sediment erosion and transport, altering seismic wave velocity by modifying the original sediment composition (Zhang & Wang, 2017). However, this process is time-consuming and irreversible, making it challenging to replicate on an annual cycle. Annual fluctuations in seismic velocities due to rainfall are more likely attributed to variations in pore pressure. Rainfall infiltrates the ground, filling subsurface pore spaces, and alters the effective stress of subsurface materials by elevating pore pressure (Zhan et al., 2007). Increased pore pressure tends to diminish seismic

velocities, especially in unconsolidated sediments, as it affects the stiffness and compressibility of the porous medium (Bachrach et al., 2001; Zhao, 2005).

To assess the influence of rainfall on the local area, we employ the one-dimensional fully coupled diffusion equation (Talwani et al., 2007) in conjunction with local rainfall data to model the cumulative variations in pore pressure (P):

$$P(r,t) = \sum_{i=1}^{n} \rho \cdot g \cdot \delta h_i \cdot erfc\left[\frac{r}{\sqrt{4c(n-1)\delta t}}\right],$$

where n and δt represent the sample size (100 days in this study) and the moving step in the time window (1 day in this study) respectively, $\rho \cdot g \cdot \delta h_i$ is the water pressure change induced by rainfall at a given time node δt_i, r signifies the diffusion depth designated as 3 km to align with the local sensitivity kernel, c is the diffusion rate (m^2/s), and *erfc(x)* is the complementary error function. Following the similar procedure constructed by Wang et al. (2017) and Feng et al. (2021), we assume a linear positive correlation between velocity changes and pore pressure changes, denoted by the equation $\frac{\Delta v}{v}_{pred} = K \cdot P + B$, where the amplification coefficient K is represented by $cov\left(\frac{\Delta v}{v}_{real}(t),\ P(t)\right)/var(P(t))$, and the intercept 'B' is a constant computed by $\overline{\frac{\Delta v}{v}_{real}(t)} - K \cdot \overline{P(t)}$, where the bar on the top indicates the average of corresponding variable. It is essential to highlight that the velocity variation $\frac{\Delta v}{v}_{real}(t)$ employed for amplification factor calculation is a highly filtered velocity variation curve. Subsequently, a grid search is conducted to identify the optimal diffusion coefficient (*c*) within the range of 0.1 to 10 m^2/s at intervals of 0.1 m^2/s, aiming to minimize the sum of squares of residuals (σ^2) between true velocity changes and predicted velocity changes:

$$\sigma^2(c) = \frac{1}{n}\sum_{i=1}^{n}\left(\frac{\Delta v}{v}_{real}(i) - \frac{\Delta v}{v}_{pred}(i,c)\right)^2.$$

The optimal diffusion rates for Norris Geyser Basin (area A), Hot Spring Basin (area B), and Jackson Lake (area C) are determined to be 0.2, 1.2, 0.2 m^2/s, respectively. To assess the influence of predicted velocity variation curves resulting from rainfall-induced pore pressure changes, cross-correlation calculations are performed with true curves. Due to data quality variations, temporal discontinuities, and impact of seismic events on the original data, gaps exist in the real seismic velocity variation curves, leading to a reduction in the cross-correlation coefficient. Despite this, the correlation coefficient surpasses 70%, suggesting that pore pressure changes induced by rainfall are the primary factor influencing seismic velocity changes in Area B. Conversely, for Jackson Lake (area C), where more than 80% of the region is covered by lake water, the influence of pore pressure changes caused by rainfall can be neglected.

5.3. THE IMPACT OF AIR PRESSURE

Atmospheric pressure typically exerts an indirect impact on surface seismic velocity by influencing pore pressure. This influence from atmospheric pressure possesses a more protracted periodicity and broader scope compared to other factors such as temperature (Luan et al., 2022). Furthermore, it can emerge as a potential factor in the occurrence of significant earthquakes (Chen et al., 2014; Gao et al., 2000). The alteration in atmospheric pressure can, over an extended duration, modify the strain load to the sub-surface (Tsai, 2011), consequently influencing pore pressure through changes in

permeability. Simultaneously, short-term variations in air pressure can swiftly affect pore content by manipulating pressure differentials within pores and capillary phenomena.

In our analysis, Norris Geyser Basin and Jackson Lake exhibit an approximate 100-day phase difference between the annual cycle and the fitting atmospheric pressure at stations, with a cross-correlation coefficient below 0.1 (Figure 4h and Figure 6h). This suggests that atmospheric pressure has no direct impact on velocity changes in these two areas. Conversely, in Hot Spring Basin, a notable phase correlation is observed between the smoothed pressure curve and the velocity annual cyclical curve, with a theoretical phase difference of 16 days (Figure 5h). The correlation coefficient surpassing 0.5 (Figure 5h) indicates that air pressure influences pore pressure through geological and hydrological property changes, subsequently affecting velocity changes. Building on the previous chapter's conclusion that the strong annual periodicity in Hot Spring Basin is induced by pore pressure changes from rainfall, we can augment this finding by suggesting that the strong annual periodicity in area B results from a combination of pore pressure changes induced by both rainfall and atmospheric pressure. It's important to note that pressure and rainfall are interconnected factors; for instance, low-pressure systems often stimulate cloud formation and precipitation (Hurley & Boos, 2014). Consequently, the velocity changes in area B are attributed to climatic factors, and further detailed research is warranted to discern the specific dominant influences.

5.4. THE IMPACT OF WATER DISCHARGE

Water discharge, the movement of water in rivers, streams, or other water bodies, can impact near-surface seismic velocities through various mechanisms. Similar to

rainfall, it primarily influences seismic velocities by altering pore pressure, sediment transport, and groundwater flow. Rapid changes in water discharge rate over a specific timeframe can lead to the redistribution of dynamic loads and stresses near the surface, exerting real-time effects on seismic velocity. Significantly, in areas predominantly covered by water (such as area C), variations in water discharge rate can serve as a proxy for groundwater content (Figure 6b and Figure S1h), subsequently reflecting water saturation. A higher water discharge rate indicates increased groundwater content, resulting in relatively larger seismic wave velocities compared to the low water flow stage in the same area, and vice versa.

For area A, water discharge data were sourced from Tantalus Creek in Norris, coinciding with the region exhibiting the highest intensity of the annual cycle. Normalized discharge data indicate a weak annual periodicity of water flow in this area, showing no direct and clear correlation with the annual periodicity of seismic velocities. Due to the absence of long-term active surface water monitoring stations in area B, the nearest available station, located in the northern part of Yellowstone Park Lake, does not accurately represent local water flow. In area C, encompassing the north, south, and east of Jackson Lake, seven surface water monitoring stations were available (three of them are plotted in Figure1). Normalized data from these stations revealed a conspicuous annual periodicity in peak water flow, with high peaks occurring from May to July each year, reaching 3 to 5 times higher discharge rate than in other months. The peak water flow corresponds to the maximum value of seismic velocity. Despite artifacts introduced to prevent transients in the 2010 and 2022 periodic functions due to edge effects from the interaction of the finite duration filter with the boundary signal (Wallén et al., 2013), the

comparison of average water flow and the annual periodic function of velocity (Figure 6a) shows a correlation coefficient reaching 0.99, and a lag time of 1 days illustrates the decisive role of surface aquifer saturation in causing the strong annual periodicity in this area.

5.5. THE IMPACT OF FAULTS AND SEISMIC EVENTS

Faults and earthquake events are primarily causative factors influencing seismic velocities. Faults represent structural discontinuities resulting from the compaction or expansion of the Earth's crust, and the stresses and strains generated by earthquake events offer external support for structural changes in the Earth's crust. The 2016 Borrego Springs earthquake, marked by a magnitude of 5.2 and attributed to relative plate motion along the San Jacinto fault zone induced, significant disturbances in both the fault zone and the nearby environment. This seismic event led to a swift reduction in seismic velocities, as detailed by Qiu et al. (2019). A comparable incident unfolded in Maduo in 2021, involving a seismic event of magnitude 7.4. This earthquake resulted in a discernible reduction in rock slope velocity, estimated at 0.41%, as determined through dv/v analysis (Huang et al., 2022). In the context of Yellowstone, earthquakes mainly arise from the movement of magma beneath the surface, leading to the accumulation of pressure and stress until it surpasses the elastic limit of the rock. While volcanic earthquakes release relatively small energy (not exceeding 4.5 Richter magnitude in this study area), it is sufficient to impact the elastic properties of the subsurface in terms of crack opening and closing.

In comparison to tectonic earthquakes, volcanic earthquakes can have a pronounced effect on the elastic properties of the subsurface, specifically regarding crack dynamics. Faults, in this context, can serve as conduits for fluid flow. The movement of fluids along faults induces changes in pore pressure, thereby influencing seismic velocities. Consequently, climate-induced alterations in seismic velocity are particularly notable in regions characterized by abundant faults and seismic activity. In the case of Area C, a significant fault traverses Jackson Lake, and the occurrence of the two largest earthquake swarms in 2022 (Grizzly Lake earthquake swarm and Pelican Cone earthquake swarm in Figure 3c) further emphasizes the intricate interplay of faulting and seismic events in influencing seismic velocities.

6. CONCLUSIONS

Utilizing ambient seismic noise, we monitored velocity fluctuations within and surrounding the Yellowstone caldera over thirteen years, observing that these perturbations exhibit periodic variations on an annual scale. Notably, the Norris Geyser Basin (area A) located northwest of the crater, Hot Spring Basin to the west (area B), and Jackson Lake towards the south (area C) demonstrated the most pronounced annual changes. Through a cross-correlation analysis between environmental parameters and the modeled annual cycle function, it was determined that the primary contributors to velocity perturbations in area A include atmospheric temperature. Alterations in surface water temperature and subsurface heat sources collectively reduce the lag time of the velocity disturbance curve. In area B, the annual cycle of velocity fluctuation is

predominantly attributed to variations in pore pressure induced by precipitation. The impact of atmospheric pressure on porosity-related pressure changes in this area is also significant, whereas, in region C, the primary driver of annual velocity changes is the alteration in pore water saturation resulting from shifts in water storage. Moreover, the extensive fault networks present in these areas enhance the susceptibility of their velocities to external environmental factors.

ACKNOWLEDGEMENTS

We thank the Seismological Facility for the Advancement of Geoscience (SAGE) Data Management Center for providing access to the seismic data used in this study. The service for downloading seismic data is funded through the Nation Science Foundation's Seismological Facility for the SAGE Award under Cooperative Agreement EAR-1724509. The study was partially supported by the U.S. National Science Foundation under awards 1830644 and 2149587 to K.L. and 1919789 to S.G.

DATA AVAILABILITY

All the data used in the study are publicly available from the Seismological Facility for the Advancement of Geoscience Data Management Center, using the BREQ_FAST data requesting procedure (https://ds.iris.edu/ds/nodes/dmc/forms/breqfast-request/). Note that the email-based BREQ_FAST request will be replaced by FetchData (https://github.com/EarthScope/fetch-scripts) and ROVER (https://earthscope.github.io/rover). The seismic data includes the networks IW

(10.7914/SN/IW; ASL, 2003), US (10.7914/SN/US; ASL, 1990), and WY (10.7914/SN/WY; University of Utah, 1983). To demonstrate the quality of the results, during the review process of this paper, the velocity variation curves using various parameters can be found at web.mst.edu - /csgg2/09_Yellowstne_dvv_Stretch/ and web.mst.edu - /csgg2/10_Yellowstne_dvv_MWCS/. Figures were made with Generic Mapping Tools version 4.5.7 and 6.2.0 (Wessel et al., 2019) and python 3.7.3.

APPENDIX

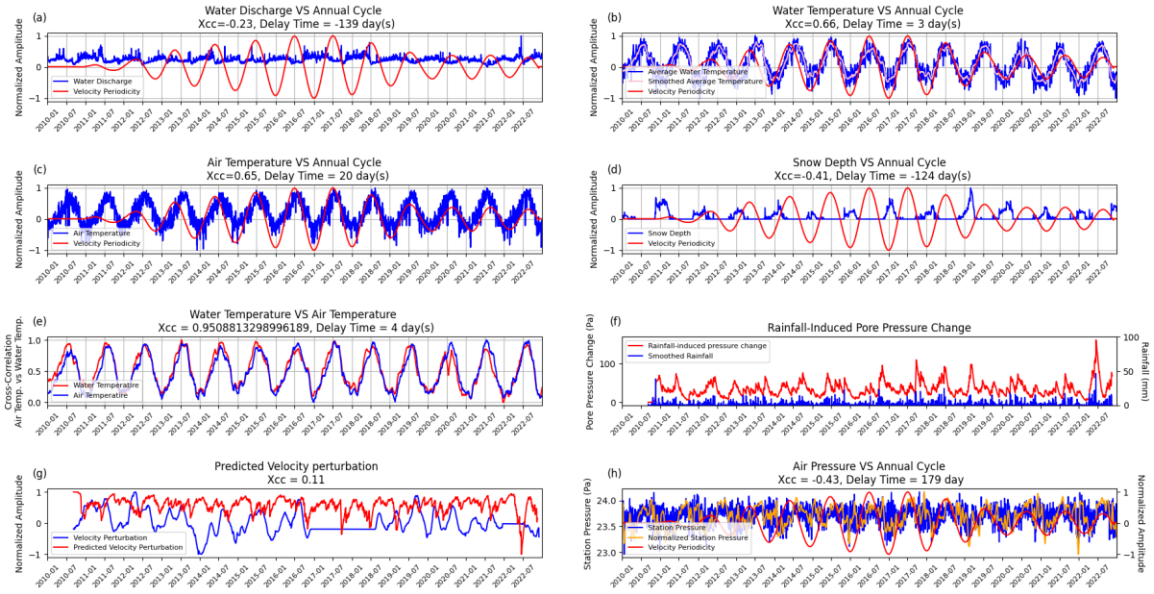

Figure S1. Same as Figure 4. Herein, the red curves depict the annual cycle function, which is derived from the highly filtered dv/v curve within the frequency band of 0.9 Hz to 1.1 Hz. Meanwhile, the blue curves represent the normalized raw climate data, illustrating a direct comparison between the refined analytical function and the initial observational data.

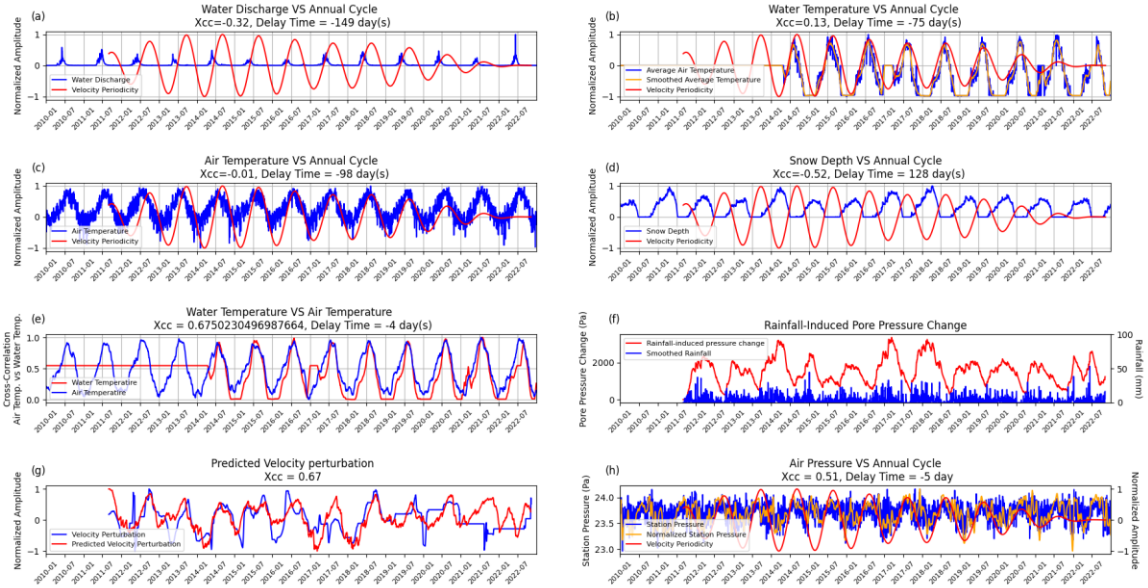

Figure S2. Same as Figure S1 but for Hot Spring Basin.

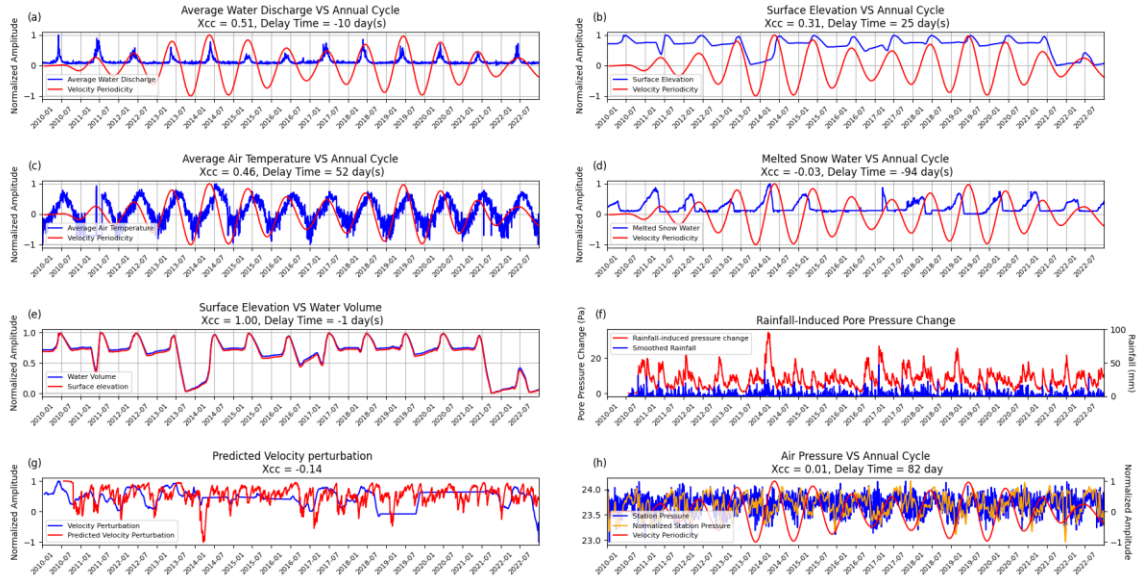

Figure S3. Same as Figure S1 but for Jackson Lake.

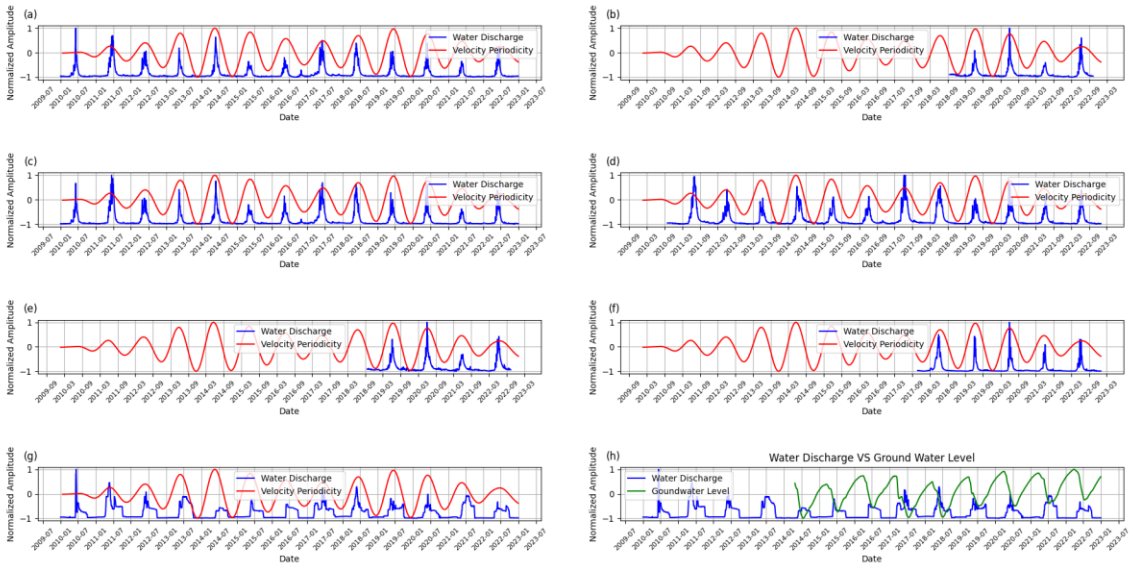

Figure S4. (a) to (g) illustrate the relationship between the velocity periodicity and the water discharge obtained from different water monitoring sites near Jackson Lake. (h) reveals the directly proportional relationship between water discharge and water volume.

REFERENCES

Albuquerque Seismological Laboratory (ASL)/USGS. (1990). United States National Seismic Network [Data]. International Federation of Digital Seismograph Networks. https://doi.org/10.7914/SN/US

Albuquerque Seismological Laboratory (ASL)/USGS. (2003). Intermountain West Seismic Network [Data]. International Federation of Digital Seismograph Networks. https://doi.org/10.7914/SN/IW

Allen, E. T., Day, A. L., & Merwin, H. E. (1935). Hot springs of the Yellowstone National Park. In Carnegie Institution of Washington eBooks. http://ci.nii.ac.jp/ncid/BA01870861

Al-Shukri, H., & Mitchell, B. J. (1988). Reduced seismic velocities in the source zone of New Madrid earthquakes. Bulletin of the Seismological Society of America, 78(4), 1491–1509. https://doi.org/10.1785/bssa0780041491

Anderson, D. L. (1987). A seismic equation of state II. Shear properties and thermodynamics of the lower mantle. Physics of the Earth and Planetary Interiors, 45(4), 307–323. https://doi.org/10.1016/0031-9201(87)90039-2

Aster, R. C., & Shearer, P. M. (1991). High-frequency borehole seismograms recorded in the San Jcinto Fault zone, Southern California Part 2. Attenuation and site effects. Bulletin of the Seismological Society of America, 81(4), 1081–1100. https://doi.org/10.1785/bssa0810041081

Bachrach, R., Nur, A., & Agnon, A. (2001). Liquefaction and dynamic poroelasticity in soft sediments. Journal of Geophysical Research, 106(B7), 13515–13526. https://doi.org/10.1029/2000jb900474

Behrendt, J. C., Tibbetts, B., Bonini, W. E., Lavin, P. M., Love, J., & Reed, J. C. (1968). A geophysical study in Grand Teton National Park and vicinity, Teton County, Wyoming. U.S. Geological Survey Professional Paper. https://doi.org/10.3133/pp516e

Ben-Zion, Y., & Allam, A. A. (2013). Seasonal thermoelastic strain and postseismic effects in Parkfield borehole dilatometers. Earth and Planetary Science Letters, 379, 120–126. https://doi.org/10.1016/j.epsl.2013.08.024

Ben-Zion, Y., & Leary, P. (1986). Thermoelastic strain in a half-space covered by unconsolidated material. Bulletin of the Seismological Society of America, 76(5), 1447–1460. https://doi.org/10.1785/bssa0760051447

Berryman, J. G. (1999). Origin of Gassmann's equations. Geophysics, 64(5), 1627–1629. https://doi.org/10.1190/1.1444667

Boschelli, J., Moschetti, M. P., & Sens-Schönfelder, C. (2021). Temporal seismic Velocity variations: recovery following from the 2019 MW 7.1 Ridgecrest, California earthquake. Journal of Geophysical Research: Solid Earth, 126(4). https://doi.org/10.1029/2020jb021465

Chen, H., Ge, H., & Niu, F. (2014). Semiannual velocity variations around the 2008 Mw 7.9 Wenchuan Earthquake fault zone revealed by ambient noise and ACROSS active source data. Earthquake Science, 27(5), 529–540. https://doi.org/10.1007/s11589-014-0089-5

Ciraula, D. A., Carr, B. J., & Sims, K. W. (2023). Geophysical imaging of the shallow geyser and hydrothermal reservoir structures of Spouter Geyser, Yellowstone National Park: Geyser Dynamics I. Journal of Geophysical Research: Solid Earth, 128(2). https://doi.org/10.1029/2022jb024417

Clarke, D. J., Zaccarelli, L., Shapiro, N. M., & Brenguier, F. (2011). Assessment of resolution and accuracy of the Moving Window Cross Spectral technique for monitoring crustal temporal variations using ambient seismic noise. Geophysical Journal International, 186(2), 867–882. https://doi.org/10.1111/j.1365-246x.2011.05074.x

Clements, T., & Denolle, M. (2018). Tracking groundwater levels using the ambient seismic field. Geophysical Research Letters, 45(13), 6459–6465. https://doi.org/10.1029/2018gl077706

De Fazio, T. L., Aki, K., & Alba, J. (1973). Solid earth tide and observed change in the in situ seismic velocity. Journal of Geophysical Research, 78(8), 1319–1322. https://doi.org/10.1029/jb078i008p01319

Donaldson, C., Winder, T., Caudron, C., & White, R. S. (2019). Crustal seismic velocity responds to a magmatic intrusion and seasonal loading in Iceland's Northern Volcanic Zone. Science Advances, 5(11). https://doi.org/10.1126/sciadv.aax6642

Farrell, J., Husen, S., & Smith, R. B. (2009). Earthquake swarm and b-value characterization of the Yellowstone volcano-tectonic system. Journal of Volcanology and Geothermal Research, 188(1–3), 260–276. https://doi.org/10.1016/j.jvolgeores.2009.08.008

Feng, K., Huang, H., Hsu, Y., & Wu, Y. (2021). Controls on seasonal variations of crustal seismic velocity in Taiwan using Single-Station Cross-Component analysis of ambient noise interferometry. Journal of Geophysical Research: Solid Earth, 126(11). https://doi.org/10.1029/2021jb022650

Finn, C. A., & Morgan, L. A. (2002). High-resolution aeromagnetic mapping of volcanic terrain, Yellowstone National Park. Journal of Volcanology and Geothermal Research, 115(1–2), 207–231. https://doi.org/10.1016/s0377-0273(01)00317-1

Gao, S. S., Silver, P. G., Linde, A. T., & Sacks, I. S. (2000). Annual modulation of triggered seismicity following the 1992 Landers earthquake in California. Nature, 406(6795), 500–504. https://doi.org/10.1038/35020045

Gardner, W. P., Susong, D. D., Solomon, D. K., & Heasler, H. P. (2013). Using environmental tracers and numerical simulation to investigate regional hydrothermal basins-Norris Geyser Basin area, Yellowstone National Park, USA. Journal of Geophysical Research: Solid Earth, 118(6), 2777–2787. https://doi.org/10.1002/jgrb.50210

Hillers, G., Ben-Zion, Y., Campillo, M., & Zigone, D. (2015). Seasonal variations of seismic velocities in the San Jacinto fault area observed with ambient seismic noise. Geophysical Journal International, 202(2), 920–932. https://doi.org/10.1093/gji/ggv151

Hillers, G., Campillo, M., & Fong, K. (2014). Seismic velocity variations at TCDP are controlled by MJO driven precipitation pattern and high fluid discharge properties. Earth and Planetary Science Letters, 391, 121–127. https://doi.org/10.1016/j.epsl.2014.01.040

Houtz, R. E., Ewing, J., & Pichon, X. L. (1968). Velocity of deep-sea sediments from sonobuoy data. Journal of Geophysical Research, 73(8), 2615–2641. https://doi.org/10.1029/jb073i008p02615

Huang, H., Dai, S., Yu, Y., & Xie, F. (2022). Observing Earthquake-Induced Velocity Change on the Rock Slope Following the 2021 M 7.4 Maduo Earthquake 780 km Away. Sustainability, 14(15), 9345. https://doi.org/10.3390/su14159345

Hurley, J. V., & Boos, W. R. (2014). A global climatology of monsoon low-pressure systems. Quarterly Journal of the Royal Meteorological Society, 141(689), 1049–1064. https://doi.org/10.1002/qj.2447

Husen, S., Smith, R. B., & Waite, G. P. (2004). Evidence for gas and magmatic sources beneath the Yellowstone volcanic field from seismic tomographic imaging. Journal of Volcanology and Geothermal Research, 131(3–4), 397–410. https://doi.org/10.1016/s0377-0273(03)00416-5

Jones, T., & Nur, A. (1983). Velocity and attenuation in sandstone at elevated temperatures and pressures. Geophysical Research Letters, 10(2), 140–143. https://doi.org/10.1029/gl010i002p00140

Kern, H. (1978). The effect of high temperature and high confining pressure on compressional wave velocities in quartz-bearing and quartz-free igneous and metamorphic rocks. Tectonophysics, 44(1–4), 185–203. https://doi.org/10.1016/0040-1951(78)90070-7

Luan, Y., Yang, H., Wang, B., Yang, W., Wang, W., Yang, J., & Li, X. (2022). Time-Lapse monitoring of daily velocity changes in Binchuan, southwestern China, using Large-Volume Air-Gun source array data. Seismological Research Letters, 93(2A), 914–930. https://doi.org/10.1785/0220210160

Maguire, R., Schmandt, B., Li, J., Jiang, C., Li, G., Wilgus, J., & Chen, M. (2022). Magma accumulation at depths of prior rhyolite storage beneath Yellowstone Caldera. Science, 378(6623), 1001–1004. https://doi.org/10.1126/science.ade0347

Marston, R. A., Mills, J. D., Wrazien, D. R., Bassett, B., & Splinter, D. K. (2005). Effects of Jackson Lake Dam on the Snake River and its floodplain, Grand Teton National Park, Wyoming, USA. Geomorphology, 71(1–2), 79–98. https://doi.org/10.1016/j.geomorph.2005.03.005

McGreevy, L., & Gordon, E. D. (1964). Ground water east of Jackson Lake, Grand Teton National Park, Wyoming. N/A. https://doi.org/10.3133/cir494

Miao, Y., Shi, Y., Zhuang, H., Wang, S. Y., Liu, H. B., & Yu, X. (2019). Influence of seasonal frozen soil on Near-Surface shear wave velocity in eastern Hokkaido, Japan. Geophysical Research Letters, 46(16), 9497–9508. https://doi.org/10.1029/2019gl082282

Miller, D. S., & Smith, R. B. (1999). P and S velocity structure of the Yellowstone volcanic field from local earthquake and controlled-source tomography. Journal of Geophysical Research, 104(B7), 15105–15121. https://doi.org/10.1029/1998jb900095

Mohamad, E. T. B., Saad, R., Noor, M. M., Isa, M. F. B. M., & Mazlan, A. N. (2010). Excavatability Assessment of weathered sedimentary rock mass using seismic velocity method. Nucleation and Atmospheric Aerosols. https://doi.org/10.1063/1.3537880

Nayak, A., Manga, M., Hurwitz, S., Namiki, A., & Dawson, P. B. (2020). Origin and properties of hydrothermal tremor at Lone Star Geyser, Yellowstone National Park, USA. Journal of Geophysical Research: Solid Earth, 125(12). https://doi.org/10.1029/2020jb019711

Pasquet, S., Holbrook, W. S., Carr, B. J., & Sims, K. W. (2016). Geophysical imaging of shallow degassing in a Yellowstone hydrothermal system. Geophysical Research Letters, 43(23). https://doi.org/10.1002/2016gl071306

Pointer, T., Liu, E., & Hudson, J. (2000). Seismic wave propagation in cracked porous media. Geophysical Journal International, 142(1), 199–231. https://doi.org/10.1046/j.1365-246x.2000.00157.x

Poupinet, G., Ellsworth, W. L., & Fréchet, J. (1984). Monitoring velocity variations in the crust using earthquake doublets: An application to the Calaveras Fault, California. Journal of Geophysical Research: Solid Earth, 89(B7), 5719–5731. https://doi.org/10.1029/jb089ib07p05719

Qiu, H., Hillers, G., & Ben-Zion, Y. (2019). Temporal changes of seismic velocities in the San Jacinto Fault zone associated with the 2016Mw 5.2 Borrego Springs earthquake. Geophysical Journal International, 220(3), 1536–1554. https://doi.org/10.1093/gji/ggz538

Ratdomopurbo, A., & Poupinet, G. (1995). Monitoring a temporal change of seismic velocity in a volcano: Application to the 1992 eruption of Mt. Merapi (Indonesia). Geophysical Research Letters, 22(7), 775–778. https://doi.org/10.1029/95gl00302

Reed, M. H., Muñoz-Sáez, C., Hajimirza, S., Wu, S., Barth, A., Girona, T., Rasht-Behesht, M., White, E., Karplus, M. S., Hurwitz, S., & Manga, M. (2021). The 2018 reawakening and eruption dynamics of Steamboat Geyser, the world's tallest active geyser. Proceedings of the National Academy of Sciences of the United States of America, 118(2). https://doi.org/10.1073/pnas.2020943118

Roumelioti, Z., Hollender, F., & Guéguen, P. (2020). Rainfall-Induced variation of seismic waves velocity in soil and implications for soil response: What the ARGONET (Cephalonia, Greece) vertical array data reveal. Bulletin of the Seismological Society of America, 110(2), 441–451. https://doi.org/10.1785/0120190183

Schnabel, P. B., Seed, H. B., & Leth, J. (1972). Modification of seismograph records for effects of local soil conditions. Bulletin of the Seismological Society of America, 62(6), 1649–1664. https://doi.org/10.1785/bssa0620061649

Schutt, D., Dueker, K. G., & Yuan, H. (2008). Crust and upper mantle velocity structure of the Yellowstone hot spot and surroundings. Journal of Geophysical Research, 113(B3). https://doi.org/10.1029/2007jb005109

Sens-Schönfelder, C., & Wegler, U. (2006). Passive image interferometry and seasonal variations of seismic velocities at Merapi Volcano, Indonesia. Geophysical Research Letters, 33(21). https://doi.org/10.1029/2006gl027797

Smith, R. B., Schilly, M. M., Braile, L. W., Ansorge, J., Lehman, J. L., Baker, M. R., Prodehl, C., Healy, J. H., Mueller, S., & Greensfelder, R. W. (1982). The 1978 Yellowstone-Eastern Snake River Plain Seismic Profiling Experiment: Crustal structure of the Yellowstone Region and experiment design. Journal of Geophysical Research, 87(B4), 2583–2596. https://doi.org/10.1029/jb087ib04p02583

Son, M. S., & Kang, Y. J. (2012). Propagation of shear waves in a poroelastic layer constrained between two elastic layers. Applied Mathematical Modelling, 36(8), 3685–3695. https://doi.org/10.1016/j.apm.2011.11.008

Taira, T., Brenguier, F., & Kong, Q. (2015). Ambient noise-based monitoring of seismic velocity changes associated with the 2014 Mw 6.0 South Napa earthquake. Geophysical Research Letters, 42(17), 6997–7004. https://doi.org/10.1002/2015gl065308

Talwani, P., Chen, L., & Gahalaut, K. (2007). Seismogenic permeability, ks. Journal of Geophysical Research, 112(B7). https://doi.org/10.1029/2006jb004665

Tsai, V. C. (2011). A model for seasonal changes in GPS positions and seismic wave speeds due to thermoelastic and hydrologic variations. Journal of Geophysical Research, 116(B4). https://doi.org/10.1029/2010jb008156

University of Utah. (1983). Yellowstone National Park Seismograph Network [Data]. International Federation of Digital Seismograph Networks. https://doi.org/10.7914/SN/WY

Waite, G. P., Smith, R. B., & Allen, R. M. (2006). VP and VS structure of the Yellowstone hot spot from teleseismic tomography: Evidence for an upper mantle plume. Journal of Geophysical Research, 111(B4). https://doi.org/10.1029/2005jb003867

Wallén, J., Gunnarsson, S., & Norrlöf, M. (2013). Analysis of boundary effects in iterative learning control. International Journal of Control, 86(3), 410–415. https://doi.org/10.1080/00207179.2012.733889

Wang, Q., Brenguier, F., Campillo, M., Lecointre, A., Takeda, T., & Aoki, Y. (2017). Seasonal crustal seismic velocity changes throughout Japan. Journal of Geophysical Research: Solid Earth, 122(10), 7987–8002. https://doi.org/10.1002/2017jb014307

Weaver, R. L., Hadziioannou, C., Larose, E., & Campillo, M. (2011). On the precision of noise correlation interferometry. Geophysical Journal International, 185(3), 1384–1392. https://doi.org/10.1111/j.1365-246x.2011.05015.x

Werner, C. A., Hurwitz, S., Evans, W. C., Lowenstern, J. B., Bergfeld, D., Heasler, H. P., Jaworowski, C., & Hunt, A. G. (2008). Volatile emissions and gas geochemistry of Hot Spring Basin, Yellowstone National Park, USA. Journal of Volcanology and Geothermal Research, 178(4), 751–762. https://doi.org/10.1016/j.jvolgeores.2008.09.016

Wessel, P., Luis, J. F., Uieda, L., Scharroo, R., Wobbe, F., Smith, W. H. F., & Tian, D. (2019). The Generic Mapping Tools version 6 [Software]. Geochemistry, Geophysics, Geosystems, 20(11), 5556–5564. https://doi.org/10.1029/2019GC008515

White, D. E., Hutchinson, R. A., & Keith, T. E. (1988). The geology and remarkable thermal activity of Norris Geyser Basin, Yellowstone National Park, Wyoming. U.S. Geological Survey Professional Paper. https://doi.org/10.3133/pp1456

Winkler, K. W. (1983). Frequency dependent ultrasonic properties of high-porosity sandstones. Journal of Geophysical Research, 88(B11), 9493–9499. https://doi.org/10.1029/jb088ib11p09493

Wyllie, M. R. J., Gregory, A., & Gardner, G. H. F. (1958). AN EXPERIMENTAL INVESTIGATION OF FACTORS AFFECTING ELASTIC WAVE VELOCITIES IN POROUS MEDIA. Geophysics, 23(3), 459–493. https://doi.org/10.1190/1.1438493

Yuan, H., & Dueker, K. G. (2005). Teleseismic P-wave tomogram of the Yellowstone plume. Geophysical Research Letters, 32(7). https://doi.org/10.1029/2004gl022056

Zeinali, S. M., & Abdelaziz, S. L. (2020). Effect of heating rate on thermally induced pore water pressures and volume change of saturated soils. Geo-Congress 2020. https://doi.org/10.1061/9780784482827.004

Zhan, T. L. T., Ng, C. W. W., & Fredlund, D. G. (2007). Field study of rainfall infiltration into a grassed unsaturated expansive soil slope. Canadian Geotechnical Journal, 44(4), 392–408. https://doi.org/10.1139/t07-001

Zhang, X. J., & Wang, Z. (2017). Interrill soil erosion processes on steep slopes. Journal of Hydrology, 548, 652–664. https://doi.org/10.1016/j.jhydrol.2017.03.046

Zhao, Q. (2005). Experiments of physical modeling for petrophysical properties of natural gas hydrate. Chinese Journal of Geophysics. https://en.cnki.com.cn/Article_en/CJFDTOTAL-DQWX200503023.htm

SECTION

2. CONCLUSIONS AND RECOMMENDATIONS

In this dissertation, we have embarked on an in-depth comparative study of seismic activities and their underlying geodynamic processes within two geologically distinct but equally fascinating regions: the Tibetan Plateau and Yellowstone National Park. Through a detailed examination of seismic anisotropy layering beneath the southern Tibetan Plateau, constrained by shear wave splitting and receiver function analyses (Paper I), and an innovative analysis revealing the annual periodicity of seismic velocities in Yellowstone Caldera and its surrounding areas (Paper II), this research offers new insights into the complexities of Earth's subsurface dynamics.

The study's first component elucidates the intricate geodynamic structure of the Tibetan Plateau, unveiling the presence of multilayer anisotropy which signifies varying depths of seismic origins across the Plateau. By leveraging advanced seismic analysis techniques, the research provides a detailed 3-D model highlighting the coexistence of strong and weak anisotropy within the Plateau. This model not only sheds light on the Plateau's tectonic evolution but also emphasizes the influence of continental deformation and plate tectonics on seismic behaviors.

Conversely, the investigation into the Yellowstone Caldera leverages surface wave analyses to decode the crustal velocity structure, revealing low-velocity anomaly zones and pronounced annual periodicity in seismic velocity profiles. This analysis underscores the significant impact of external environmental factors, such as temperature

and atmospheric pressure, on seismic velocities. Moreover, it accentuates the caldera's dynamic response to meteorological variations, providing a nuanced understanding of its geological stability.

Together, these studies portray a comprehensive picture of the seismic phenomena occurring beneath the Tibetan Plateau and Yellowstone National Park. The juxtaposition of these regions' seismic characteristics enables a broader comprehension of the geological and tectonic processes at play. This research not only bridges gaps in the existing literature but also pioneers a holistic perspective on seismic monitoring, hazard assessment, and geological exploration.

Considering these findings, it is recommended that future research continue to explore the intersection of geodynamic phenomena and seismic activities, with an emphasis on integrating advanced geophysical methods. Such endeavors will undoubtedly further our understanding of Earth's interior mechanisms, contributing to improved seismic hazard assessment and mitigation strategies.

BIBLIOGRAPHY

De Fazio, T. L., Aki, K., & Alba, J. (1973). Solid earth tide and observed change in the in situ seismic velocity. Journal of Geophysical Research, 78(8), 1319–1322. https://doi.org/10.1029/jb078i008p01319

Gao, S., & Liu, K. (2009). Significant seismic anisotropy beneath the southern Lhasa Terrane, Tibetan Plateau. Geochemistry, Geophysics, Geosystems, 10(2). https://doi.org/10.1029/2008gc002227

Husen, S., Smith, R. B., & Waite, G. P. (2004). Evidence for gas and magmatic sources beneath the Yellowstone volcanic field from seismic tomographic imaging. Journal of Volcanology and Geothermal Research, 131(3–4), 397–410. https://doi.org/10.1016/s0377-0273(03)00416-5

Jolivet, L., Faccenna, C., Becker, T., Tesauro, M., Sternai, P., & Bouilhol, P. (2018). Mantle Flow and Deforming Continents: From India‐Asia Convergence to Pacific Subduction. Tectonics, 37(9), 2887‐2914. https://doi.org/10.1029/2018tc005036

McKenzie, D. (1978). Active tectonics of the Alpine--Himalayan belt: the Aegean Sea and surrounding regions. Geophysical Journal International, 55(1), 217–254. https://doi.org/10.1111/j.1365-246x.1978.tb04759.x

Miller, D. S., & Smith, R. B. (1999). P and S velocity structure of the Yellowstone volcanic field from local earthquake and controlled-source tomography. Journal of Geophysical Research, 104(B7), 15105–15121. https://doi.org/10.1029/1998jb900095

Molnar, P., England, P., & Martinod, J. (1993). Mantle dynamics, uplift of the Tibetan Plateau, and the Indian Monsoon. Reviews of Geophysics, 31(4), 357. https://doi.org/10.1029/93rg02030

Pasquet, S., Holbrook, W. S., Carr, B. J., & Sims, K. W. (2016). Geophysical imaging of shallow degassing in a Yellowstone hydrothermal system. Geophysical Research Letters, 43(23). https://doi.org/10.1002/2016gl071306

Roumelioti, Z., Hollender, F., & Guéguen, P. (2020). Rainfall-induced variation of seismic waves velocity in soil and implications for soil response: What the ARGONET (Cephalonia, Greece) vertical array data reveal. Bulletin of the Seismological Society of America, 110(2), 441–451. https://doi.org/10.1785/01201

Silver, P. G. (1996). SEISMIC ANISOTROPY BENEATH THE CONTINENTS: Probing the Depths of Geology. Annual Review of Earth and Planetary Sciences, 24(1), 385–432. https://doi.org/10.1146/annurev.earth.24.1.385

Waite, G. P., Smith, R. B., & Allen, R. M. (2006). VP and VS structure of the Yellowstone hot spot from teleseismic tomography: Evidence for an upper mantle plume. Journal of Geophysical Research, 111(B4). https://doi.org/10.1029/2005jb00386790183

Wu, J., Zhang, Z., Kong, F., Yang, B. B., Yu, Y., Liu, K. H., & Gao, S. S. (2015). Complex seismic anisotropy beneath western Tibet and its geodynamic implications. Earth and Planetary Science Letters, 413, 167–175. https://doi.org/10.1016/j.epsl.2015.01.002

VITA

Cong Shen received his bachelor's degree in Gology & Geophysics from Missouri University of Science and Technology in December 2017 and in Explortation Technology and Engineering from China University of Petroleum (East China) in May 2018. He joined Dr. Liu and Dr. Gao's research group in Geology & Geophysics program to pursue his Ph.D. degree at Missouri University of Science and Technology in August 2018.

During the year from 2019 to 2024, he worked as a teaching assistant or research assistant in the Geology & Geophysics program at Missouri University of Science and Technology. He was a secretary and treasure of Society of Exploration Geophysics (SEG) S&T student chapter. He was vice president of Chinese students and scholars' association in 2019. He presented his research works at American Geophysical Union (AGU) annual meeting in 2021 and 2022. He was awarded as second place prize of excellent student poster presentation in the Fifth Biennial Field Conference of the American Association of Petroleum Geologists (AAPG), Mid-Continent Section in 2022. His research focused on the crust and mantle anisotropy in the Indian-Eurasian collision zones using shear waves splitting and receiver function methods and ambient noise-based tomography in Yellowstone.

In May 2024, he received his Ph.D. degree in Geology and Geophysics from Missouri University of Science and Technology.